This is to certify that the

dissertation entitled

The Structural Changes and
Their Effects upon the
Magnetic Properties of
Ultrathin Fe Layers

presented by

Heekyung Sung

has been accepted towards fulfillment
of the requirements for

_____Ph.D._____ degree in _Physics_

Carl L. Foiles

Major professor

Date _December 21, 1990_

0-12771

PLACE IN RETURN BOX to remove this checkout from your record.
TO AVOID FINES return on or before date due.

DATE DUE	DATE DUE	DATE DUE
————	————	————
————	————	————
————	————	————
————	————	————
————	————	————
————	————	————
————	————	————

MSU Is An Affirmative Action/Equal Opportunity Institution

c:\circ\datedue.pm3-p.1

STRUCTURAL CHANGES AND THEIR

EFFECTS UPON

THE MAGNETIC PROPERTIES OF

ULTRATHIN Fe LAYERS

By

Heekyung Sung

A DISSERTATION

Submitted to

Michigan State University

in partial fulfillment of the requirements

for the degree of

DOCTOR OF PHILOSOPHY

Department of Physics and Astronomy

1990

ABSTRACT
STRUCTURAL CHANGES AND THEIR EFFECTS UPON
THE MAGNETIC PROPERTIES OF ULTRATHIN Fe LAYERS

By

Heekyung Sung

Ultrathin Fe/Si, Fe/Mo, Fe/V and Fe/Cr metallic multilayers have been prepared with a UHV sputtering system. The individual layer thickness is between 3 monolayers(ML) and 40 ML. Sputtered Si is amorphous while the lattice parameter mismatches between bulk crystalline constituents are 9%, 5% and 0.6% in Fe/Mo, Fe/V and Fe/Cr respectively.

Standard reflection X-ray diffraction(XRD), transmission electron diffraction(TED) and limited EXAFS data were used for structural studies. Fe layers in Fe/Si are structurally isolated(non-coherent). For layer thickness of $\leq 10\mathring{A}$, amorphous Fe layers were observed in Fe/Si and these amorphous Fe layers were non-magnetic. Fe/Mo, Fe/V and Fe/Cr systems form coherent structures with a perpendicular coherence length of at about $\sim 200\mathring{A}$. Strained layer superlattices(SLS) have been directly observed in Fe/V and Fe/Mo for the first time using TED. The double BCC to single BCC transition in the layer planes occurred at bilayer thickness $\sim$ 32ML in Fe/V and $\sim$16ML in Fe/Mo. XRD data were consistent with TED data but suggested that the strain was uniaxial.

The saturation magnetizations of Fe multilayers at thin layer thicknesses were closely related to the lattice mismatches. Fe/Mo lost its magnetism abruptly at a layer thickness between 3ML and 6ML while the reduction in Fe/V was gradual. Fe/Cr retained bulk-like magnetism over all the thickness range indicating little structural change in the Fe layers.

Anomalously large saturation fields and magnetic anisotropy have been observed in Fe/Cr. The antiferromagnetic coupling between magnetic Fe layers, known to exist in Fe/Cr, is believed to be responsible for these large saturation fields and anisotropy.

To my mother and father

Acknowledgements

I wish to thank Professor Carl Foiles for his support and patient guidance through my thesis work. Without his help it would not have been possible to finish this thesis.

I would like to thank Professors J. Cowen, T. Kaplan, J. Linnemann and W. Lynch and for their service as my Ph. D guidance committee and Professor J. S. Kovacs for his warm encouragement during my initial stage at Michigan State University.

I am also indebted to W. Abdul-Razzaq, C. Fierz and R. Loloee for helping me in operation of the sputtering system.

Most of all I would like to thank my wife, Hyeran, for her loving and patient support during the course of my thesis work.

Contents

List of Tables

List of Figures

ix

Chapter 1

Introduction

1.1 Motivation

The fabrication of ultrathin metallic films and multilayers is an expanding research area that has produced exciting results associated with elastic anomalies[1], magnetic properties[2][3], superconductivity[4] , transport properties[1] and X-ray reflectivities of sufficient strength to produce mirrors[5].

The main research field of this thesis lies within the area of magnetic properties of ultra thin metallic layers. The magnetic properties of ultrathin magnetic layers are interesting from both the fundamental and applied point of view. Fundamental properties which can be studied with ultrathin magnetic layers include two dimensional magnetism, surface and interface magnetism and new magnetic structure from artificially layered structures involving antiferromagnetic coupling between ultrathin magnetic layers. Magnetic mass data storage offers a possible application of this field.

For the purpose of this thesis ultrathin denotes layers with thicknesses between 3 and 40 atomic monolayers(ML). Investigation of ultrathin magnetic layers can be devided into three basic approaches. In one approach the layer of interest maintains a free surface and is grown upon a substrate chosen to control the structure of the layer. Surface science techniques and theoretical consideration of broken symmetry are essential in this approach. The second approach is similar to the first

1

and continues on to study effects as a controlled overlayer is added to the previously free surface. The third approach involves numerous ultrathin magnetic layers and incorporates them into some type of periodic multilayered structure. Controlled symmetries can be produced and the possibility of interactions between magnetic layers must be considered.

This thesis uses the third approach, multilayers. The advantages of this approach are as follows: (i) Structural change in the magnetic layers can be induced by combining the magnetic layers with various materials having different structures. (ii) Due to the multilayered structure, a large number of magnetic layers are involved giving strong magnetic signal for easier measurements. (iii) The multilayered structure also offers an opportunity to observe the possible magnetic interlayer interaction between magnetic layers. The difficulty in obtaining sufficiently detailed structural information for a multilayered structure and its buried interfaces is one of the disadvantages of this approach. Solving this difficulty is a main subject in this thesis.

1.2   Basic structure

A metallic multilayer is made by depositing two elements alternatively on a proper substrate. The building block of a multilayer is a bilayer which consists of N_A atomic monolayers(ML) of element A and N_B atomic monolayers of element B as shown in fig.1.1. Our typical multilayers repeat the bilayer for M cycles to give a total thickness of approximately $1800\mathring{A}$. The periodicity (or the compositional modulation wavelength) Λ is given by

$$\Lambda = (N_A - 1)d_A + (N_B - 1)d_B + 2\bar{d} \tag{1.1}$$

where d_A and d_B are the lattice spacing of element A and B, and $\bar{d}$ is their average value which we take as the spacing between two unlike atoms at interface. We will denote a multilayer by $(N_A$ ML A$/$ N_B ML B$)$M. This one has N_A monolayers of A and N_B monolayers of B in a bilayer and it is repeated M times. The resulting structure is referred to as an artificial superlattice. The distinction between superlattice
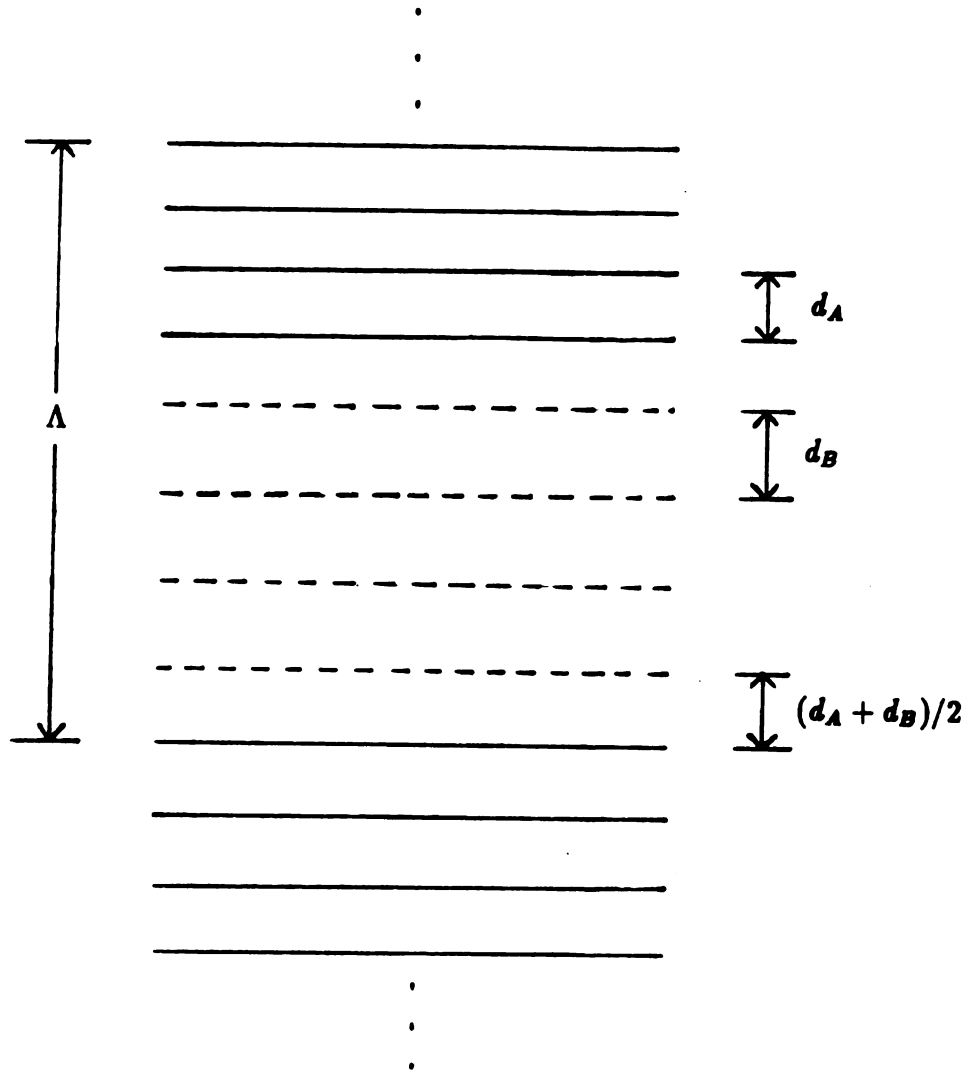
Figure 1.1: Basic structure of an ideal multilayer. The unit cell consists of N_A atomic layers of element A and N_B atomic layers of element B with the lattice spacings d_A and d_B respectively.

and multilayer varies with different authors but, generally, a multilayered structure with a high order of structural coherence is called a superlattice.

An artificial superlattice is an inherently metastable structure and relies for its existence on slow intraplane kinetics(during the growth process) and slow interplane. diffusion(during and after the growth process). The metastable nature of artificial superlattices suggests that they may be engineered to have material properties which might not be otherwise attainable. This is a major motivation for the large current interest in these materials.

An understanding of the physical properties (magnetic properties in this thesis) requires careful measurements of both the crystalline structures involved and the extent of their commensurateness. We define two coherence lengths in describing the structural order. PSCL is the perpendicular structural coherence length and is associated with the multilayer structure perpendicular to the substrate surface while TSCL is the transverse structural coherence length and is associated with the structure in planes parallel to the substrate surface. In fig.1.2 some possible structural disorders related to PSCL or TSCL are illustrated. Disordered interfaces due to lattice mismatch, intermixing and irregular periodicity reduce the PSCL and the formation of many randomly oriented grains reduces the TSCL.

1.3 Experimental environments

Fe is the magnetic layer of interest in this thesis and we have made Fe/Si ,Fe/Mo,Fe/V and Fe/Cr multilayers in an effort to systematically change the environments of the Fe layers. Sputtered Si is amorphous. The transition metals used for our metallic multilayers have BCC crystal structure as their natural bulk structure. Bulk Mo,V and Cr have the lattice parameter mismatches with bulk Fe of about 9%, 5% and 0.6% respectively. Recently the Fe/Cr system has attracted special interest. Antiferromagnetic interlayer coupling between the ultrathin magnetic Fe layers across the Cr interlayer has been observed by various groups.[6] [7] [8] The rare earth magnetic superlattice Gd/Y is another example of magnetic interlayer coupling; coupling be-
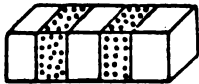
Figure 1.2: Structural orders inherent in multilayers. Reflection XRD is sensitive to the PSCL. After Fujii[2]

tween the Gd layers can be made ferromagnetic or antiferromagnetic by varying the Y layer thickness .[9] Since the combinations of bulk Fe and Cr, and bulk Gd and Y have BCC and HCP structure respectively with nearly identical lattice parameters, these systems have produced a belief that large coherence lengths are crucial in controlling magnetic coupling.

In this thesis magnetic properties(saturation magnetization and magnetic anisotropy) of ultrathin Fe layers in various multilayer systems will be tested. Chapter 2 describes the sample preparation conditions and procedures with the MSU sputtering system. Chapter 3 discusses the structural characterization of the metallic multilayers using standard reflection X-ray diffraction(XRD) and transmission electron diffraction(TED). In chapter 4 the magnetic properties of Fe multilayers are presented and in chapter 5 some limited EXAFS(extended X-ray absorption fine structure) data for Fe multilayers is discussed. EXAFS data provide measurements of local order that can be important in understanding magnetic behavior.

Bibliography

[1] R. C. Cammarata, Scripta Metallur. 20, 479 (1986)

[2] T. Shinjo and T. Takada, Metallic superlattices (Elsevier Science Publishers B.V., 1987)

[3] B. Y. Jin and J. B. Ketterson, Advances in Physics 38, 189 (1989)

[4] S. T. Ruggiero, Superlattices and Microstructures 1, 441 (1985)

[5] Troy W. Barbee, Jr. , in Synthetic Modulated Structures, edited by L.L. Chang and B.C. Giessen (Academic Press, 1985)

[6] S.S.P. Parkin, N. More and K.P. Roche, Phys. Rev. Lett., 64, 2304 (1990)

[7] M.N. Baibich, J.M. Broto, A. Fert, F. Nguyen Van Dau, F. Petroff, P. Eitenne, A. Friederich, and J. Chazelas, Phys. Rev. Lett., 61, 2472 (1988)

[8] C. Carbone and S. F. Salvarado, Phys. Rev. B. 36, 2433 (1987)

[9] C.F. Majkrzak, J.W. Cable, J. Kwo, M. Hong, D.B. McWhan, Y. Yafet, J.V. Waszczak, and C. Vettier, Phys. Rev. Lett., 56, 2700 (1986)

Chapter 2

Sample preparation

2.1 Introduction

There are numerous epitaxial methods available nowadays for preparation of artificial metallic superlattices; MBE (Molecular Beam Epitaxy), vacuum evaporation and sputtering have been most widely used. A system to prepare a superlattice might be broken down into the following components or functions.[1]

(1) Sources to produce atomic fluxes of the desired constituents of the superlattices.

(2) Means to position the substrates alternatively over the sources.

(3) Methods to mount the substrates and maintain the substrate temperature.

(4) A deposition chamber to establish the desired ambient background conditions such as high vacuum or inert gas.

(5) Methods to control and monitor the fluxes.

With regard to the method of producing atomic fluxes we distinguish three modes

(i)physical vapor deposition (PVD)

(ii)chemical vapor deposition (CVD)

(iii)electrodeposition

MBE, vacuum deposition and sputtering methods are categorized as PVD. PVD has been carried out with thermal evaporation, electron beam heating and dc or rf

sputtering being the most commonly used techniques. A resistively heated crucible containing a tight fitting cover with a small hole to allow the vapor to escape is called an effusion cell.[2] The process of growing epitaxial films using an effusion cell is referred to as MBE. Electron gun evaporation is accomplished by impacting a beam of high energy(greater than 3 Kev) electrons on the material to be evaporated. Sputtering is a very powerful method for depositing metallic superlattices. In the sputtering process a plasma discharge is created by ionization of an inert gas(e.g. Ar) and maintained above the target (source) when an appropriate negative potential is applied to the target. Target material is sputtered by the impact of energetic ions. For a given power applied to the sputtering gun, the atomic flux is generally quite stable with time until a substantial part of the target material has eroded. The amount of fluxes and the kinetic energy of the sputtered atoms can be controlled by adjusting the applied potential, the plasma current, the pressure of the sputtering gas and the target-to-substrate distance.

All samples in this thesis were made with the MSU sputtering system and fig .2.1 shows a schematic diagram of the MSU sputtering system. Although detailed descriptions of this system have been presented by J.M. Slaughter and G. Kenning [3][4][5] a brief review of them will be attempted in the next sections.

2.2   Substrates and samples

Substrates were mounted on the Substrate Positioning and Monitoring Apparatus (SPAMA). Each substrate had a covering shutter. The SPAMA can accommodate 16 substrates so that 16 different samples could be made without breaking vacuum. To make multilayered films the SPAMA was positioned alternatively over two sputtering sources by a stepping motor which is controlled by an IBM-PC. Typically, two sets of samples having the same nominal number of atomic planes per layer but different sample total thicknesses were prepared. One set was prepared on polished c-axis oriented sapphire (Al_2O_3) crystal substrates and had the bilayer thickness repeated until a total sample thickness was about $1800\text{\AA}$. This set was used for reflection X-
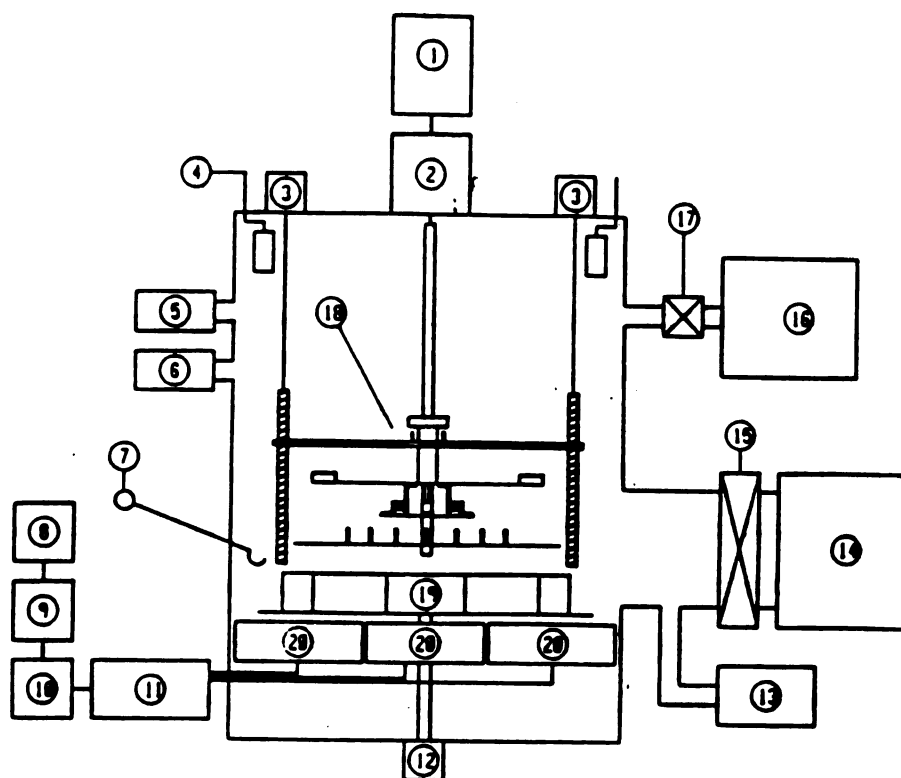
1. Stepping motor
2. Rotary feedthrough
3. Rotary feedthrough
4. Meissner trap
5. Ionization gauge
6. Convectron gauge
7. Wobble stick
8. UHP Ar tank
9. Cold-trap gas purifier
10. Hydrox gas purifier
11. Gas flow controller
12. Rotary feedthrough
13. Residual gas analyzer
14. Cryopump
15. Gate valve
16. Mechanical pump
17. Bellows sealed valve
18. SPAMA
19. Shutter assembly
20. Sputtering source

Figure 2.1: Schematic block diagram of the MSU sputtering system. After J.M. Slaughter, Ph. D. thesis, Michigan State University, 1987

ray studies, EXAFS data collections and magnetic measurements. The second set of samples was deposited on freshly cleaved NaCl substrates. These samples had at least 5 bilayer distances and gave the total thickness of between $400\overset{\circ}{A}$ to $500\overset{\circ}{A}$. After reflection X-ray measurements the thinner samples were floated off the NaCl onto Cu grids to provide free standing films for TED studies.

2.3   Sputtering sources and gun parameters

Sputtering is the emission of the surface atoms of a target material by bombarding it with energetic ions. We use Ar^+ ions to bombard the targets. Sputtering is done in a cylindrical stainless steel chamber of height 48 cm and radius 23 cm. The sputtering chamber was pumped to ≤ 0.5 torr with a mechanical pump and then further pumped down to $< 1 \times 10^{-8}$ torr with a CTI cryopump and a Meissner trap. Then ultra-high purity Ar gas was introduced into the chamber giving a pressure of 2.5×10^{-3} torr.

Four Simard "Tri-Mag" sputtering guns are mounted 90° from each other on a circle of radius 14 cm. Targets with 99.9 % purity are mounted on each gun and the target to substrate distance is 10 cm. About 50 ev energy electrons are passed through the Ar flowing over the target to produce a plasma discharge. A negative potential is applied to the target and the positive Ar^+ ions are accelerated to the target and bombard it .

Fig.2.2 is a schematic cross-sectional diagram to demonstrate the control of the atomic fluxes. Atomic beams from the sputtering sources reach the substrate after passing through a hole in the chimney top and then through a shutter mounted on the SPAMA. If the deposition rate is measured as a function of angular displacement from the center of the target it is found to drop to zero between 20 and 35 degrees depending on the size of the hole.[3] Considering that the sources are separated by 90° and that the time between sources is approximately 0.2 sec it is clear that the intermixing of two atomic fluxes is negligible. With the completion of a given sample, its shutter is closed.

stepping motor ⟶

SPAMA ⟶

chimney ⟶

Sputtering sources | A | B
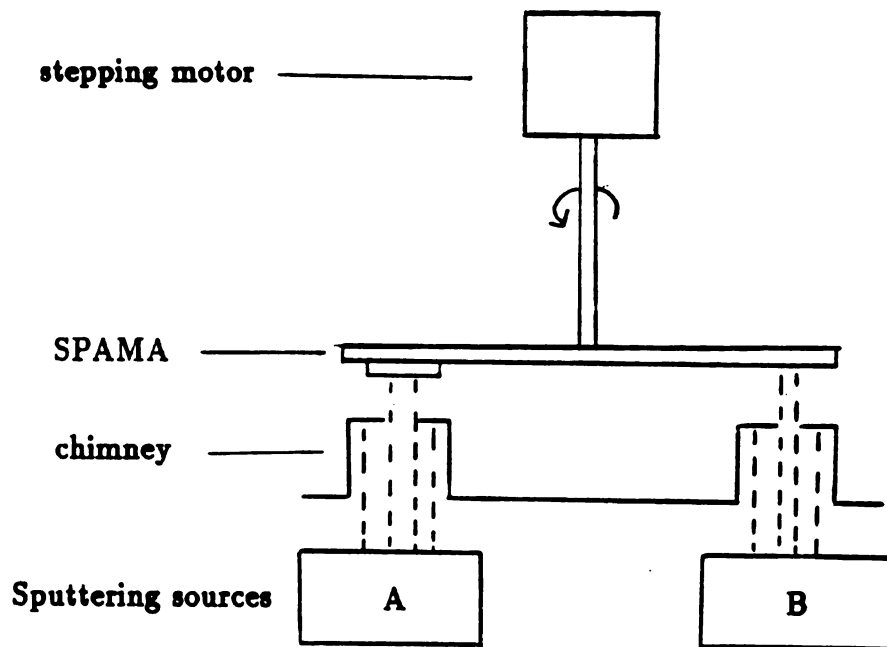
Figure 2.2: Atomic flux control in the MSU sputtering system. Far separation between sputtering sources and collimation of each atomic flux ensure no intermixing between the two fluxes at the substrate.

The deposition rate can be changed by adjusting the Ar pressure, target-to-substrate distance, the target potential and the plasma current. The gun parameters used in this work were determined by trial and error with the constraint that the substrate temperature should not be too hot. Too large Ar energies or total flux of sputtered atoms cause thermal interdiffusion and poor layering in samples.[5]

Temescal FTM-3000 quartz crystal film thickness monitors (FTM) are used to determine the deposition rates prior to and directly after making samples. Desired layer thicknesses in the samples are programmed into the computer which controls the stepping motor attached to the SPAMA plate.

The gun parameters and the deposition rates of each constituent for the multilayers in this thesis are summarized in table 2.1. For the all cases the Ar pressure was kept at 2.5×10^{-3}torr and the target to substrate distance was 10 cm.

Substance	Target potential	Plasma current	Deposition rate
Fe	525 V	1.0 A	7.0 $\mathring{A}$/sec
Cr	500 V	0.8 A	6.9 $\mathring{A}$/sec
V	725 V	1.1 A	7.3 $\mathring{A}$/sec
Mo	320 V	1.1 A	7.9 $\mathring{A}$/sec
Si	300 V	0.8 A	2.0 $\mathring{A}$/sec

Table 2.1: Gun parameters for each constituent of the Fe multilayers.

Bibliography

[1] B.Y. Jin and J.B. Ketterson, Advances in Physics, 38, 189 (1989)

[2] F. Reif, Fundamentals of Statistical and Thermal Physics (McGraw-Hill Book Company,1965)

[3] J.M. Slaughter, Ph. D. thesis , Michigan State University, 1987

[4] J.M. Slaughter, W.P. Pratt,Jr. and P.A. Schroeder, Rev. Sci. Instrum. 60, 127 (1989)

[5] G. Kenning, Ph. D. thesis, Michigan State University, 1988

Chapter 3

Structural studies with XRD and TED

When we fabricate multilayers, in most cases a structural characterization is necessary to confirm the successful growth of the desired samples. X-ray diffraction(XRD) provides the most easily interpreted structural data characterizing a broad range of multilayers. This technique is a nondestructive and readily available method, and most of the measurements can be done in a standard reflection geometry while leaving the sample on the substrate. The evolution of one-dimensional order along the growth direction can be studied on a standard diffractometer.

X-rays scattered by individual atoms give rise to interference depending upon the positions of the scatterers. The structural information from XRD includes

(i) the positions of the average Bragg lines and the surrounding satellite lines are used to calculate the average lattice spacings and the average modulation wavelength.

(ii) the FWHM of the average Bragg line gives a perpendicular structural coherence length (PSCL). For PSCL the Scherrer formula

$$\xi_\perp = \frac{0.9\lambda}{FWHM \cos \theta_{Avg}} \quad (3.1)$$

is used where λ is the wavelength of X-ray and θ_{Avg} is the position of the average Bragg line.

(iii) The relative intensities of the satellites can give additional information about a

16

unit bilayer if the uniqueness of the bilayer model can be established.

In this chapter we describe the experimental setup for the X-ray diffraction measurements, present the results of calculations based on various models of chemical and structural environments to demonstrate how diffraction patterns reflect the structural characteristics of multilayers, and then analyze the data of actual samples. Complementary data from TED studies are also discussed.

3.1 Experimental method

A Rigaku θ-2θ diffractometer with Cu-$K\alpha$ radiation is used for all XRD measurements. The wavelength(λ) of Cu-$K\alpha$ line is 1.5406Å.

Since multilayers are compositionally modulated in the growth direction(i.e . perpendicular to the surface of the substrate), knowledge of the structure along this direction is of primary interest. This knowledge can be achieved using a standard reflection geometry which is shown in fig. 3.1. X-rays specularly reflected by multilayer film plane give rise to interference depending on the position of the atoms. The scattering vector is perpendicular to the sample plane in this geometry and is defined as

$$\vec{q} = \vec{k_f} - \vec{k_i} \tag{3.2}$$
$$q = |\vec{q}| = 2k \sin \theta$$

$\vec{k_i}$ and $\vec{k_f}$ are the wave vectors of the incident and reflected X-rays respectively and the magnitude is unchanged for elastic scattering with value $k = 2\pi/\lambda$. If the lattice constant of the c-axis is chosen to be the modulation period Λ, we have the reciprocal lattice constant $G = 2\pi/\Lambda$ along this axis. A constructive interference occurs whenever the scattering vector is an integral multiple of the reciprocal vector.

$$q = Gn = 2\pi n/\Lambda, n = integer \tag{3.3}$$

Combining eq.3.2 and eq.3.3 leads to the well known Bragg's law in kinematical
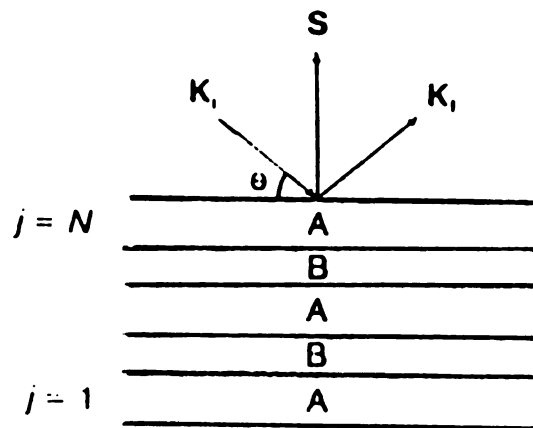
Figure 3.1: **The geometry of the standard reflection X-ray diffraction . The scattering vector is perpendicular to the sample plane.**

diffraction

$$2\Lambda \sin \theta = n\lambda \qquad (3.4)$$

When our multilayer is grown successfully, the first order Bragg reflection (001) due to the compositional modulation period appears at the scattering vector $q = 2\pi/\Lambda$, or at the scattering angle given by $2\theta = 2 \sin^{-1}(\lambda/2\Lambda)$. Higher order reflections (00n) appear at positions expressed by integral multiples of G, q=nG.

3.2 X-ray model calculations

3.2.1 Ideal superlattices

For direct structural information it is necessary to know both the amplitude and the phase of the scattered waves; unfortunately, only the intensity(the square of the amplitude) is observed experimentally. Therefore one often has to make some model calculations which yield only part of the information on the multilayer structures. The model calculation is quite straightforward for a number of idealized geometries. The ideal diffraction models which are most frequently used can be categorized as follows.

(i) the step model : atomically sharp interface, bulk structural properties for individual layers and no fluctuation in the modulation period.

(ii) the strain model : same assumptions as in the step model except different lattice spacings from the bulk values arise due to the coherency strain.

(iii) the composition modulation model : intermixing over some region at interfaces

First we discuss the step model which shows the characteristic features of diffractions of superlattices. The X-ray scattering amplitude of an ideally stacked superlattice is just the sum of the atomic form factor over their relative distances.

$$
\begin{aligned}
F_G &= \int_V f(\vec{r}) exp(i\vec{G} \cdot \vec{r})d^3r \qquad (3.5) \\
\vec{G} &= \frac{2\pi l \hat{z}}{\Lambda}
\end{aligned}
$$
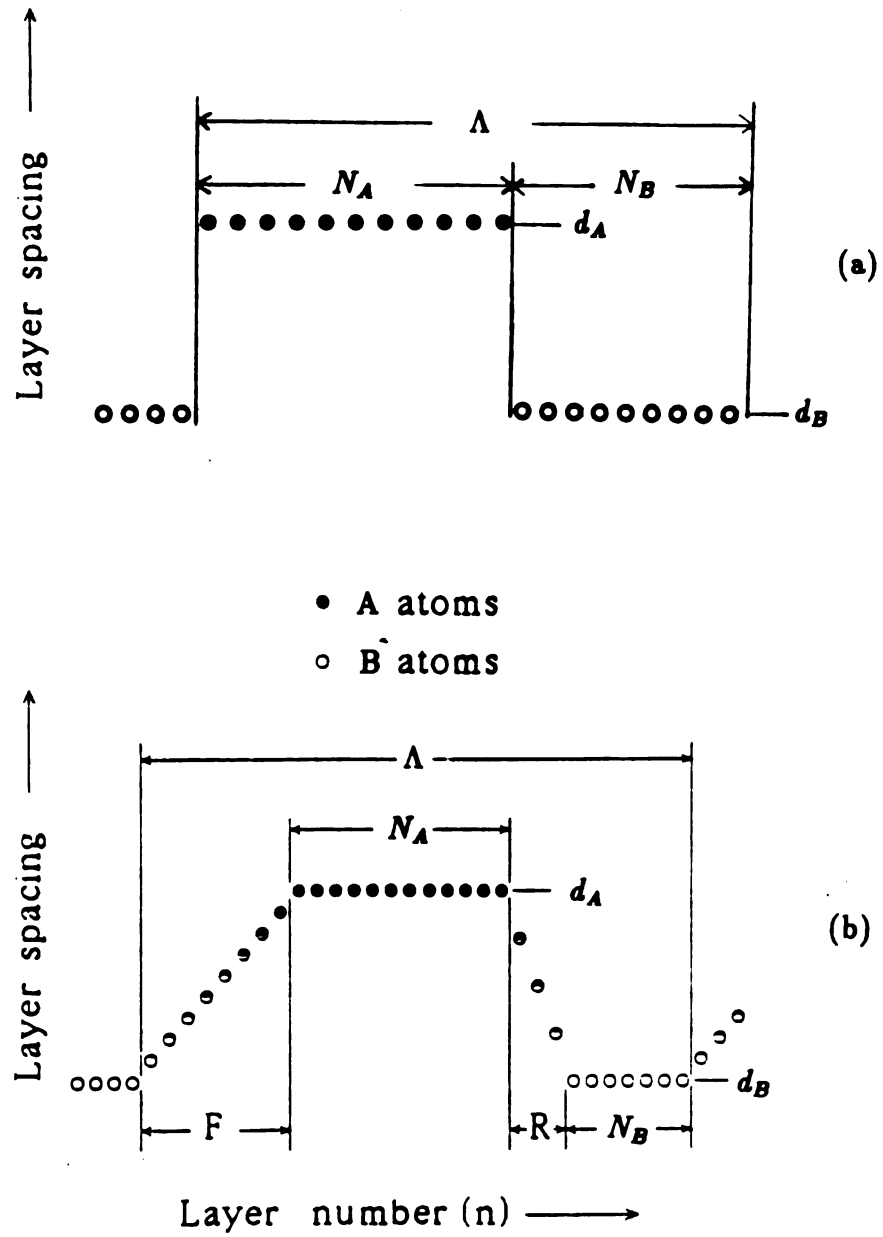
Figure 3.2: One dimensional ideal superlattice model with a perfectly periodic structure. (a) step model (b) trapezoidal composition and d-spacing modulation model.

where $\vec{G}$ is the reciprocal vector of the superlattice with period Λ. In standard reflection geometry, the scattering vector is along the growth direction so that the eq.3.5 can be simplified as

$$
\begin{aligned}
F_q &= \sum_{j=1}^{M} exp(iq(j-1)\Lambda) \int_0^{\Lambda} f(z)exp(iqz)dz \\
&= \frac{\sin(Nq\Lambda/2)}{\sin(q\Lambda/2)}exp[iq\Lambda(N-1)/2][n_A f_A \frac{\sin(qd_A N_A/2)}{\sin(qd_A/2)} \\
&\quad +n_B f_B \frac{\sin(qd_A N_B/2)}{\sin(qd_B/2)}exp(iq\Lambda/2)]exp[iq\Lambda(N_A-1)/2]
\end{aligned} \tag{3.6}
$$

The square of the scattering amplitude is the intensity of the reflected X-ray, and for perfectly stacked superlattice with modulation period Λ and total thickness $N\Lambda$, it is calculated as

$$
I_0(q) = |F(q)|^2 = L_M(q)|S(q)|^2 \tag{3.7}
$$

where

$$
L_M(q) = \sin^2(q\Lambda M/2)/\sin^2(q\Lambda/2) \tag{3.8}
$$

$$
|S(q)|^2 = n_A^2 f_A^2 \sin^2 N_A\alpha/\sin^2\alpha + n_B^2 f_B^2 \sin^2 N_B\beta/\sin^2\beta \tag{3.9}
$$
$$
+2n_A n_B f_A f_B \cos(N_A\alpha + N_B\beta)\sin N_A\alpha \sin N_B\beta/\sin\alpha\sin\beta
$$

Here n_A and n_B are the atomic area densities, f_A and f_B are the atomic form factors of metal A and B respectively, $\alpha = qd_A/2$ and $\beta = qd_B/2$.

In an actual experiment the measured intensity is not the same as eq. 3.6. A number of correction factors affect the actual intensities. They are the Lorentz factor $1/\sin(2\theta)$, the polarization factor $1 + cos^2(2\theta)$, the absorption factor $1 - exp(-2\bar{\mu}t/\sin\theta)$ and the Debye-Waller factor $exp[(-2\bar{B}\sin^2\theta/\lambda^2)]$. Here $\bar{\mu}$ and $\bar{B}$ are the average absorption and Debye-Waller coefficients, respectively. A discussion of these corrections can be found in the book by Cullity.[1] Including the above corrections, the experimental diffraction intensity is given by

$$
I(q) = I_0(q)\frac{1+\cos^2(2\theta)}{\sin(2\theta)}exp(-2\bar{B}\sin^2\theta/\lambda^2)[1-exp(2\bar{\mu}t/\sin\theta)]^{-1} \tag{3.10}
$$

The Laue function $L_M(q)$ is obtained by summing over the number of the bilayer cycles and has its maximum M^2 at equally-distant positions given by integral multiples of $G = 2\pi/\Lambda$ and its width is proportional to $1/M\Lambda$ in momentum space. This

function is shown in fig.3.3 The function $S(q)$ is a layer structure factor reflecting the structure within a bilayer. At low angles the structure factor has large value due to the forward scattering . At high angles the Bragg reflections by individual atomic spacings and their interference enhance the structure factor. The convolution of the Laue function and the square of the structure factor produces reflection X-ray peaks that are characteristic of superlattices. The Laue function, the square of the structure factor and the final X-ray diffraction pattern of (15ML Fe/15ML V)20 are shown in fig.3.3

For more understanding of the step model, we will check the effect of individual layer thickness within a bilayer on the reflection pattern. The first two terms in eq.3.9 are the diffraction functions of layer A and layer B, and the resulting pattern consists of two broad peaks(the width $\propto 1/N_i d_i, i = A, B$) located at angles θ_A and θ_B which satisfy the Bragg conditions

$$2d_A \sin \theta_A = m\lambda \tag{3.11}$$

$$2d_B \sin \theta_B = n\lambda$$

where m and n are integers. The third term in eq.3.9 is an interference term which comes from the overlap of the diffraction peaks at θ_A and θ_B in the angular region between these two angles. If N_A and N_B are small as in fig.3.4 (a), the A and B peaks are broad and there will be considerable overlap, and a single average peak will appear at an angle between θ_A and θ_B. In contrast, if N_A and N_B are large the line widths of peaks A and B are small and the overlap will be negligible. The calculated diffraction patterns in fig. 3.4 clearly show this trend. In this calculation, Fe and Mo are chosen as two constituents and equal numbers of atomic layers of two metals are taken. The lattice spacings are $d_{Fe} = 2.0268\text{Å}$ and $d_{Mo} = 2.2250\text{Å}$, and their Bragg angles are $2\theta_{Fe} = 44.67°$ and $2\theta_{Mo} = 40.51°$ respectively.

Now we consider the effect of the difference in the individual lattice spacings on the X-ray diffraction pattern. If the difference is large the Bragg angles θ_A and θ_B are well separated as we see in eqs. 3.9 and 3.11; the function in eq.3.9 gives individual Bragg lines with small overlap between them. On the other hand, if d_A
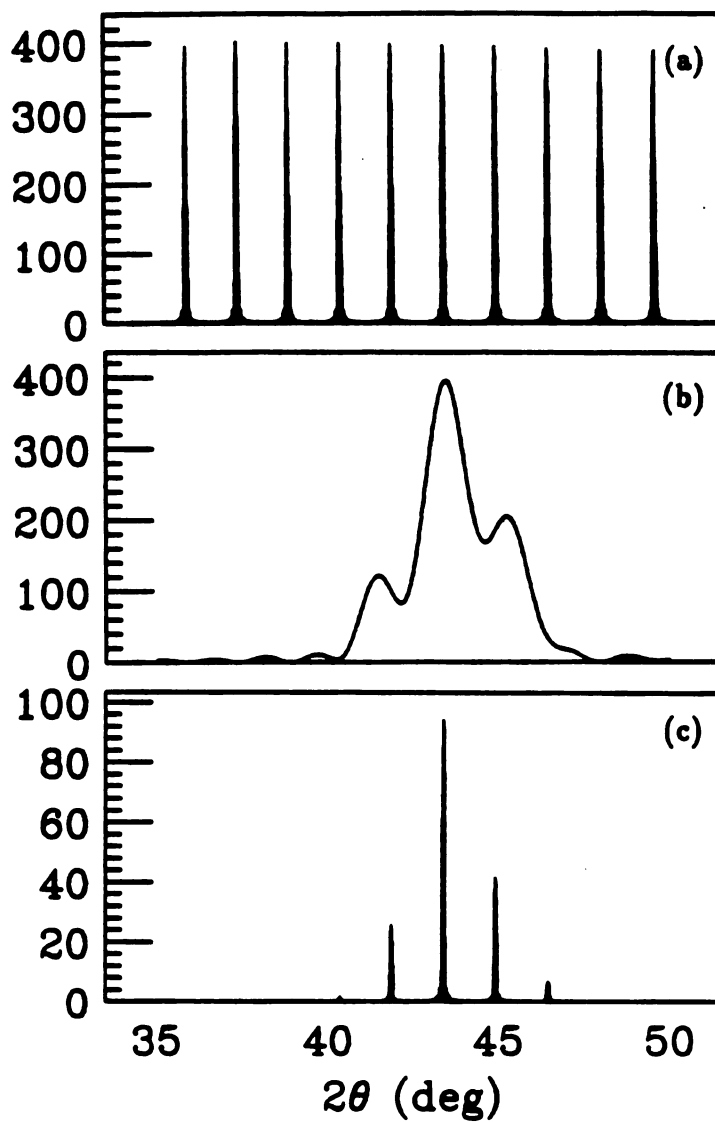
Figure 3.3: Step model calculation of (15ML Fe/15ML V)20. In (a) the Laue function $L_M(l)$ is drawn (b) is the structure factor squared of a bilayer and (c) is the X-ray intensity.

and d_B are very close, essentially only one Bragg line appears. As a result, a large lattice spacing difference enhances the intensities of the satellites surrounding a weak average line, and a small difference develops a strong average line and suppresses the developments of the satellites as shown in fig.3.5 where $\delta = (d_A - d_B)/max(d_A, d_B)$ is the lattice spacing difference and 15 ML of Fe, 15 ML Mo and 20 cycles of bilayers are used.

Until now we have assumed an atomically sharp and abrupt interface. Now, as the final ideal model calculation, we will consider the effects of interdiffusion at the interfaces. The intermixing of atoms at interfaces is quite realistic when two constituent elements are miscible or if the interfaces are atomically rough. Just for the convenience of the calculation we assume a trapezoidal compositional modulation where the atomic concentration and lattice spacing vary linearly over some region of the interfaces. No fluctuation in the period is assumed. The structure factor is calculated by summing up all atoms in the unit bilayer which is divided into 4 regions.(see fig.3.2)

The structure factor is obtained using Eq.3.2

$$S = S_F + e^{iqN_F d}S_A + e^{iq(N_F d + N_A d_A)}S_R + e^{iq(N_F d + N_A d_A + N_R d)}S_B \tag{3.12}$$

where S's are the structure factors of the four regions, d is the average lattice spacing, N_F and N_R are the number of atomic layers with linear composition and the number of atomic layers of pure metals A and B are denoted by N_A and N_B respectively. The structure factors of each region are

$$S_F = \sum^z f_F n_F(x) e^{iqz_o} \tag{3.13}$$

$$S_A = \sum^z f_A n_A e^{iqz_o}$$

$$S_R = \sum^z f_R n_R(x) e^{iqz_o}$$

$$S_B = \sum^z f_B n_B e^{iqz_o}$$
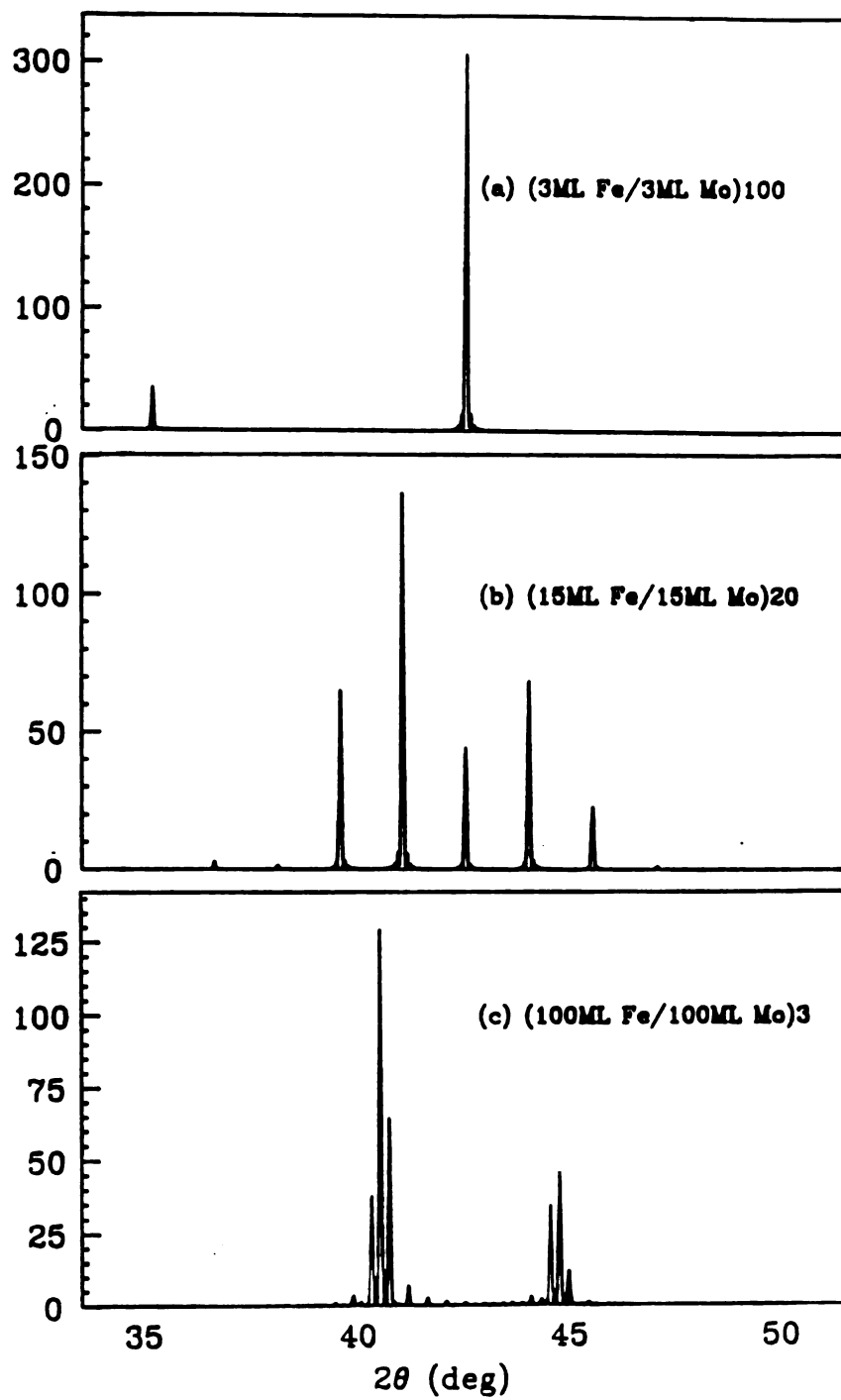
Figure 3.4: Step model calculation demonstrating the effect of the layer thickness .
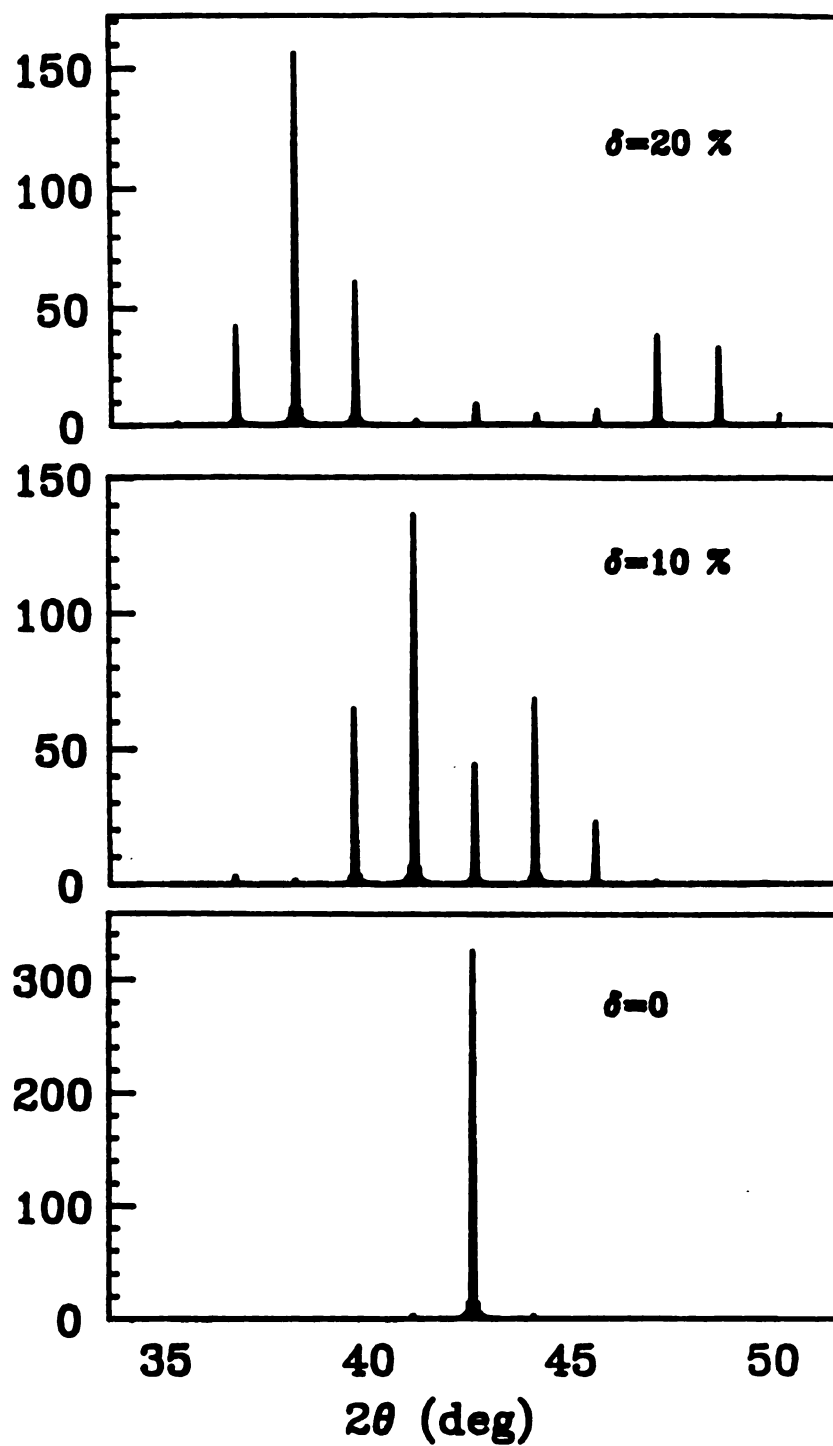
Figure 3.5: Step model calculations of (15ML Fe/15ML Mo)20 demonstrating the effect of the relative difference in lattice spacings, δ.

where the atomic scattering factors in each region are

$$f_F = (f_A - f_B)\frac{x}{N_F + 1} + f_B \qquad (3.14)$$

$$f_A = f_A$$

$$f_R = (f_B - f_A)\frac{x}{N_R + 1} + f_A$$

$$f_B = f_B$$

n_F, n_R are linear functions of the atomic area density at the interface regions and z_x is the position of the x-th atomic plane within each region. The square of eq.3.12 gives the intensity for a unit bilayer ;this function becomes the new $|S(q)|^2$ in eq.3.8. Results for a step model and a trapezoidal model of interfaces are compared in fig. 3.6. The major effect of interdiffusion at the interface is a reduction in satellite intensities.

3.2.2 Nonideal superlattices

The previous results given for composition models have had very sharp reflection lines because perfect periodicity has been assumed and thus the total thickness $M\Lambda$ was the coherence length. But in most metallic superlattices, the experimentally observed high angle reflection lines are much broader than those predicted by simple one dimensional models, such as the "step" and the "strain" model. Typical perpendicular structural coherence lengths(PSCL) in the growth direction of our metallic superlattice samples are about $200\mathring{A}$, ranging from a few Λ's to nearly 10Λ's. The PSCL is much shorter than the total sample thickness of $\sim 1800\mathring{A}$, indicating that some mechanisms are decreasing the long range order. Several mechanisms which can cause this decrease are

(1) imperfections in the deposition process

(2) geometric constraints at the interfaces due to the difference in the lattice parameter and symmetry

(3) variations in growth mode and wetting

(4) interdiffusion and alloying

Practically all these mechanisms would limit the accurate control over the thick-
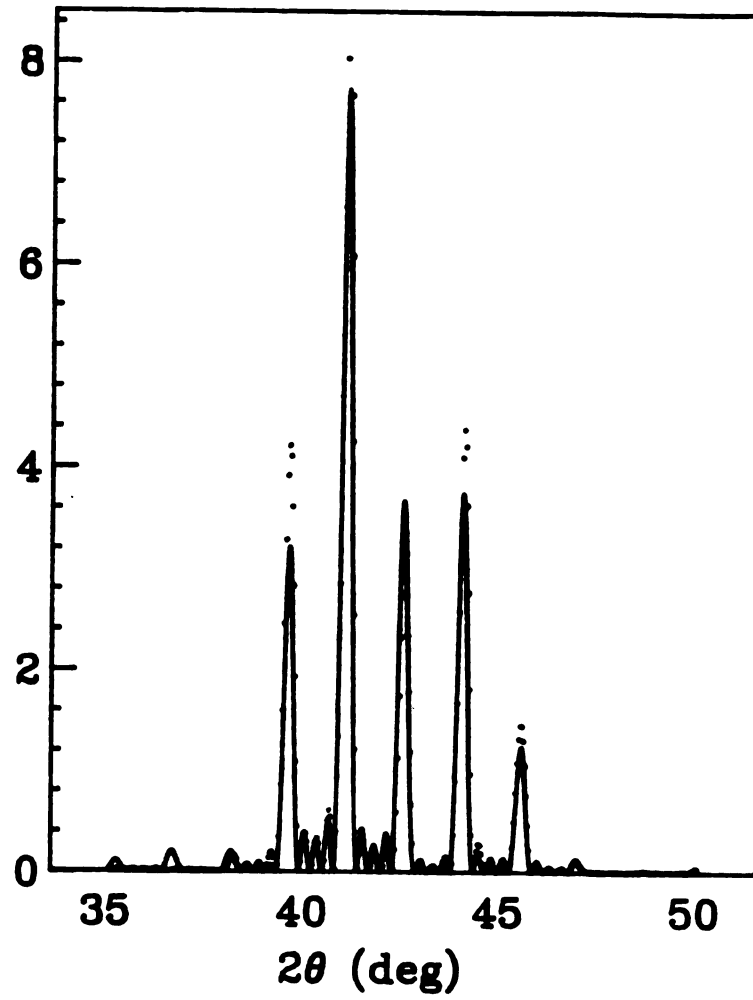
Figure 3.6: Trapezoidal composition model(solid line) and step model(dotted line). $N_A = N_B = 10$ ML, $N_F = N_R = 5$ ML. Intermixing reduces the intensities of the satellites.

nesses of the individual layers by at least a few percent.

Recently X-ray model calculations assuming imperfect periodicity have been done by two groups. Structural imperfections can be modeled as (i) a continuous layer thickness distribution associated with the amorphous layer in a Crystalline/Amorphous system[2][3] (ii)a discrete distribution for the number of atomic planes in the layers of a Crystalline/Crystalline system[3] [5] and (iii) a continuous fluctuation of the interface distance(the distance between unlike atoms) due to the lattice mismatch.[4][5] Clemens and Gay[3] assumed fluctuations of a Gaussian type, continuous thickness fluctuations for amorphous layers and discrete thickness fluctuations in crystalline layers, and made kinematical X-ray diffraction calculations. The intensity is

$$I(q) = |D(q)|^2 |S(q)|^2 \tag{3.15}$$

$S(q)$ is the layer structure factor which is the same as in eq.3.2, $D(q)$ is the Fourier transform of the layer distribution function. For amorphous layers having a continuous layer thickness distribution described by a Gaussian distribution of half-width σ about the average thickness c,

$$|D(q)|^2 = N + 2 \sum_{n=1}^{N-1} (N - n) \cos(n(N_A d_A + c)q) exp(-n\sigma^2 q^2/4) \tag{3.16}$$

For a discrete thickness distribution where one of the layer thicknesses differs from the average c by md with a probability $exp(-m^2 d^2/\sigma^2)$ and m is a integer,

$$\begin{aligned} |D(q)|^2 &= N + 2 \sum_{n=1}^{N-1} (N - n) \cos(n(N_A d_A + c)q) \\ &\times [1 + 2 \sum_{m=1}^{\infty} exp(-m^2 d^2/n\sigma^2) \cos(mdq)] \end{aligned} \tag{3.17}$$

Calculated intensities using eq.3.16 are illustrated in fig. 3.7 for a 20ML Fe layer and a 50Å multilayer system. Sharp reflection lines are developed(fig. 3.7 (a)) with zero fluctuation and as the distribution width σ increases the lines rapidly become broad. With a σ of 4% for the amorphous layer thicknesses only the finite thickness Fe layer broadened line occurs and there is no trace of superstructure. We will see this kind
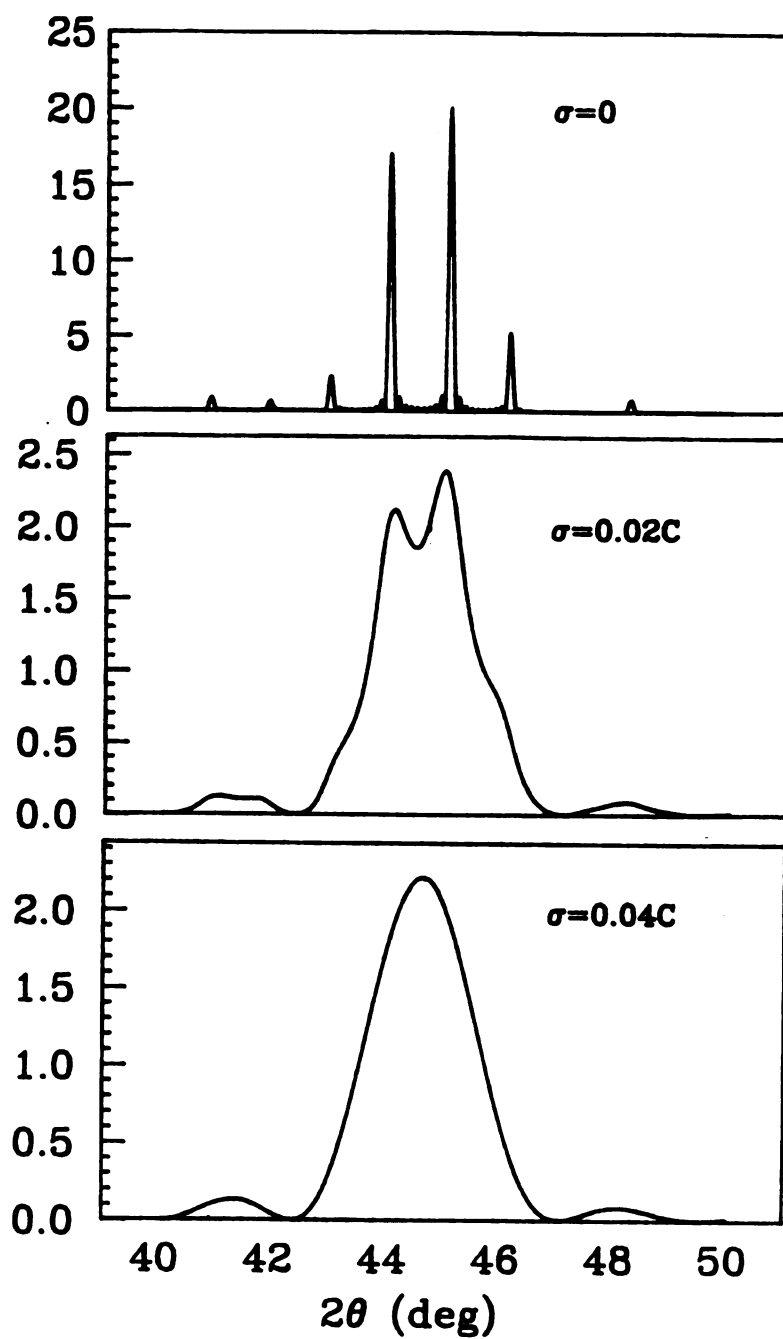
Figure 3.7: Model calculations with continuously distributed amorphous layer thicknesses. σ is the width of the Gaussian distribution and c is the thickness of the a-Si layer. (20ML Fe/50$\AA$ a-Si)10.

of behavior in our Fe/Si system which will be discussed in the next section. On the other hand, the diffraction intensity for a discrete fluctuation of layer thicknesses shows superlattice peaks due to the superlattice structure image in eq.3.18. Fig.3.8 illustrates the calculation of (15 ML Fe/15ML Mo)20 for 3 values of the discrete distribution width σ where σ is given in units of the lattice spacing of Mo. The reflection peaks remain rather sharp even for a considerable discrete distribution width. This is the case for Crystalline/Crystalline multilayers such as Fe/Mo and Fe/V systems in next section.

Locquet et al.[4] assumed that the distance at the interface between unlike atoms fluctuates around an average value d following a continuous, Gaussian distribution of width σ. They state, "The origin of this fluctuation can be the perpendicular lattice mismatch $\delta = (d_A - d_B)/max(d_A, d_B)$, with d_A and d_B the lattice spacings of the constituents, which is correlated with the in-plane lattice parameter difference. The geometric conditions imposed by the latter create a "rough" interface, with large (atoms A forced on top of atoms B) and small (atoms A "falling" in between atoms B) interface distances, assumed to follow a Gaussian distribution around an average value d." They note that this assumption is strictly correct for incommensurate systems and only approximately correct for systems that have a long-distance commensurate relationship. Incommensurate is understood to mean a small PSCL. The total intensity is given by

$$
\begin{aligned}
I_0(q) \;=\; & N[A^2 + B^2 + 2AB exp(-q^2\sigma^2/4)\cos(q\Lambda/2) \\
& +2\sum_{m=1}^{N-1}(N-m)((A^2 + B^2)exp(-2mq^2\sigma^2/4)\cos(2mq\Lambda/2) \\
& +AB exp[-(2m+1)q^2\sigma^2]\cos[(2m+1)q\Lambda/2] \\
& +AB exp[-(2m-1)q^2\sigma^2/4]\cos[(2m-1)q\Lambda/2)])
\end{aligned}
\tag{3.18}
$$

with

$$
A \;=\; f_A\sin(N_A q d_A/2)/\sin(q d_A/2)
$$

$$
B \;=\; f_B\sin(N_B q d_B/2)/\sin(q d_B/2)
$$

For $\sigma = 0$, eq.3.18 reduces to the step model, while for $\sigma = \infty$ it reduces to the
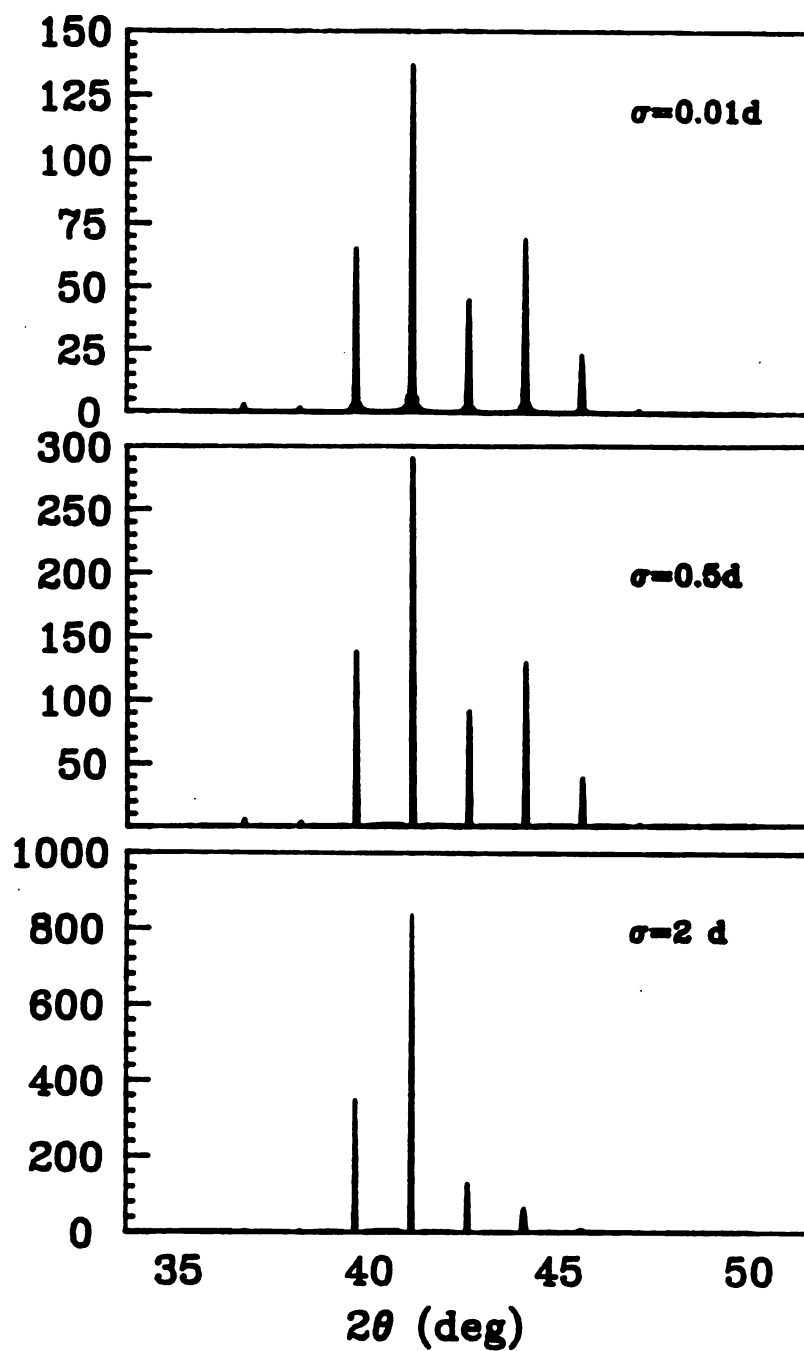
Figure 3.8: The effect of the discrete fluctuation of layer thickness in high angle X-ray diffraction of (15ML Fe/15ML Mo)20.

scattering of two independent blocks of materials A and B without any trace of superstructure. Using eq.3.18, the high angle X-ray diffraction patterns of a (15ML Fe/15ML Mo)20 multilayer was calculated for different values of distribution width σ. A drastic decrease of the peak intensities together with an increase of the linewidths occurred with increasing σ and is shown in fig.3.9.

3.3 Experimental data(X-ray and TED)

3.3.1 Measurements of basic sample parameters

Among the structural parameters potentially available from standard reflection XRD, two basic sample parameters are most easily obtained. They are the modulation period Λ, and the average lattice spacing d_{AVG}. As we discussed in section 3.3 the positions of the reflection lines from the superstructure are determined by the Laue function $\sin^2(q\Lambda M/2)/\sin^2(q\Lambda/2)$ which has sharp peaks when the Bragg condition for the modulation period Λ is satisfied.

$$2\Lambda \sin \theta = n\lambda \tag{3.19}$$

$$n = 1, 2, 3, \cdots$$

We can rewrite this equation as

$$q = \frac{2\pi}{\Lambda} n \tag{3.20}$$

where $q = \frac{4\pi}{\lambda} \sin \theta$ is the magnitude of the scattering vector. We get the modulation period from eq.3.20. The average lattice spacing d_{AVG} is

$$d_{AVG} = \frac{N_A d_A + N_B d_B}{N_A + N_B} = \frac{\Lambda}{N_A + N_B} \tag{3.21}$$

so the average Bragg line occurs when $n = N_A + N_B$ in eq.3.19 or eq.3.20. In fig.3.10. experimental X-ray diffraction data are shown, (a)low angle harmonics (b)an average line at $2\theta = 42.32°$ with satellites surrounding the average line. Hereafter the term harmonics denotes reflection lines at low angle and satellites denote the high angle peaks surrounding the average Bragg peak. The nominal parameters of this sample are $(30.4 \mathring{A} Fe/33.4 \mathring{A} Mo)28$ which were intended to make a (15ML Fe/15ML Mo)28
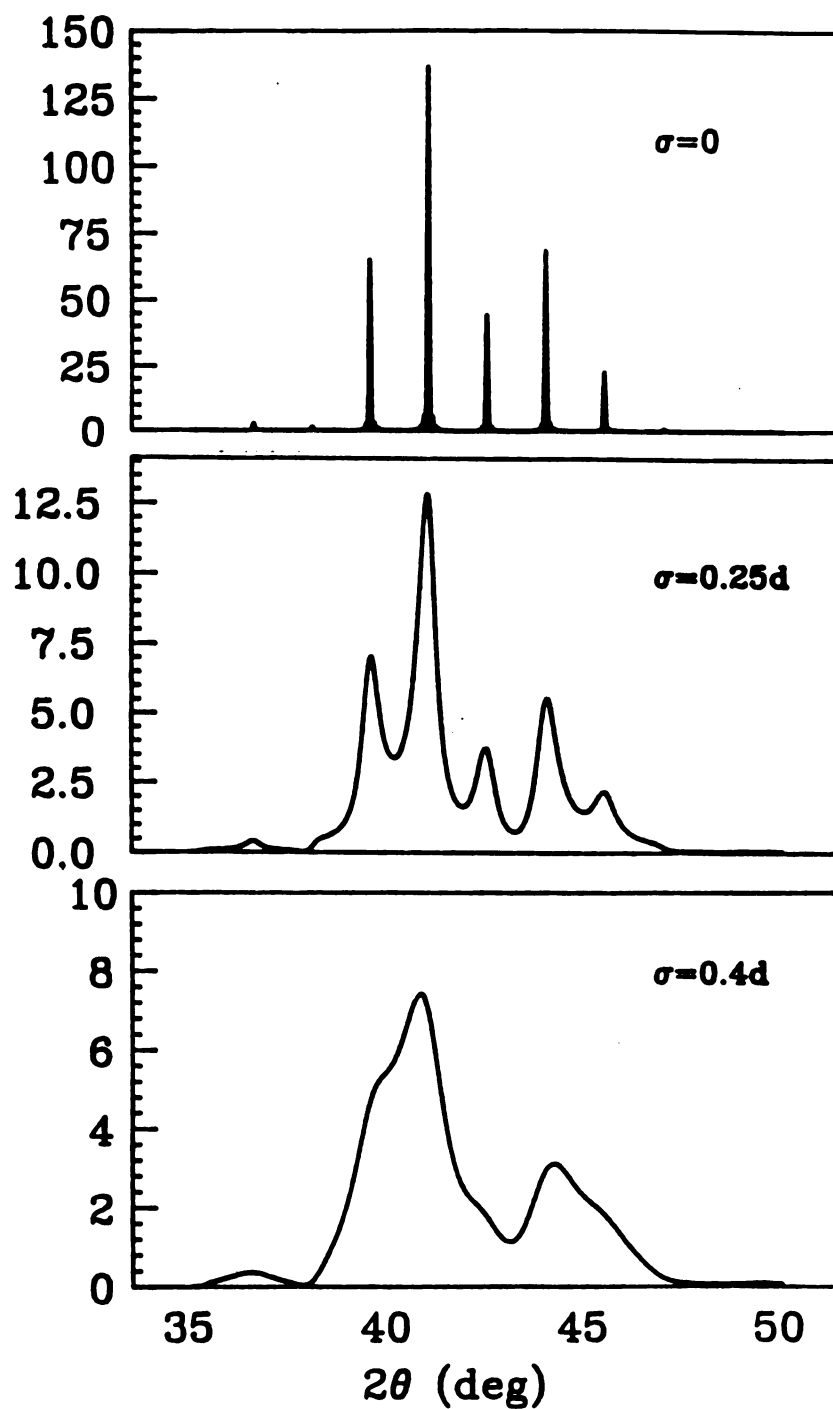
Figure 3.9: Evolution of simulated high-angle spectra of (15ML Fe/15ML Mo)20 for crystalline layers having a continuous distribution of interface distances. The half width σ is given in units of the d-spacing of Mo layer.
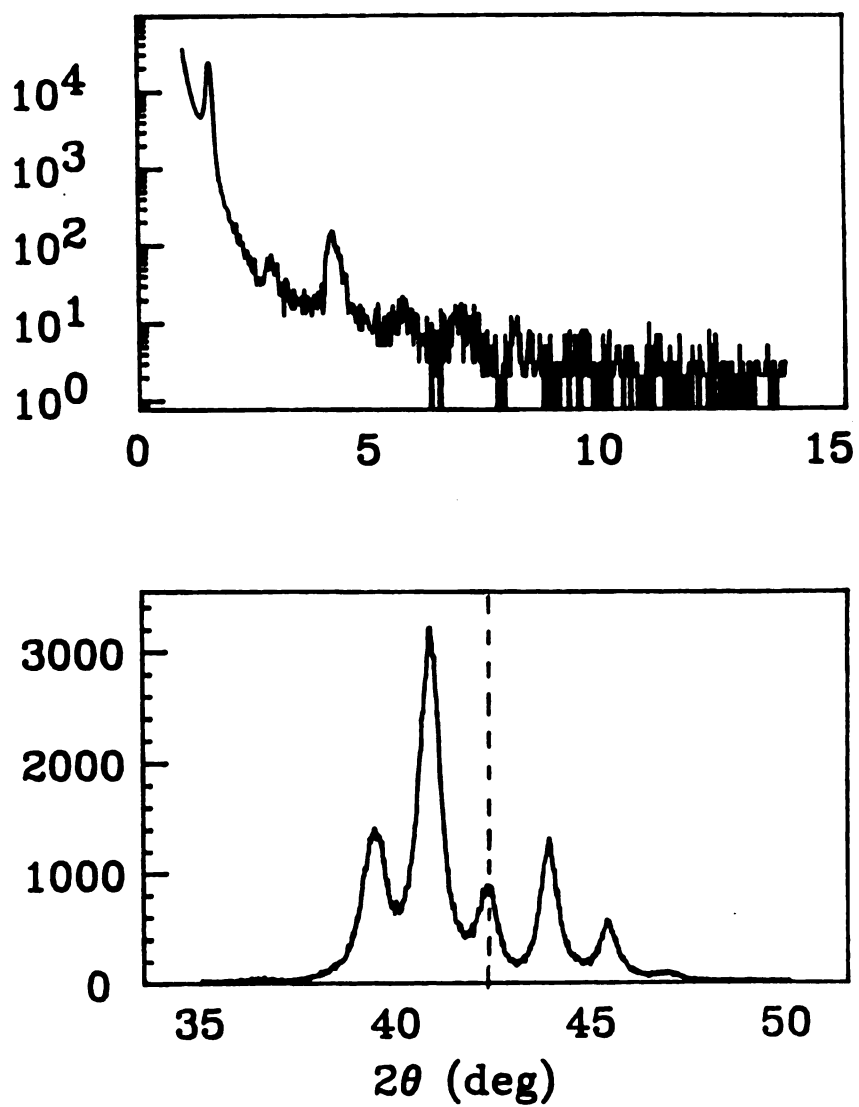
Figure 3.10: Experimental diffraction spectra of a sample with nominal parameters (15ML Fe/15ML Mo)28 (a)harmonics (b)satellites. The average line is denoted by a vertical line.

sample with BCC(110) texture. The high angle spectrum of this sample is very close to the pattern of step model calculation (see fig.3.4(b)) where we used the lattice parameters of bulk Fe and bulk Mo assuming (110) texture in growth direction. The closeness of experimental spectra and model calculation confirms the successful growth of multilayers as designed. The observed average lattice spacing from the position of the average line is $d_{obs} = 2.134\text{Å}$, whereas the bulk value is $d_{bulk} = 2.126\text{Å}$ with $d_{Fe}(110) = 2.0268\text{Å}$ and $d_{Mo}(110) = 2.225\text{Å}$. [6]

It is often convenient to index the high angle satellites with respect to the average line instead of the absolute index as in eq.3.20. Let m be the satellite index such that m=0 for the average line which is $n = N_A + N_B$ in eq.3.20. Then eq.3.20 can be rewritten as

$$q = \frac{2\pi m}{\Lambda} + q_{AVG} \qquad (3.22)$$

In fig.3.11, we plot the experimental data of fig.3.10 as q versus m. The plot is linear as expected and the slope is $2\pi/\Lambda$ if the sample is adequately layered. The measured modulation period Λ from the slope is $\Lambda_m = 63.6\pm0.5\text{Å}$ and the same plot with low angle harmonics gives the value $\Lambda_m = 64.7 \pm 0.5\text{Å}$. The nominal value is $\Lambda_n = 63.8\text{Å}$. In most our samples, values of Λ determined from harmonics, satellites and nominal preparation parameters agree to within 5% or less with the exception of several times when the crystal thickness monitor was miscalibrated.

We will demonstrate the accuracy of Λ's obtained from the above methods by obtaining the total film thickness using another, independent method. As noted earlier, the samples prepared for TED are very thin ($\sim 500\text{Å}$) on a NaCl substrate. Due to the interference between the X-rays reflected at the outer surface of film and the X-rays scattered by the surface of substrate, fine oscillations are observed in very thin films at low angles. Fig.3.12(a) shows the fine oscillation from the total thickness of a very thin sample on a NaCl substrate. The pronounced peak at $2\theta = 4.2°$ is the first order Bragg line of Λ.

For the small oscillations the following relation holds. [7]

$$\theta_m^2 = 2\delta + (m + k)^2 \frac{\lambda^2}{4t^2} \qquad (3.23)$$
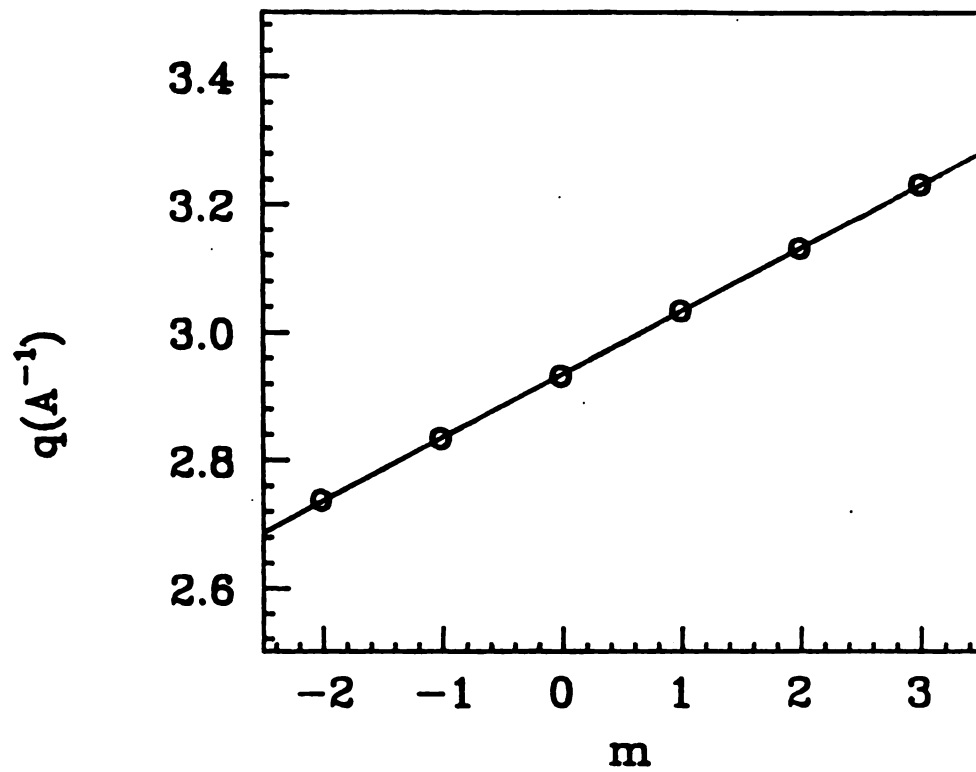
Figure 3.11: The plot of satellite data for sample #199-1 as q versus m. The slope is $2\pi/\Lambda$.

where θ_m is the position of the m-th peak in units of radians, $\delta = Re(1-n)$, n is the refractive index of the film, k=0 or $\frac{1}{2}$ for minima or maxima, respectively, and t is the thickness of the film. The data points of the small oscillations of sample #187-2 are plotted as θ_m^2 versus $(m+k)^2$ in fig.3.13. The slope of the linear line is $\lambda^2/4t^2$ according to eq.3.23. The film thickness from the slope is $t = 507\overset{\circ}{A}$.

The nominal parameters of the sample (sample number #187-2 and it is sputtered on NaCl for the TED study) are $(6.1\overset{\circ}{A}$ Fe$/13.4\overset{\circ}{A}$ Mo)23 and produce the nominal total thickness of $462\overset{\circ}{A}$. High angle diffraction data for this sample in fig.3.12(b), are rather weak due to the small sample volume, but clearly show the average peak and a satellite. The measured period using eq.3.22 is $\Lambda_m = 21.5\overset{\circ}{A}$. Using the measured period Λ_m and the number of cycles produces $t = 508\overset{\circ}{A}$ including a $13.4\overset{\circ}{A}$ Mo overlayer on top. Two independent methods of obtaining the total thickness give excellent agreement. In this particular sample, the nominal thickness $(t = 462\overset{\circ}{A})$ differs from the actual thickness by 9%. This relatively large discrepancy is typical of samples having a few ML individual layers, and suggests the difficulty of accurate thickness control with such thin layers.

3.3.2 Fe/a-Si system (Crystalline/Amorphous)

In all Fe/Si multilayers the thickness of the Si layer is fixed either at $50\overset{\circ}{A}$ or at $30\overset{\circ}{A}$. The low angle XRD data clearly show a number of harmonics, ranging from 3 to 6, which indicate that our samples are compositionally modulated.(fig.3.14). But when we look at the high angle XRD data in fig.3.15 there are no satellites at all, only a broad Fe(110) Bragg line appears in all Fe/Si multilayers. The peaks at about 42° are the Bragg lines from sapphire substrates. The lack of Bragg peaks for crystalline Si, even though the Si layer is relatively thick indicates Si is amorphous in our Fe/Si multilayers.

Another special feature in Fe/Si multilayer systems is the fact that the measured period Λ_m is always smaller than the nominal period Λ_n by 10% in samples with nominal Si thickness of $30\overset{\circ}{A}$, and 15% in samples with nominal Si thickness of $50\overset{\circ}{A}$. This fact is special because the opposite behavior, i.e. $\Lambda_m > \Lambda_n$, is observed
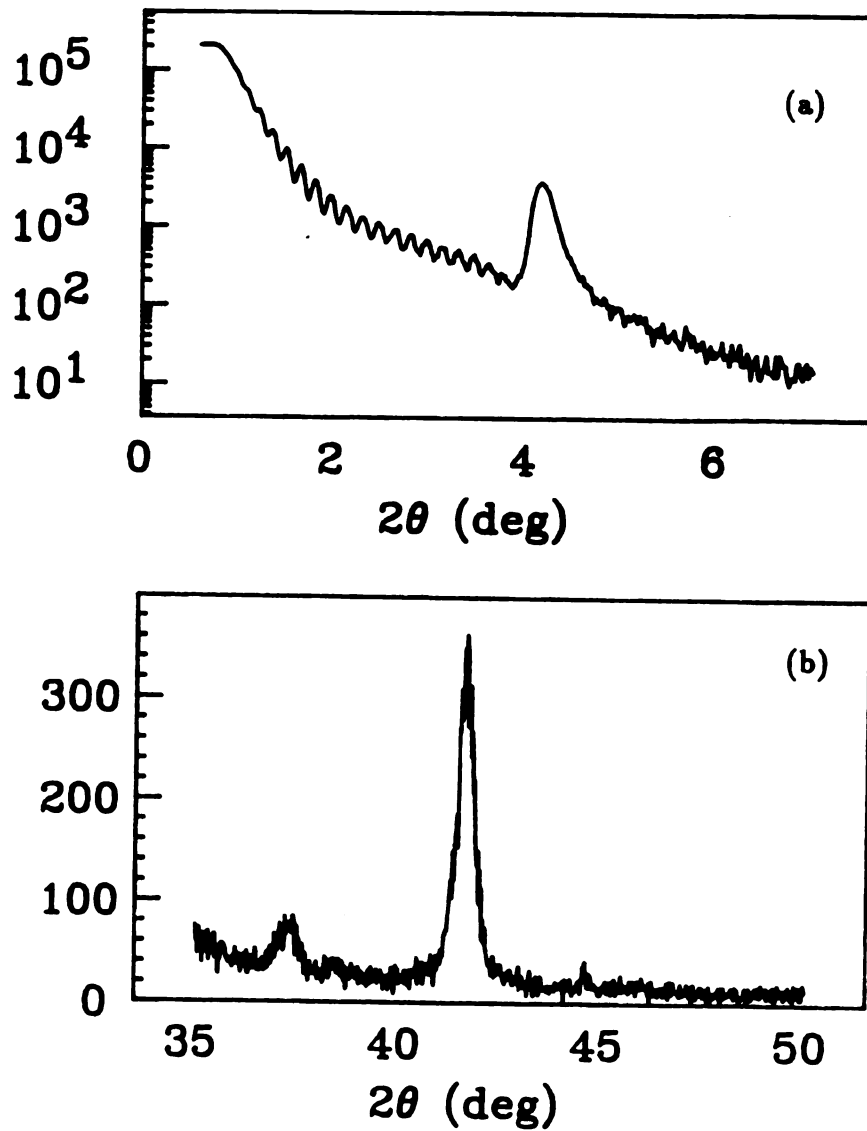
Figure 3.12: (a)low angle and (b)high angle X-ray diffraction of a sample ,#187-2, with a nominal thickness of $462\mathring{A}$.
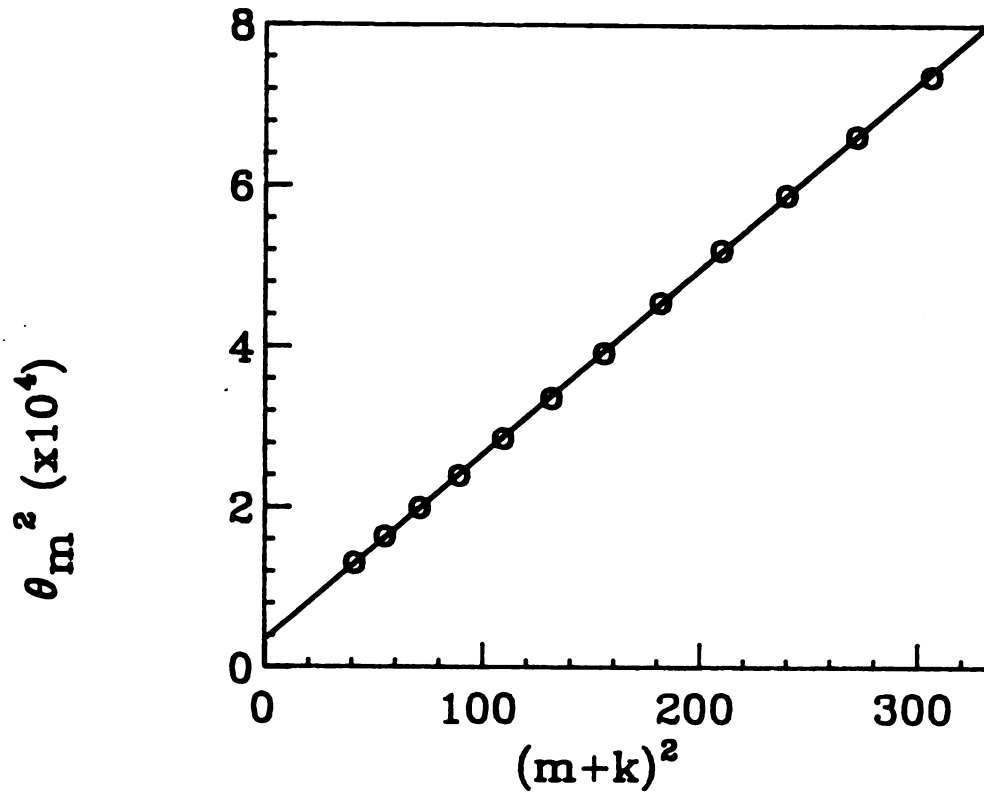
Figure 3.13: plot of the data point of small oscillation of sample #187-2 as θ_m^2 vs. $(m+k)^2$. The slope is $\lambda_z^2/4t^2$.

for all other Fe/metal multilayer systems due to the extra exposure of substrates to the atomic beam during the motion of the SPAMA plate. Since the densities of crystalline materials were used for crystal thickness monitor, it is expected that the density of amorphous Si is larger than that of crystalline Si.

The Fe(110) lines are evident and become systematically broader and weaker as the Fe thickness decreases. The structural coherence length from the FWHM of these peaks is always less than but comparable to the Fe layer thickness. The disappearance of satellites in the Fe/Si systems can be explained by a continuous distribution of the amorphous Si layer thicknesses. As we saw in section 3.3 fig.3.7, a Gaussian type layer thickness fluctuation with a distribution width of 5% of the layer thickness completely wiped out the high angle satellites and left only a broad Fe(110) line.

Suppose we have M Fe layers, the positions of layers are randomly located and each individual layer has n atomic monolayers. This system can be a rough model for our Fe/Si multilayer. If the amplitude of X-rays scattered by an atomic layer is A, then the X-ray intensity from a Fe layer is proportional to n^2A^2 because n atomic layers within individual Fe layer are stacked regularly and constructive interference occurs at the Bragg angle. But the Fe planes in one layer are not arranged in a regular fashion relative to the planes in neighboring layers and thus the X-rays scattered by them would have random phases. Then the intensity of the waves scattered by the whole system is proportional to $M(n_{Fe}A)^2$.

$$I = Mn_{Fe}^2A^2 + B \qquad (3.24)$$

where B is a background signal. In fig.3.16 the integrated intensities of the Fe(110) Bragg lines in fig.3.15 are plotted versus the Fe thickness squared. They are quite linear indicating eq. 3.24 explains the systematic change of the intensities. Near Fe layer thickness of 12ML this Fe(110) peak is lost in the background signal but TED data indicate that the Fe is still crystalline. The TED data of Fe/Si samples that illustrate behavior as the Fe thickness decreases are given in fig.3.17.[8] For 20 ML Fe layers a BCC pattern with a strong Fe(110) Bragg line is evident. As the Fe
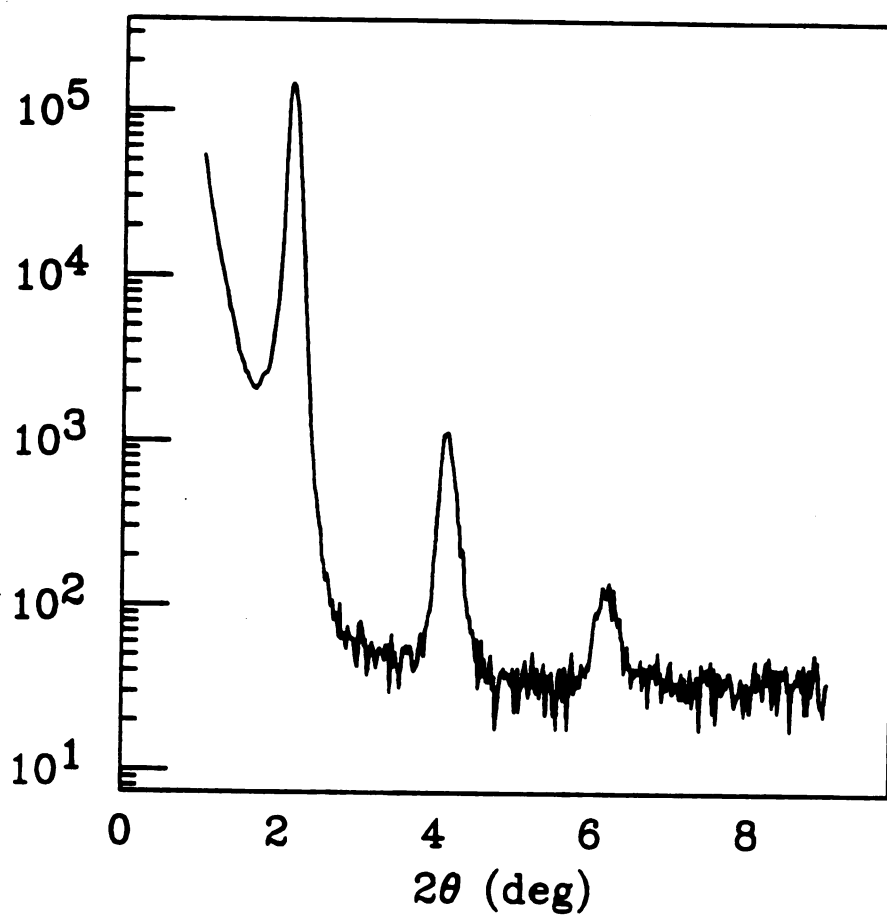
Figure 3.14: The low angle harmonics of $(18\mathring{A}Fe/50\mathring{A}Si)40$ which indicate the compositional modulation.
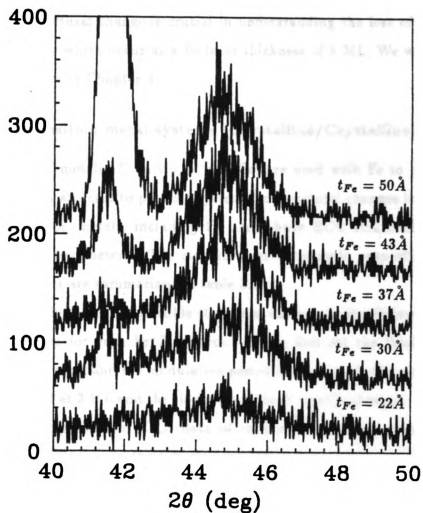
Figure 3.15: The high XRD of Fe/50Å Si. No satellites are visible and the finite size broadening is evident. Sapphire Bragg lines are seen at about 42°.

layer thickness decreases while the Si thickness remains constant the higher-index Bragg lines broaden, merge and finally disappear. This systematic variation clearly indicates that long range order is lost as Fe thickness decreases. All these data are consistent with the formation of structurally isolated, crystalline Fe layers in our Fe/Si multilayers. But TED data suggest a crystalline to amorphous transition as the Fe thickness decreases to about 5 ML.

This structural change is crucial in understanding the loss of magnetism in Fe/Si multilayers which occur at a Fe layer thickness of 5 ML. We will discuss this loss of magnetism in Chapter 4.

3.3.3 Fe/transition metal systems (Crystalline/Crystalline)

Three transition metals, X = Mo, V and Cr, are used with Fe to prepare Fe /X multilayers in an attempt to produce systematic structural changes in the Fe layers. All four transition metals, including Fe itself, have BCC structure in bulk with different lattice parameters. The structural and magnetic properties of elements used in this thesis are summarized in table 3.1.

To more fully explore possible structural changes in the Fe layer we prepared 2 sets of samples for each Fe/X system. In the first set the thicknesses of two constituents are equal and the modulation period is changed; in the second set the Fe thickness is fixed at 3 ML and the thickness of the X layer is changed. In this section some selected experimental XRD data of each system will be presented. Initial interpretation focuses upon the achievement of adequate compositional modulation, and then an interpretation of high angle satellites for the presence of coherency strain will be given. Finally the direct observations of strained layer superlattices(SLS) using TED data are given.

In fig.3.18 and fig.3.19 the low angle and high angle XRD data for (3ML Fe/t_{Mo})M are illustrated. (t_{Mo}=3 ML, 8 ML and 12 ML) At least two harmonics are seen at low angles(the second order harmonic of 3 ML Fe/3ML Mo is out of range in fig.3.18) and a strong average line plus satellites are observed at high angle. Note that even the 3 ML Fe/3 ML Mo sample has both harmonics and satellites
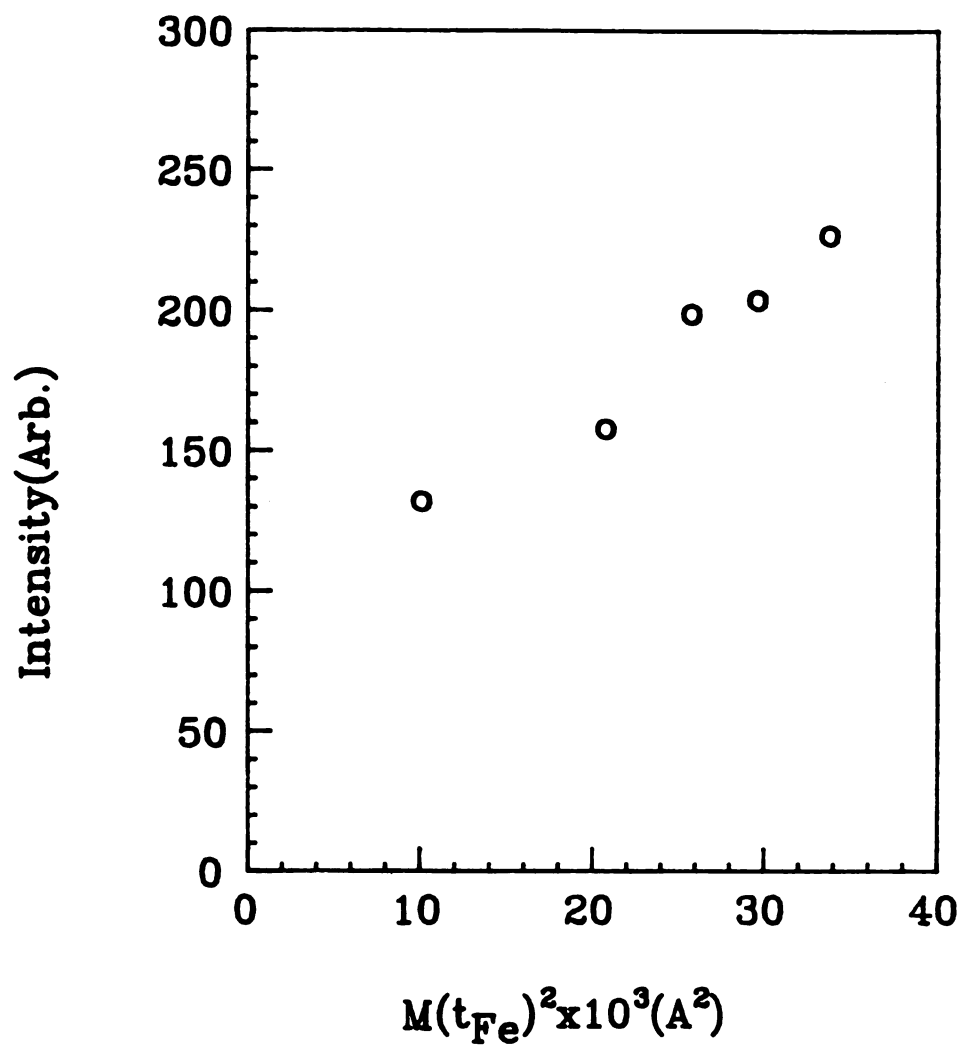
Figure 3.16: Data plot of the intensities of Fe(110) lines versus Fe thickness squared.
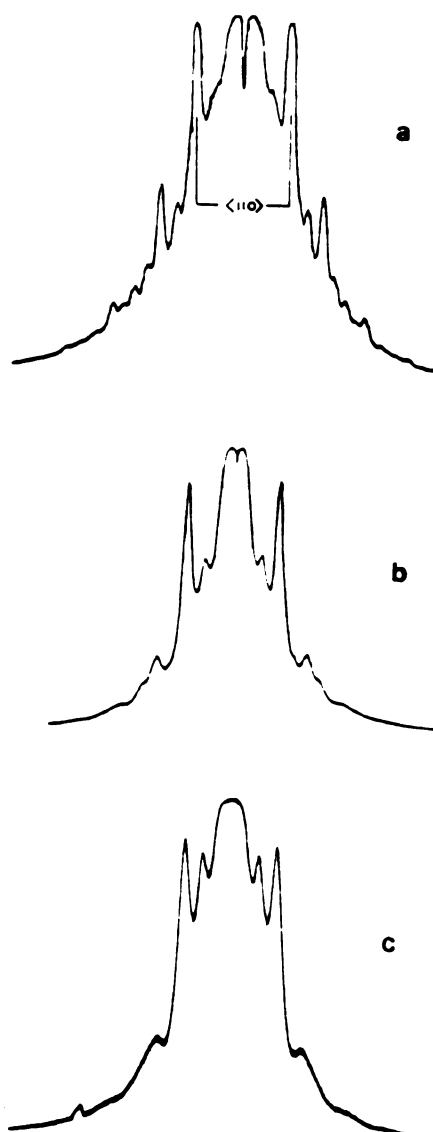
Figure 3.17: TED data of Fe/Si multilayer systems. The Fe layer thickness are 20 ML(a) 12 ML(b) and 4 ML(c). After C. L. Foiles

Element	Structure	$a(\overset{\circ}{A})$	$d(110)(\overset{\circ}{A})$	δ	Magnetic property
Fe	BCC	2.8663	2.0268	0	Ferromagnetic
Mo	BCC	3.1467	2.2250	8.91%	Paramagnetic
V	BCC	3.0281	2.1412	5.34%	Paramagnetic
Cr	BCC	2.8844	2.0396	0.6%	Antiferromagnetic
Si	Amorp.	.	.	.	Diamagnetic(Cryst.)

Table 3.1: Structural parameters of elements used for the metallic multilayers in this thesis and their magnetic properties. From the CRC Handbook of Chemistry and Physics 66th ed. 1985.

indicating strong compositional modulation. The systematic shift in the positions of average lines toward low angle indicates an increase of the average lattice spacing as the Mo thickness increases.

The high angle XRD data in fig.3.20 are from three equal layer Fe/Mo samples (a) (15 ML Fe/15 ML Mo)28 (b) (11 ML Fe/11 ML Mo)38 and (c) (3 ML Fe/3 ML Mo)140 respectively. More satellites are developed as the layer thickness increases consistent with the model calculation results given in fig.3.4. Note that the positions of the average lines are almost constant at $2\theta = 42.3°$ for all samples. XRD data of the Fe/Mo systems, in both the locations of average lines and the systematic shifts in peak locations, are all consistent with expectations of Crystalline/Crystalline metallic multilayers. BCC structure with (110) texture along growth direction in each ultrathin metallic layer is confirmed by the XRD data. XRD data of the Fe/V and Mo/V(made for a superconductivity study) systems showed similar behavior to that of the Fe/Mo systems and will not be given separately. The average d-spacings calculated from the average Bragg lines of various metallic multilayers are plotted as functions of the unit bilayer thickness in fig.3.21. Samples with equal ML thicknesses of each constituent were used in this plot. The horizontal lines near each data sets denote the average spacings from the tabulated bulk lattice parameters assuming (110) texture in all layers. The observed average spacings of the systems are very close to the bulk average d(110) spacings indicating (110) texture in individual layers. Generally the observed points lie a little higher than the bulk values and this can be explained by the strains in the ultrathin layers which will be discussed in the next section.

3.3.4 Observation of metallic SLS

A more detailed characterization of ultrathin layers is needed. It is expected that individual layers in multilayers with large modulation period would have their own bulk structural properties. But if the layer thicknesses become ultrathin (a few tens of $\mathring{A}$) one anticipates strains in the layers due to the lattice mismatch between the two constituents. Very thin metallic layers grown on a substrate have been reported
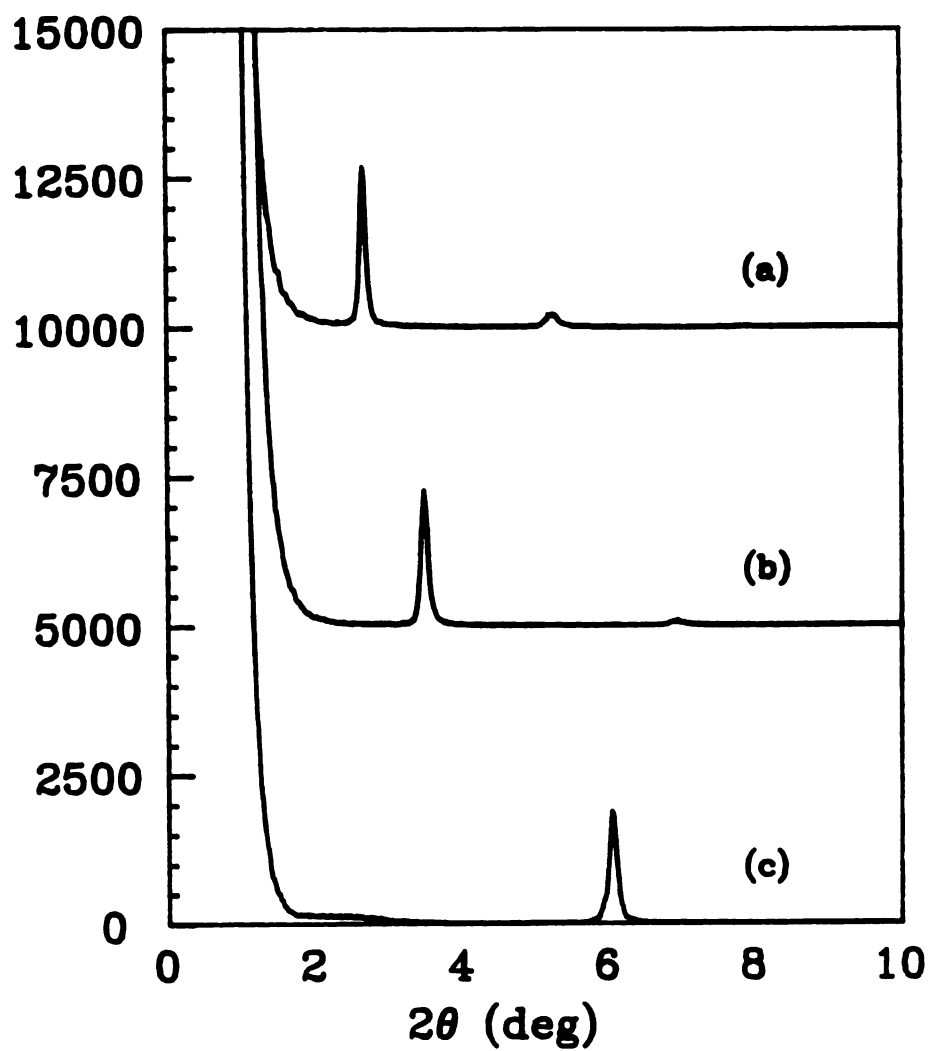
Figure 3.18: Low angle harmonics of (3 ML Fe/t_{Mo} Mo)N samples. (a)t_{Mo}=12 ML (b)t_{Mo}=8 ML (c)t_{Mo}=3 ML.
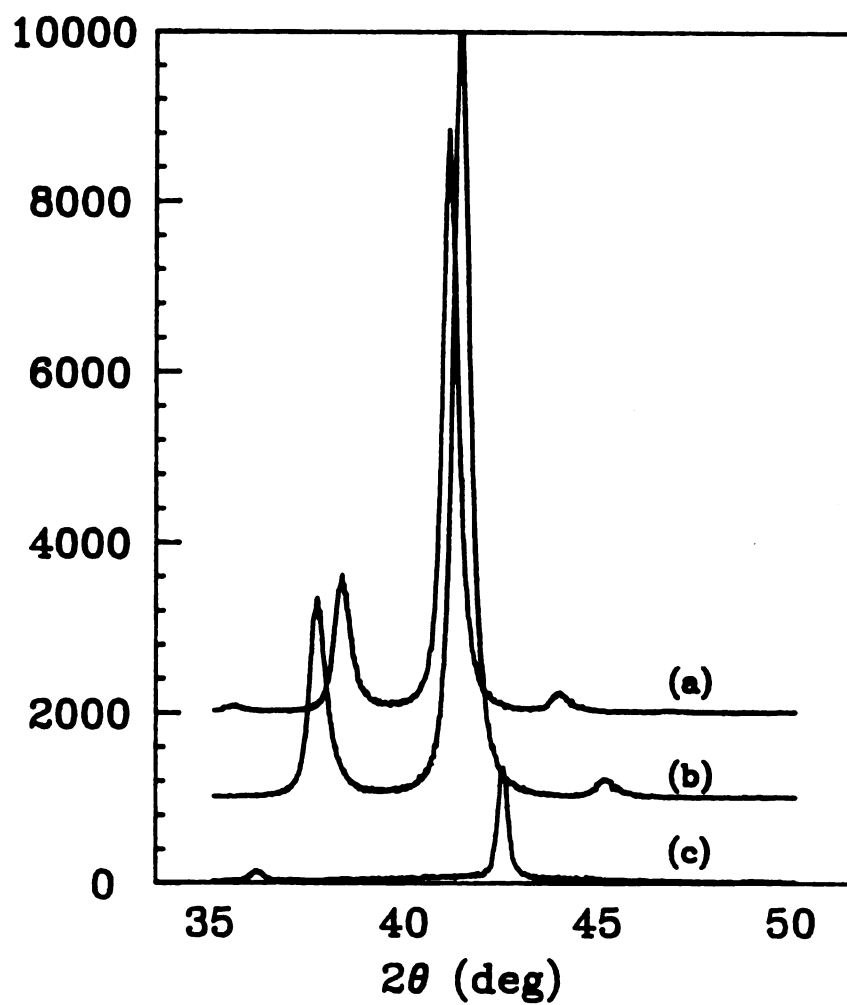
Figure 3.19: High angle reflection lines of (3 ML Fe/t_{Mo} Mo)M samples. (a)$t_{Mo}=12$ ML (b)$t_{Mo}=8$ ML (c)$t_{Mo}=3$ ML.
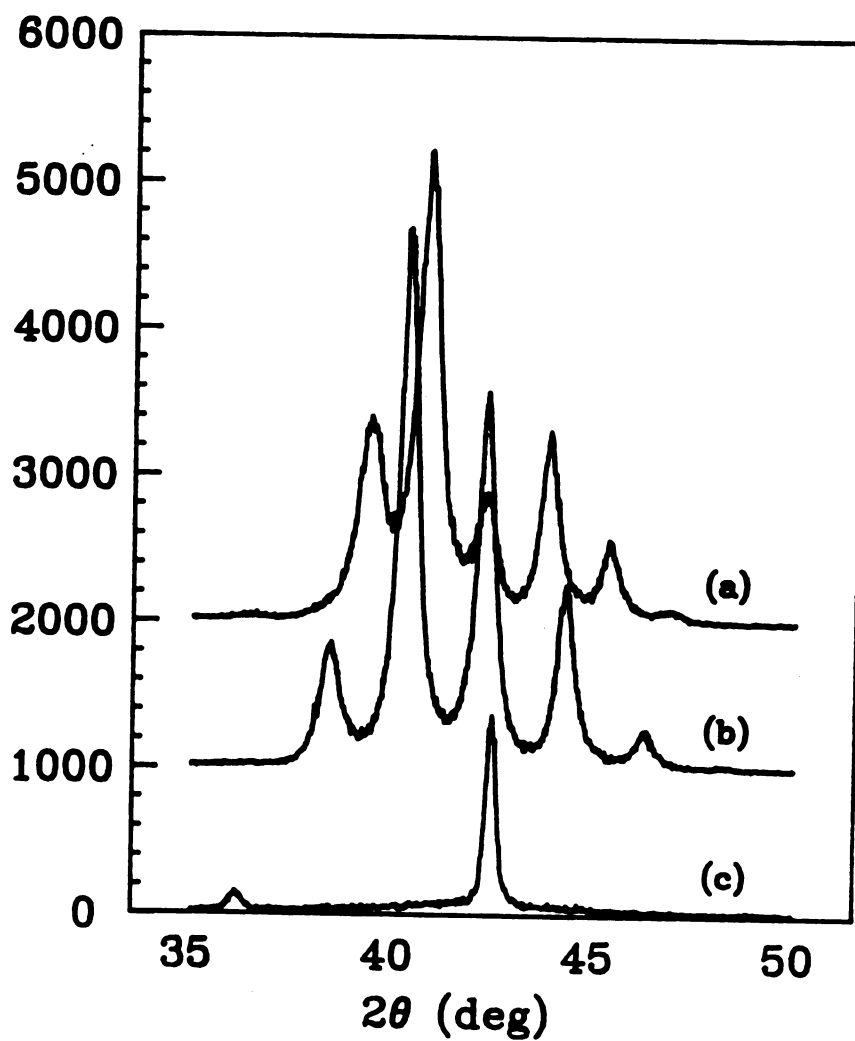
Figure 3.20: High angle reflection lines of samples having equally thick of Fe and Mo layers.
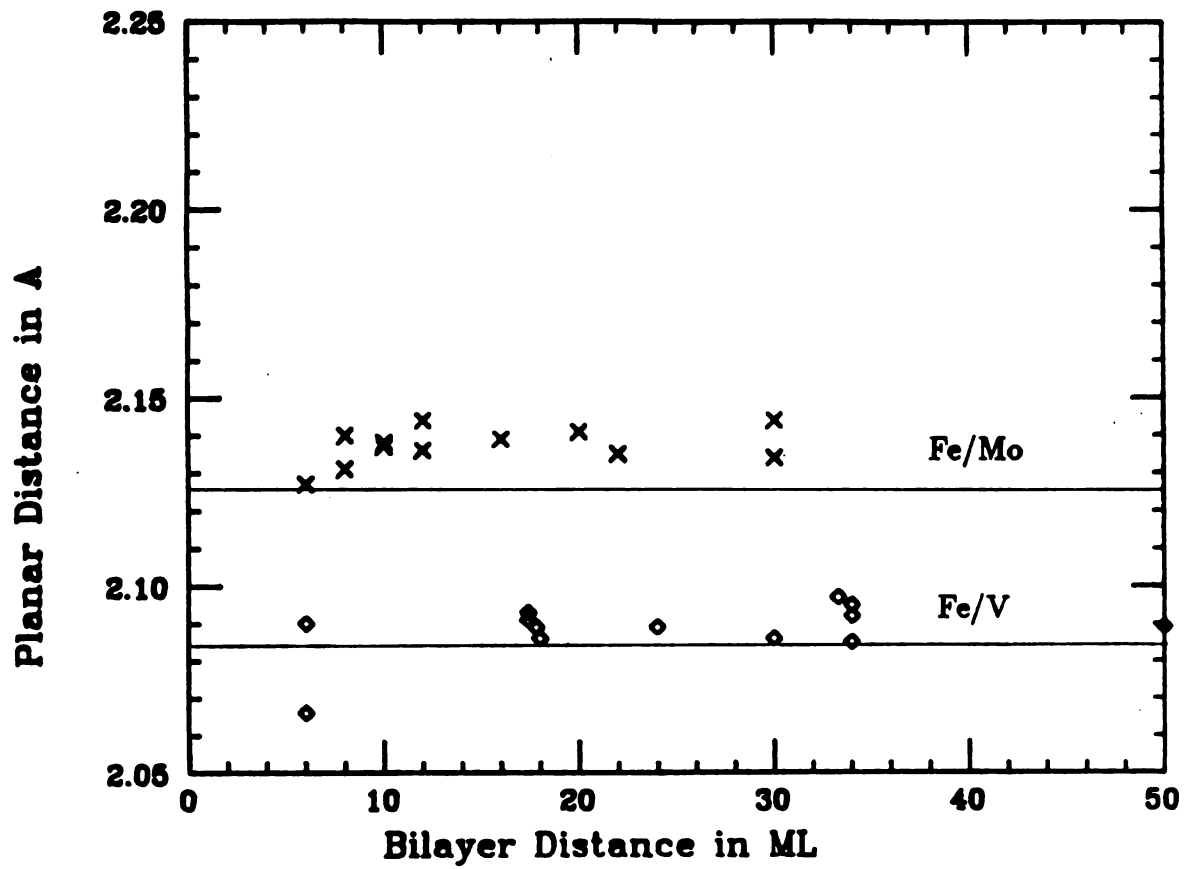
Figure 3.21: Measured d-spacings from the average Bragg lines of each multilayer. The horizontal lines near each data set denote the average d-spacings using the bulk values of d(110) for each metal.

to simulate the structure of the substrate up to a few monolayers. [9] In a multilayer which consists of many number of ultrathin layers, the strain is expected to reside throughout the whole sample making a SLS (Strained Layered Superlattice).

It is easily shown that the average lattice spacings of superlattices can be expressed as a linear function of the chemical composition.

$$d_{AVG} = \Delta x + d_A \qquad (3.25)$$

where

$$x = \frac{N_B}{N_A + N_B} \qquad (3.26)$$

is the fraction of material A in a unit bilayer and

$$\Delta = d_B - d_A \qquad (3.27)$$

is the difference of the two lattice spacings. In standard reflection XRD the average lattice spacing d_{AVG} satisfies the Bragg condition $d_{AVG} \sin \theta_{AVG} = \lambda$. In fig.3.22 the average lattice spacings of Fe/V samples are plotted versus x, the fraction of Fe in a bilayer. The results for both types of sample; i.e. samples with equal layer thicknesses of Fe and V (x~ 0.5), and samples with 3 ML Fe and varying V layer thicknesses, were used in plotting fig.3.22. Data points from the literature[10] are also included. The continuous straight line is the plot of eq.3.25 using the bulk lattice spacings of Fe and V and the individual data points are measured values. Two differences between the data points and the solid line can be pointed out. (i) apparently, there are two regions for the data points; the linearly changing region below $x = 0.4$ and the cluster of data points above the solid line near $x = 0.5$. (ii)the slope from the linear region of data points is larger than the slope of the solid line by about 30%. According to eq.3.25 the slope of the line is just the difference of the two lattice spacings Δ. If a coherency strain really exists, one would anticipate a contracted V lattice and an expanded Fe lattice for the in-plane direction of a strained layered Fe/V superlattice. This contraction and expansion would be a maximum for a common in-plane lattice. Indeed we will see the TED data provide direct evidence of a common in-plane lattice. But the 30% difference in slopes from

fig.3.22 suggest the opposite sense of changes in the growth direction, i.e. a larger V lattice spacing becoming larger and a smaller Fe lattice spacing becoming smaller.

The preceding uniaxial strain is consistent with a very familiar phenomenon in metallurgy and is related to the Poisson's ratio. Consider a cubic object with a lateral length a as in fig. 3.23. If this object is expanded in z-direction by strain ϵ ($\epsilon \ll 1$), then the initial and the final volume can be written

$$V_i = a^3 \tag{3.28}$$

$$V_f = a^3(1 + \epsilon)(1 - \sigma\epsilon)^2 \tag{3.29}$$

If the parameter $\sigma = 1/2$ the volume is not changed to the order of ϵ^2.

$$V_f = V_i + O(\epsilon^2) \tag{3.30}$$

Indeed the observed σ of rubber which is very flexible is 1/2. This parameter σ is called the Poisson's ratio and is defined by

$$u_{ss} = -\sigma u_{zz} \tag{3.31}$$

where u_{zz} is the displacement in the strained direction and u_{ss} is the displacement of the other two direction. A typical value of σ for metals is 1/3.

Since two individual lattice planes with different lattice parameters contact each other in a SLS, the coherency strain apparently lies in the x-y plane in contrast to the definition of the conventional Poisson's ratio where the strain is produced in the z-direction by tension or compression. Consider the cubic object again and assume a strain ϵ in x-direction and y-direction, planar strain, then the final volume is

$$V_f = a^3(1 + \epsilon)^2(1 - \mu\epsilon) \tag{3.32}$$

The ratio of the strain in the z-direction to the strain in plane is newly defined as μ to distinguish it from σ. With $\mu = 2$, $V_f = V_i + O(\epsilon^2)$ so that

$$\mu = 4\sigma \tag{3.33}$$

The in-plane strain in the Fe and V layers of a Fe/V SLS may have the relation

$$E_{Fe}t_{Fe}\epsilon_{Fe} = -E_V t_V \epsilon_V \tag{3.34}$$
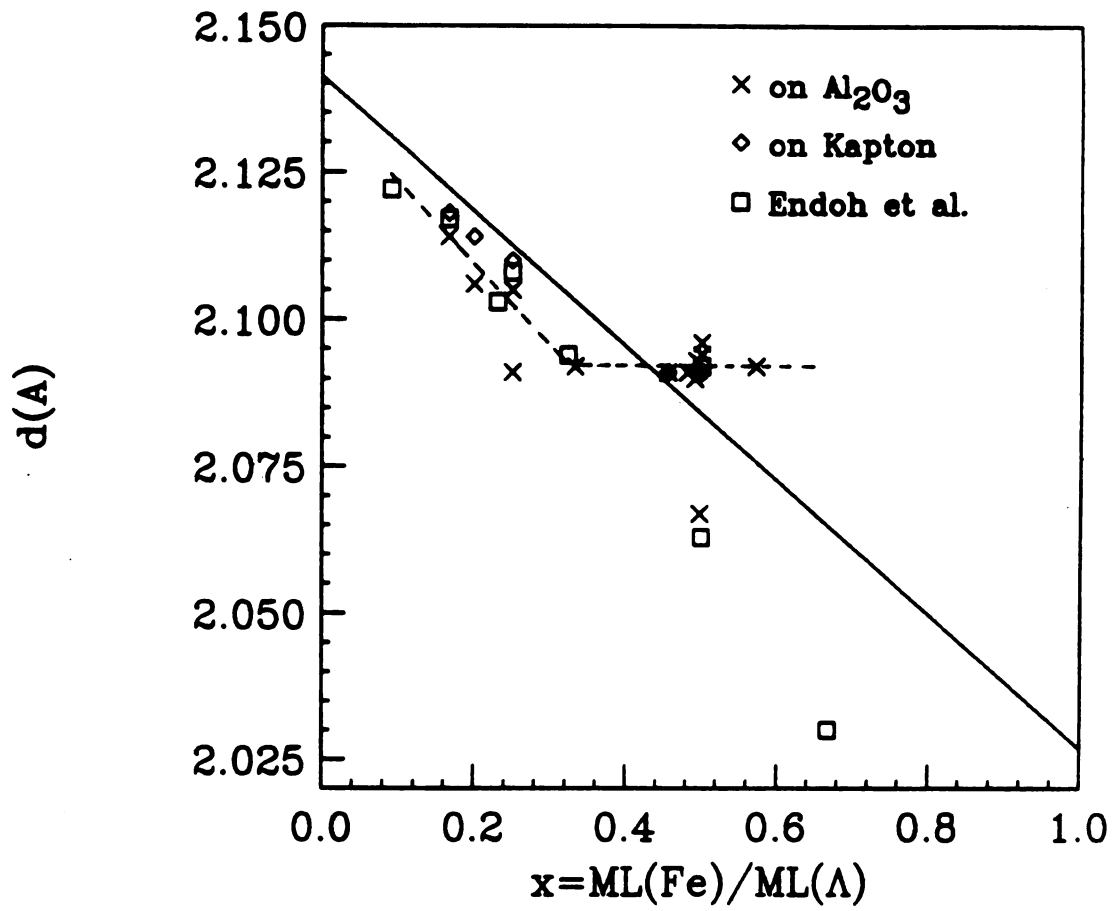
Figure 3.22: The linear relation of the average d-spacing, d, and the fraction of Fe in a bilayer for Fe/V systems.
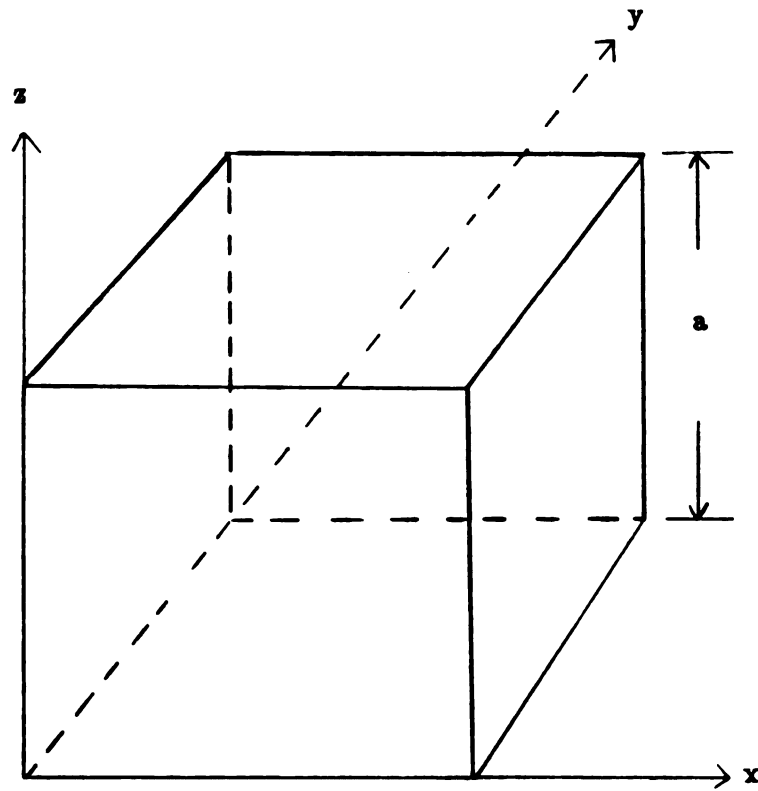
Figure 3.23: A cubic object.

where E's are the Young's moduli, t's are the layer thicknesses and ϵ's are the strains
of each metal. Since the lattice mismatch of Fe and V is 5.34% we have

$$\epsilon_{Fe} - \epsilon_V = 5.34\% \tag{3.35}$$

From eq.3.34 and eq.3.35 and assuming $t_{Fe} = t_V$ we get

$$
\begin{aligned}
\epsilon_{Fe} &= \frac{E_V t_V}{E_V t_V + E_{Fe} t_{Fe}} \times 5.34\% = 2.0\% \\
\epsilon_V &= -3.34\%
\end{aligned}
$$

Finally the lattice spacings of fully strained layers are

$$
\begin{aligned}
d_{Fe}^S &= d_{Fe}^{bulk}(1 - 4\sigma_{Fe}|\epsilon_{Fe}|) \\
d_V^S &= d_V^{bulk}(1 + 4\sigma_V|\epsilon_V|)
\end{aligned}
\tag{3.36}
$$

and the average spacing of the SLS is

$$d_{AVG}^S = d_{AVG}^{bulk} + 2(d_V^{bulk}\sigma|\epsilon_V| - d_{Fe}^{bulk}\sigma_{Fe}|\epsilon_{Fe}|) \tag{3.37}$$

The amount of increase in the spacing estimated using known values of d,σ and ϵ is
$0.028\text{\AA}$. And this explains a little larger observed spacings than the bulk values at
$x = 0.5$ in fig.3.22.

With this uniaxial strain in mind let us examine the experimental high angle
XRD data for effects related to the strain in individual layers. As we saw in section 3
(fig.3.5), the intensities of high angle reflection lines are very sensitive to the relative
difference of two lattice spacings. When the difference is large the intensity of the
average line (I_0) decreases rapidly while the intensities of nearby satellites increase.
Reflection X-ray intensities are calculated using the step model for a system (12
ML Fe/12 ML V)20 with three different lattice parameter conditions: (i)with bulk
lattice spacings (ii) with lattice spacings of uniaxial strain (eq.3.36) (iii) with lattice
spacings of symmetric strain where the sign of strain is the same in any direction. In
fig.3.24 the structure factor squared and the Laue function of the three calculations
are shown: the convolution of these functions produces stronger satellites in the
uniaxial strain model and a diminishing of satellites in the symmetric strain model.

In fig.3.25 the ratios I_0/I_+ (I_0 is the intensity of the average line and I_+ is the intensity of the satellite at higher angle) are plotted for both Fe/V and Fe/Mo systems. In both plots the experimental data points deviate from the bulk model toward the uniaxial strain model. The strains in Fe/V and Fe/Mo SLS are uniaxial but the values are smaller than the values predicted by eq.3.25. The data points for the Fe/Mo system abruptly join the bulk step model for a modulation period of about $\Lambda = 16ML$ while the data points of the Fe/V system do not join up to $\Lambda = 32ML$ which is plausible if we consider the lattice mismatches in these two systems.

Direct evidence of SLS are provided by TED. Fig.3.26 is the TED data for a Fe/V superlattice having Λ =15 ML and illustrates a large number of Bragg lines. These Bragg lines are identified as those of a single BCC lattice. A number of samples with equal numbers of monolayers of Fe and V and systematically varying Λ were prepared. Fig. 3.27(a) is the TED data for a Λ =60 ML sample and fig. 3.27(b) is for a Λ =12 ML sample. The first two rings in fig.3.27(a), < 110 > and < 200 > lines, are wider than the counterparts of fig.3.27(b) but resolution into two rings is not possible. But the third ring in fig.3.27(a), < 211 > line, is clearly a doublet. Numerous higher index lines for this sample are also doublets. These doublets are consistent with two BCC lattices, one for Fe and the other for V is an obvious interpretation. Systematic TED data show that the onset of the single BCC lattice plane for Fe/V occurs when the modulation period is 32 ML or less.

Fig.3.28 shows the TED data of two Fe/Mo samples with equal number of monolayers of Fe and Mo. Fig.3.28(a) is TED data for a Λ =30 ML sample and the first ring is clearly a doublet. A careful inspection of the positions of the rings indicates they are are from two BCC lattices. TED data of Fe/Mo samples of Λ =60 ML and 20 ML also show double BCC lattices while a sample of Λ =12 ML has a single BCC lattice plane. Fig.3.28(b) shows the TED data of a Λ =12 ML sample and the ring pattern is consistent with a single BCC lattice. From this fact it can be claimed that the onset of the single BCC lattice in Fe/Mo system occurs when Λ is between 20 ML and 12 ML. This claim is consistent with the suggested onset at
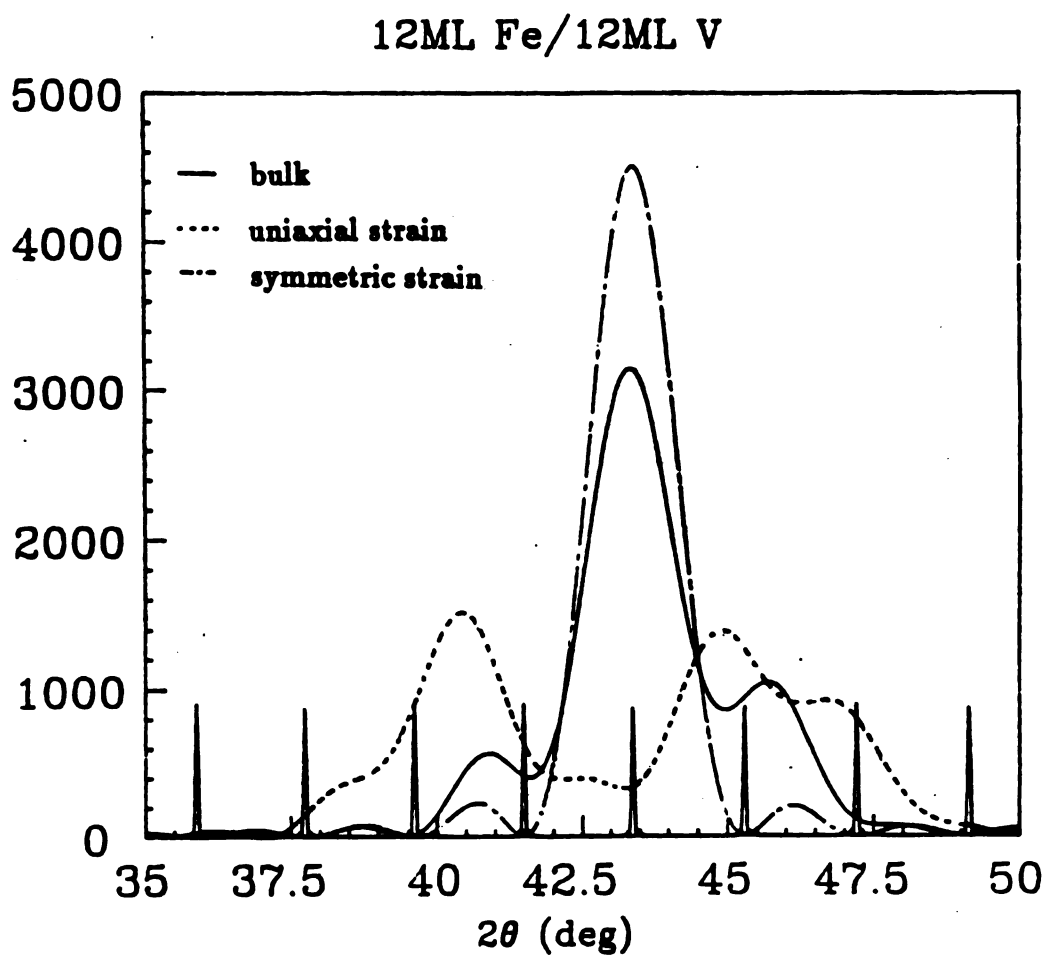
Figure 3.24: The structure factor squared and the Laue functions of three step models.
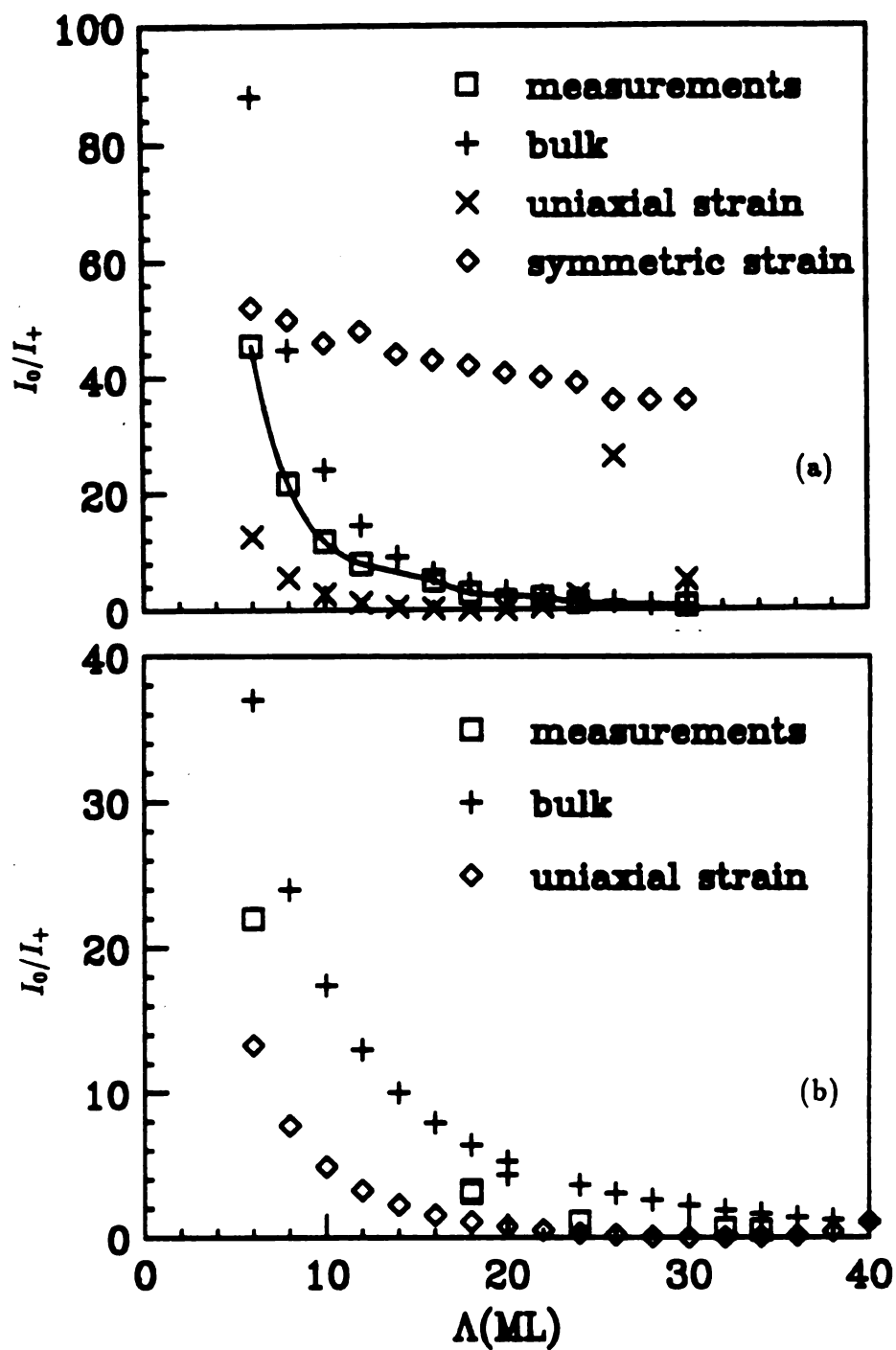
Figure 3.25: The ratios I_0/I_+ of three step models versus Λ. (a)Fe/Mo system (b) Fe/V system.

$\Lambda =16$ ML by the XRD data in fig.3.25(a).

Since the wavelength of the electrons used in TED is small($0.037\mathring{A}$ with 100 Kev) and therefore the Bragg angles are also small(within few tens of mrad), the relative difference of the lattice parameters of the two BCC lattices can be estimated by using the large number of the diffraction ring radii from the TED data. Fig.3.29 depicts the lattice parameter differences of the double BCC lattice planes, Δa, normalized by the larger lattice parameter a_0 as a function of modulation period Λ. A smooth transition from double lattice to single lattice is evident for Fe/V samples while a rather abrupt transition occur between $\Lambda =20$ ML and 12 ML for Fe/Mo samples. As previously noted, this behavior is consistent with the results of the XRD data in fig.3.25.
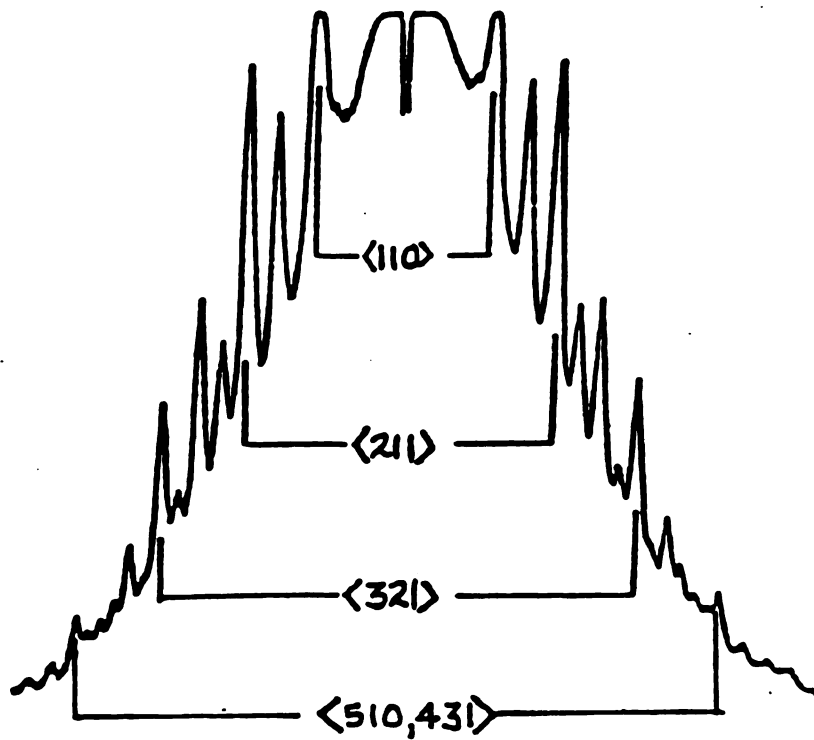
Figure 3.26: The TED data for a Λ =15 ML Fe/V sample. The Bragg peaks are identified as those of a single BCC lattice.
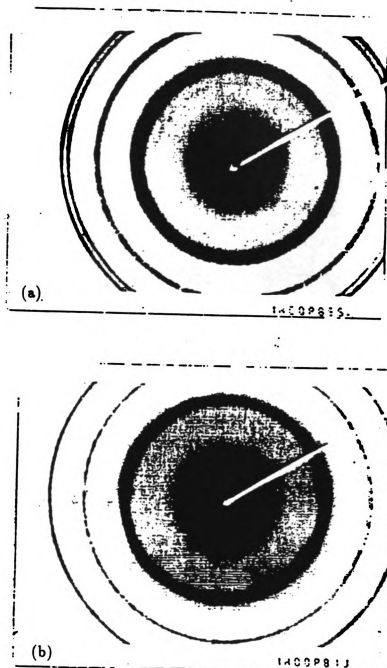
Figure 3.27: The TED data for two Fe/V samples having different Λ's (a) for Λ =60 ML (b)for Λ =12 ML.
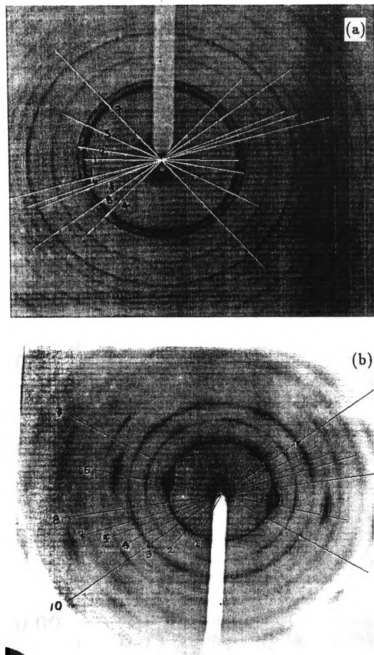
Figure 3.28: The TED data for Fe/Mo samples having different Λ's (a) for $\Lambda = 30$ ML (b)for $\Lambda = 12$ ML.
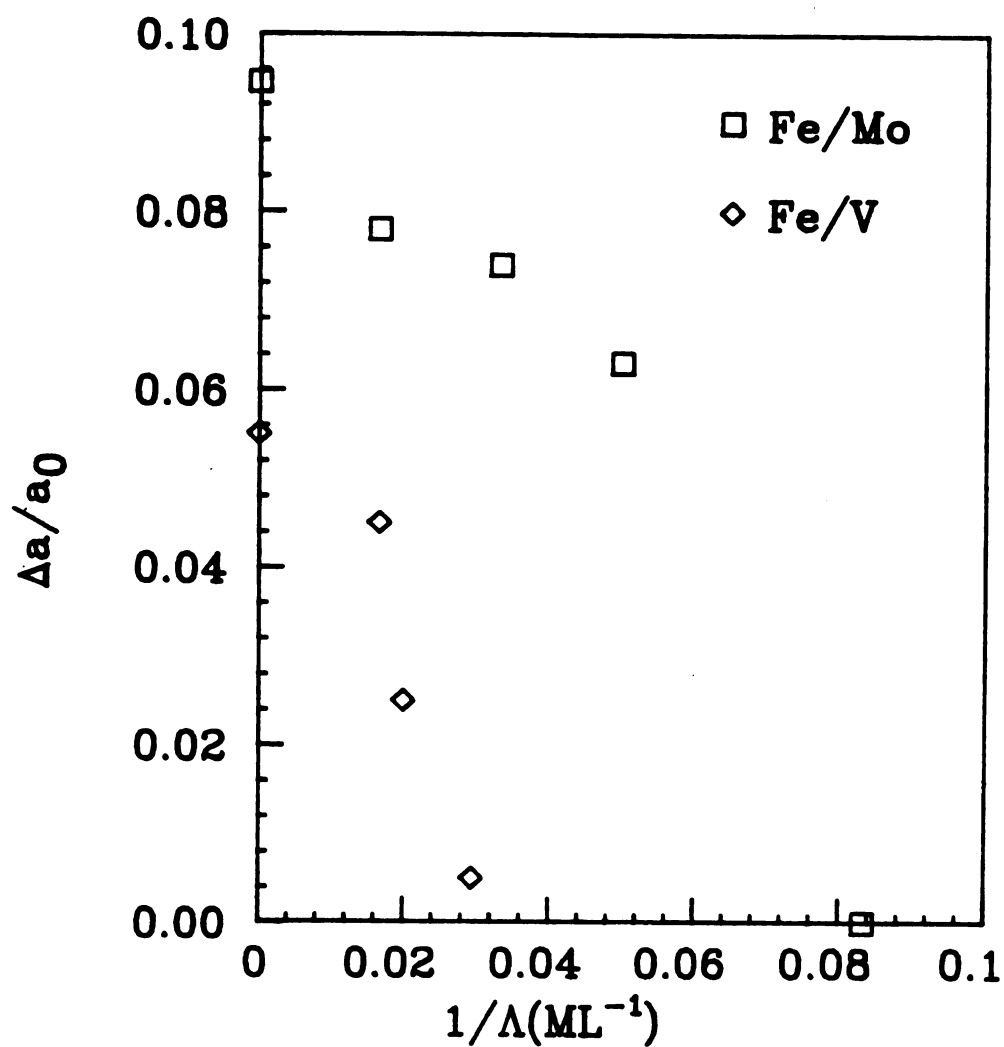
Figure 3.29: The relative differences of the two lattices parameters versus $1/\Lambda$ in Fe/V and Fe/Mo samples using TED data.

Bibliography

[1] B. D. Cullity Elements of X-ray Diffraction, Addison-Wesley Publishing Reading, MA (1956)

[2] W. Sevenhans, M. Gijs, Y Bruynseraede, H. Homma and Ivan K. Schuller, Phys. Rev. B. 34, 5955 (1986)

[3] B. M. Clemens and J. G. Gay, Phys. Rev. B. 35, 9337 (1987)

[4] J.-P. Locquet,D. Neerinck, L. Stockmann, Y. Bruynseraede and Ivan K. Schuller, Phys. Rev. B. 38, 3572 (1988)

[5] J.-P. Locquet,D. Neerinck, L. Stockmann, Y. Bruynseraede and Ivan K. Schuller, Phys. Rev. B. 39, 13338 (1989)

[6] The CRC Handbook of Chemistry and Physics, 66th ed. 1985

[7] A. Segmuller and M. Murakami in "Thin films from Free atoms and Particles" ed. K. J. Klabunde, Academic Press NY (1985)

[8] C. L. Foiles Ultramicroscopy, 29, 80 (1989)

[9] U. Gradmann and G. Waller Surface Science 116, 539 (1982)

[10] Y. Endoh, K. Kawaguchi, N. Hosoito, T. Shinjo, T. Takada, Y. Fujii and T. Ohnish,J. of Phys. Soc. Japan, 53, 3481 (1984)

Chapter 4

Magnetic properties

4.1   Measurements of magnetic data

The magnetization of the samples was measured at 5K on a Quantum Design MPMS magnetometer having a maximum field of 55 KOe. Samples remained on their substrates and were mounted in a plastic tube in a manner that aligned the field parallel or perpendicular to the layers. Fig.4.1 shows a magnetization curve of one of our Fe/V samples. The magnetization in parallel fields rises rapidly at low fields and saturates at about 4 KOe; in perpendicular fields the magnetization increases linearly and saturates at a field about 18 KOe eventually joining the parallel curve. The negative linear slope at high field in both curves is due to the diamagnetic sapphire substrate, the plastic tube and the spacer for sample mounting. Extrapolation of the of the linear portion of this plot to zero field gives the saturation magnetization M_S. The volume of Fe in the layered sample, determined by sample area, individual layer thickness and the total number of layers, was used to obtain an absolute value for M_S. Tests with pure Fe films provided a separate absolute calibration and established our error limits as 5%, most of which is from the errors in sample area measurements and Fe layer thickness measurements.
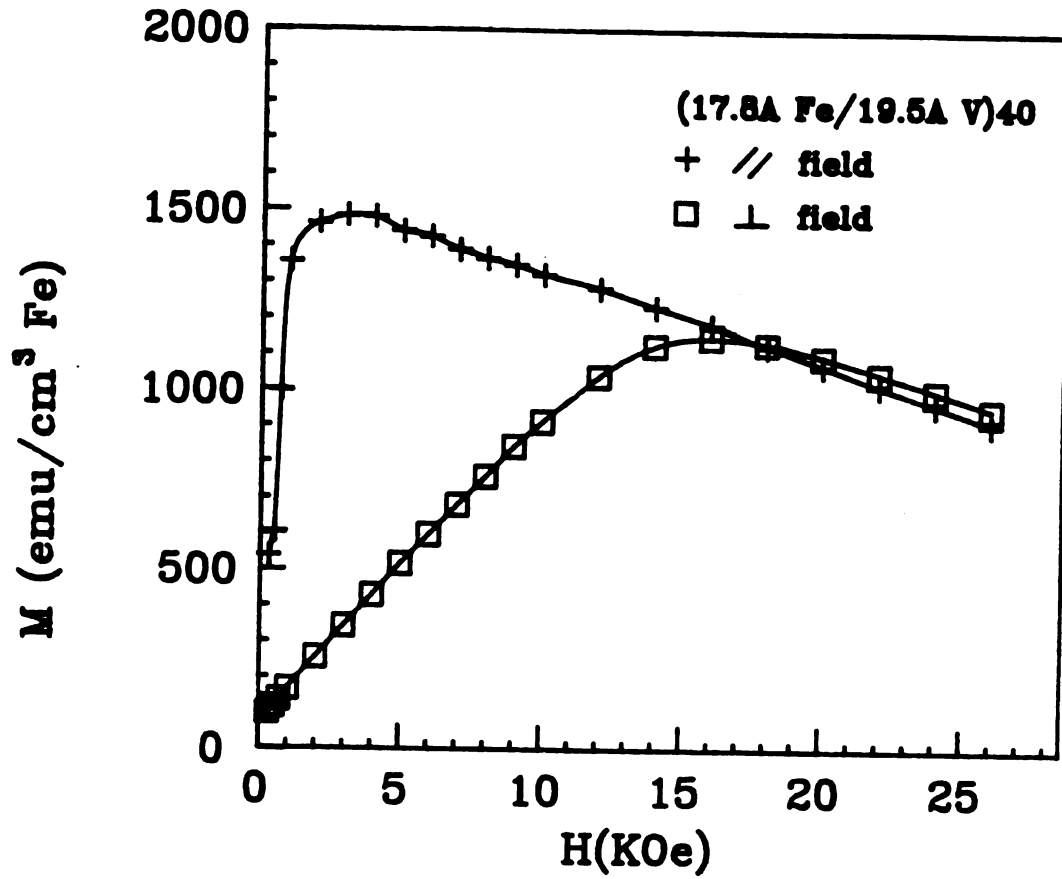
Figure 4.1: The magnetization curves in parallel and perpendicular magnetic fields for a Fe/V multilayer. Extrapolating the high field part to zero field gives the value of $M_S = 1600 emu/cm^3$ at 5K for Fe.
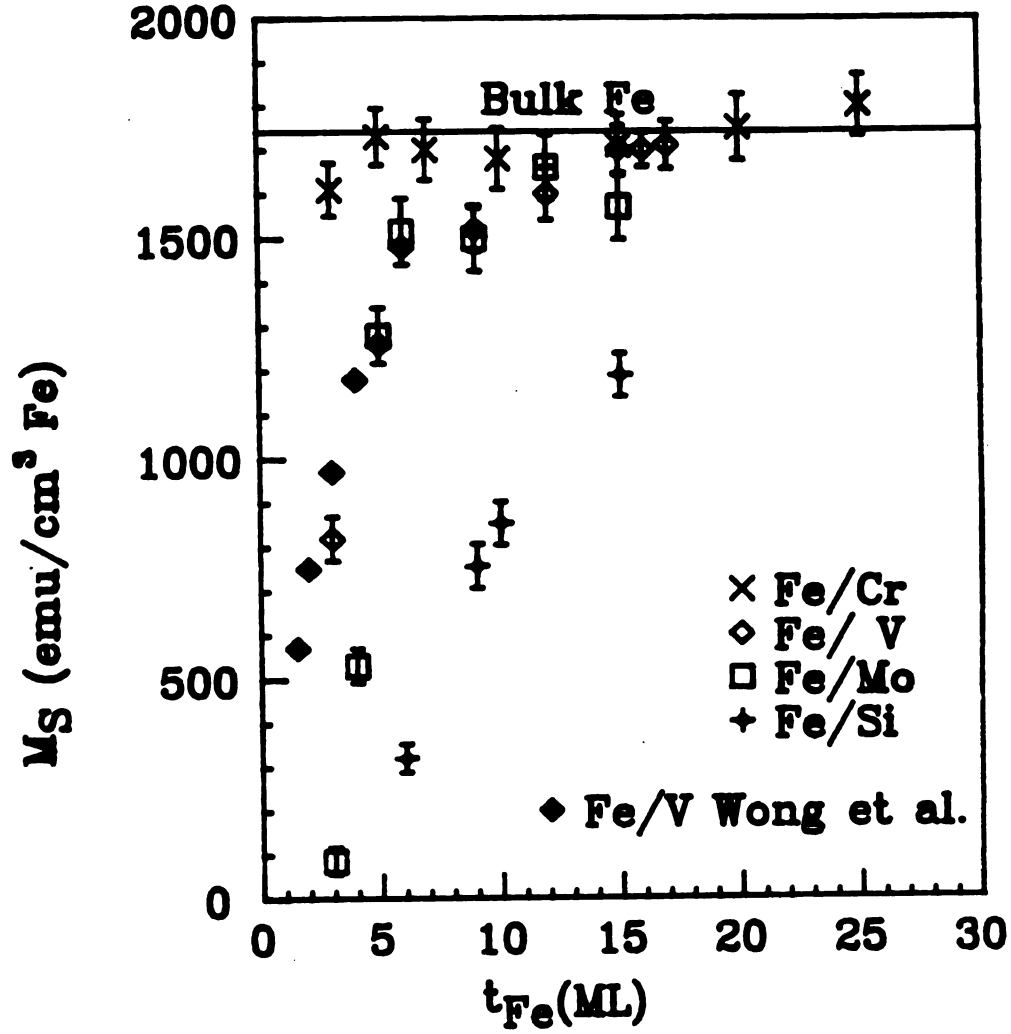
Figure 4.2: The saturation magnetizations for various Fe multilayers as a function of Fe thickness at 5 K. As the Fe layer thickness increases, the value of bulk Fe, 1740 emu/cm^3, is approached.

4.2 Saturation magnetization of Fe multilayers

Fig.4.2 summarizes the saturation magnetizations at a temperature of 5 K for our Fe multilayers (Fe/Si, Fe/Mo, Fe/V and Fe/Cr systems) as functions of Fe layer thickness The thickness of the two constituents in each system are the same with the exception of Fe/Si multilayers where the Si layer thickness is fixed at $50\AA$.

4.2.1 Fe/Si system

The Fe layers in Fe/Si systems show a rapid reduction of their magnetism and become nonmagnetic at a Fe layer thickness of about 5ML($\sim 10\AA$). Data points for Fe/Si multilayers in this plot can be well fitted by assuming that a region of the Fe layers at the interface is magnetically dead. In chapter 3 we showed that the Fe(110) Bragg line in Fe/Si samples becomes systematically broader and weaker as Fe layer thickness decreases. TED data indicated that the long range order in Fe layers is lost when the thickness is less than about $10\AA$ suggesting crystalline to amorphous transition.

As noted earlier, sputtered Si is amorphous in our Fe/Si systems. And somehow, probably due to the disordered surface structure of the a-Si layers, sputtered Fe atoms may not form their stable BCC structure up to a thickness of about $10\AA$ and after that they may form a BCC structure. Suppose a-Fe in our Fe/Si multilayers is nonmagnetic and let t_{Fe} be the individual Fe layer thickness and x_d be the thickness of the magnetically dead layer in each Fe layer as shown in fig. 4.3 Then we have the following relation

$$MNt_{Fe}A = M_0 N(t_{Fe} - x_d)A \tag{4.1}$$

where M is the magnetization per unit volume for all Fe in the sample, M_0 is the magnetization of crystalline bulk Fe, N is the number of Fe layers in the sample and A is the sample area. Rearranging the above equation we have

$$\frac{M_0 - M}{M_0} = \frac{x_d}{t_{Fe}} \tag{4.2}$$

In fig.4.4 data points for Fe/Si samples are plotted as $(M_0 - M)/M_0$ versus $1/t_{Fe}$.
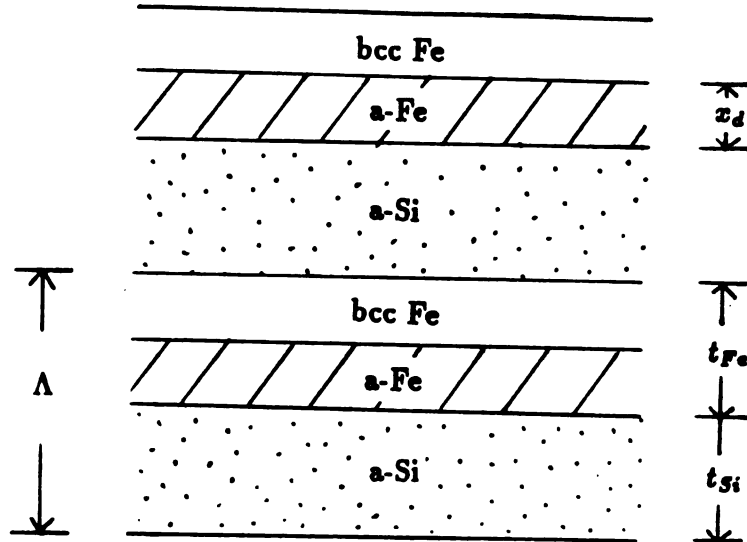
Figure 4.3: Magnetically dead layers in a Fe/Si model system. The Fe layers at the interface with a-Si have a thickness x_d and are assumed to be nonmagnetic.
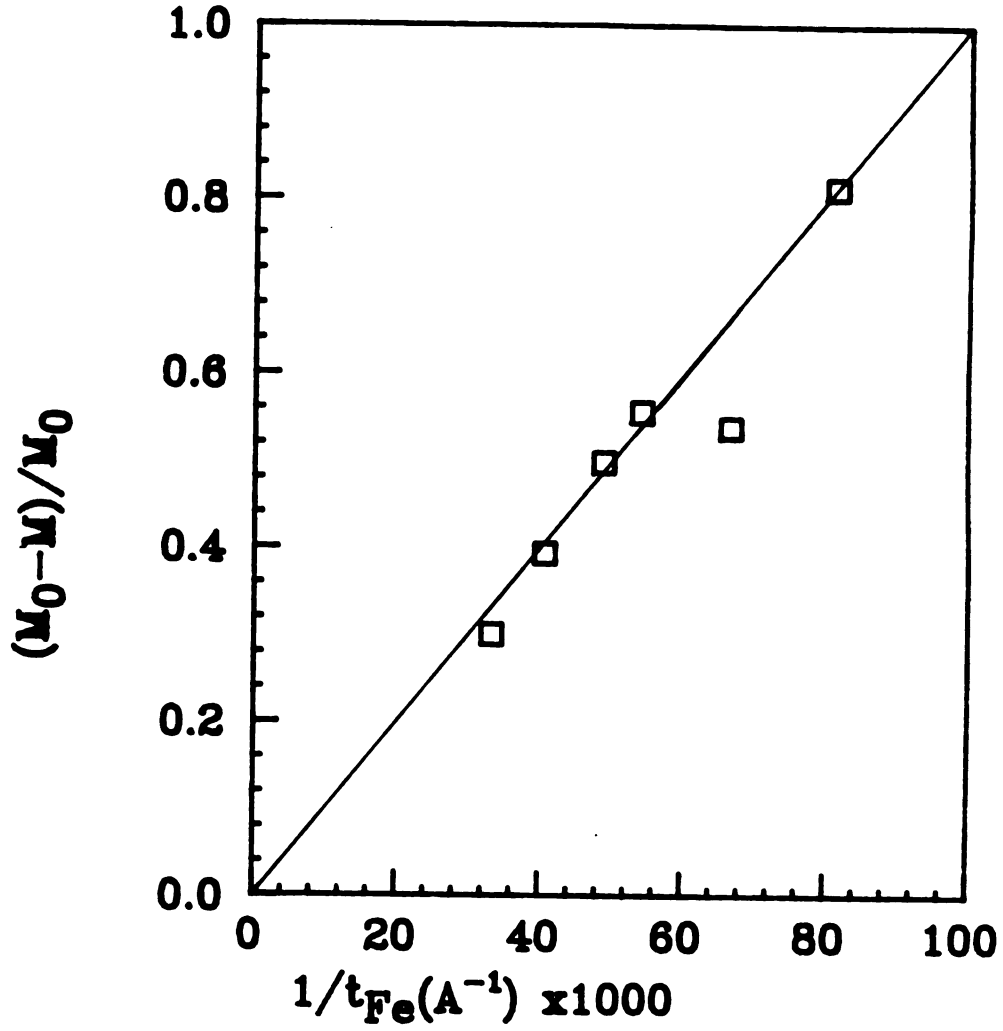
Figure 4.4: Data plot of $(M_0 - M)/M_0$ versus $1/t_{Fe}$ of Fe/Si for multilayers. The slope is the thickness of nonmagnetic Fe layers in the magnetic dead layer model; $x_d = 10.2 \text{Å}$ in this plot.

According to eq.4.2, the slope of this plot is just the thickness of the nonmagnetic Fe region x_d. Linear regression of 6 data points gives $x_d = 10.2\text{Å}$.

In chapter 5 we will describe the EXAFS data which confirm the presence amorphous Fe layers in Fe/Si multilayers as the Fe layer thickness decreases.

4.2.2 Fe/transition metal system

A consideration of the loss (or reduction) in magnetization as Fe layers become thinner with different transition metals produces an interesting pattern. In the Fe/Mo system the Fe layers retain their saturation magnetizations, which is quite close to the value of bulk Fe, until they are about 6 ML thick and then lose the magnetism as the Fe layers become thinner. The sample with nominal parameters 3ML Fe/3ML Mo is nonmagnetic (or at least substantially reduced). The Fe/V system also loses its magnetism as the Fe layer thickness decreases. However the loss occurs at a rather gradual pace and Fe layers with thickness less than 3ML still retain about 50% of the bulk saturation magnetization. The saturation magnetizations of the Fe/Cr system are essentially independent of the Fe thickness down to 3ML Fe.

Surveying the the magnetic behavior in thin Fe multilayers, it seems that the lattice mismatches between Fe and the associated transition metals are systematically related to the reduction of the saturation magnetization. The Fe/Mo system with a 9% mismatch loses magnetism rapidly below 6 ML Fe thickness while the Fe/Cr system with only a 0.6% mismatch does not show a significant reduction in saturation magnetization down to a 3ML Fe thickness.

At this point, however, it is not clear whether the structural disorder in Fe layers caused by lattice mismatch is responsible for the different behaviors in the loss of magnetism or whether the increased number of non-magnetic nearest neighbors due to intermixing plays some role. For the possibility of intermixing at interfaces the phase diagrams of each binary alloys were surveyed. [1][2]

(1) Fe-V

Up to 23 atomic % of V is soluble in Fe at room temperature and BCC structure is retained. The saturation magnetization drops to about half that of bulk Fe at 25 %

V and then drops even more rapidly at higher V concentrations.

(2) Fe-Mo

Only 3 atomic % of Mo is soluble in BCC Fe at $600°C$. The saturation magnetization falls to zero at about 50 % Mo.

(3) Fe-Cr

Up to 20 % of Cr is soluble in BCC Fe at $400°C$. The saturation magnetization drops to half that of bulk Fe at about 30 % Cr.

The effect of interdiffusion at the interfaces would be pronounced when the Fe layers are very thin. Let us look at fig.4.5 where the saturation magnetizations of samples with Fe layers 3ML thick and varying nonmagnetic layer thickness are shown. Again the Fe/Cr system does not show any significant change as the Cr thickness changes. The Fe/V system may have a gradual increase of magnetization as the V layer thickness increases but the magnetizations stays below 70 % that of bulk Fe. The 3ML Fe/t ML Mo system shows the most interesting magnetic behavior. While the 3ML Fe/3ML Mo sample is nonmagnetic, the saturation magnetizations increase rather abruptly as the Mo thickness increases and approach the value of bulk Fe at a 5ML Mo thickness. As noted above Fe and Mo are insoluble. Moreover, if the loss of magnetism is caused by an increased number of Mo nearest atoms due to intermixing, it is difficult to explain the strong magnetism for thicker Mo layer samples. Structural change in the Fe layers caused by lattice mismatch seems to be the most plausible explanation for the loss of magnetism in 3ML Fe/3ML Mo samples. With only 3 atomic layers of each metal and 9% mismatch, it may be more difficult to retain their individual bulk structure than to have some structural disorder. But thick Mo layers would retain the BCC structure to dominate the thinner Fe layers to form an ordered structure. More study is needed to clearly establish a structural change, and EXAFS data in chapter 5 will provide some evidence.

The changes of magnetism in the Fe/V system seem to be explained by intermixing. NMR and Mossbauer measurements indicate a mixed interface range of about 3ML for Fe/V samples.[3] In fig. 4.5 the lower value of saturation magne-
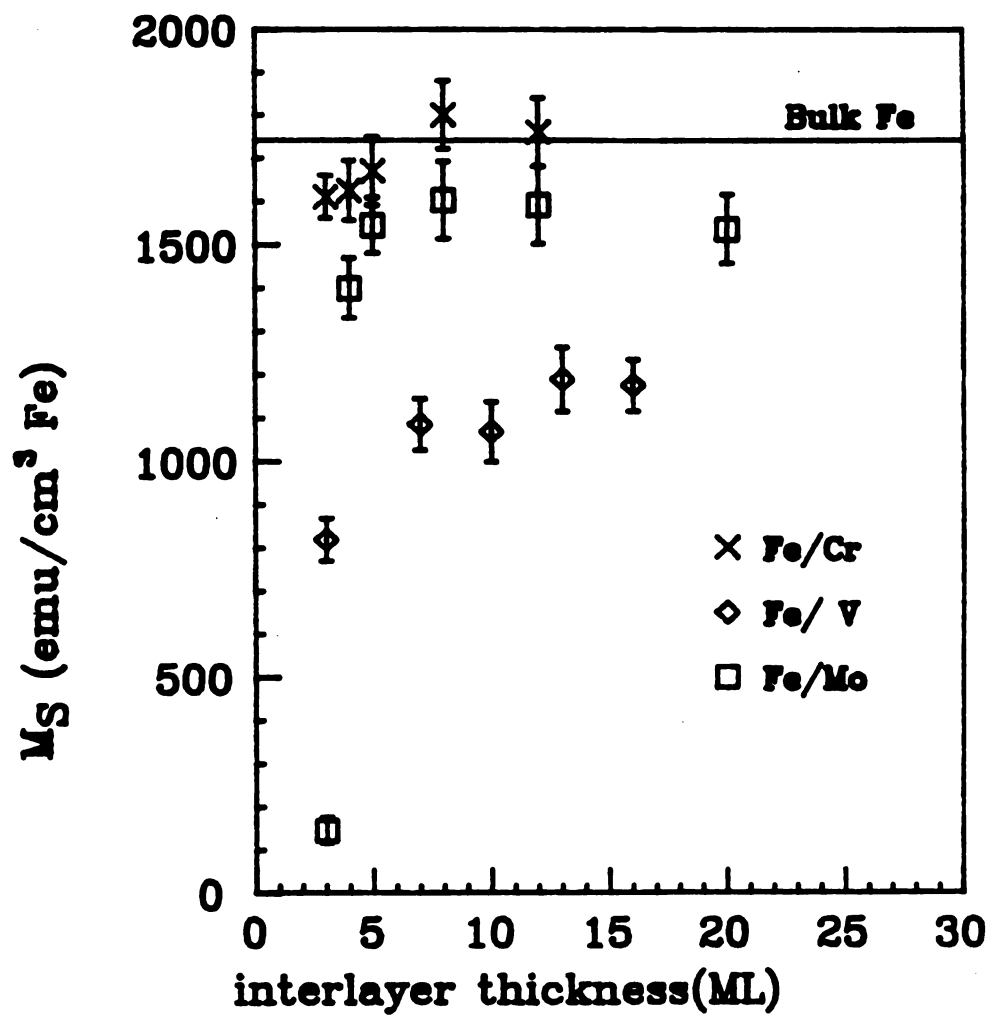
Figure 4.5: Saturation magnetization of 3 ML Fe layer samples as functions of the nonmagnetic layer thickness.
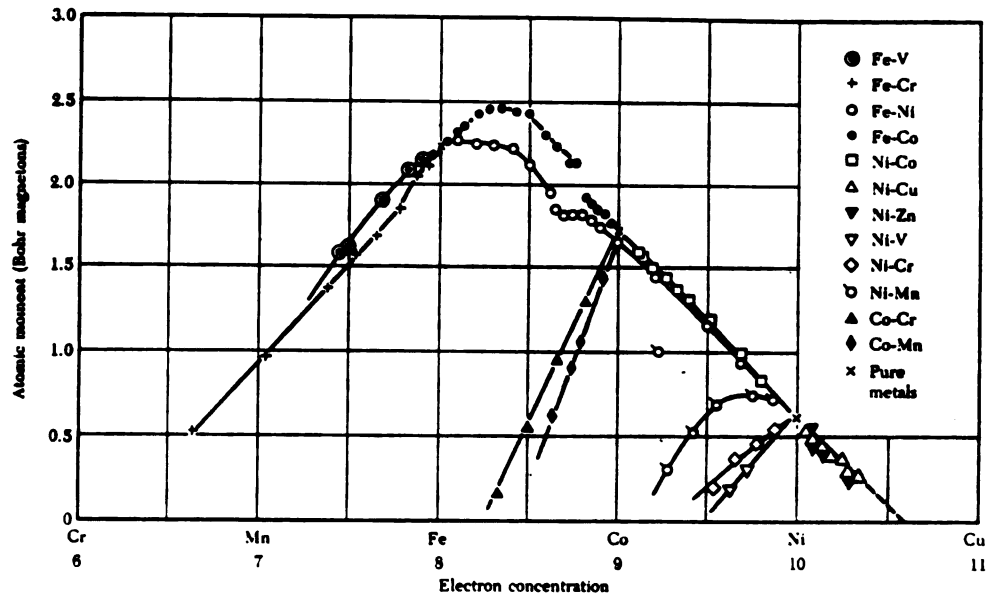
Figure 4.6: Average atomic moments of binary alloys of the elements in the Fe group. (Bozorth.)

tization in 3ML Fe/t ML V systems also suggests intermixing of Fe and V at the interfaces. The Fe layers in Fe/Cr system, on the other hand, retain their bulk magnetization for all samples. No direct data for Fe/Cr interfaces are available but fortunately, the magnetic data of Fe -V and Fe-Cr binary alloys are available in the literature[10] and shown in fig.4.6. The reduction of magnetization for both alloys have almost identical linear dependences on the composition of V or Cr. Combining these facts, the saturation magnetizations of 3 ML Fe layers and the magnetic data of alloys, suggests that the intermixing in Fe/Cr samples is considerably more limited than in Fe/V samples for our sputtered samples. Moreover with almost identical lattice parameters of Fe and Cr, the structural disorder should be much smaller in 3 ML Fe/3 ML Cr samples than in 3 ML Fe/3 ML Mo samples. Less intermixing and structural disorder are consistent with the bulk-like saturation magnetization of 3 ML Fe/3 ML Cr samples.

In summary, structural change caused by insolubility and the large lattice mismatch of Fe and Mo is responsible for the loss of magnetism in the Fe/Mo system. In equal thickness Fe/Mo samples the saturation magnetization drops rapidly when the layer thickness is less than 6ML. At 8ML uniaxially strained layers are observed by XRD and at 6ML the onset of a single lattice is observed by TED. Non-magnetic 3 ML Fe layers in 3 ML Fe/3 ML Mo system recover the magnetism of bulk Fe when the Mo layers become thicker than 5 ML. The Fe layers in Fe/Cr system seem to retain their bulk structure and and there is no evidence for interdiffusion at the interfaces. No loss of magnetism was observed down to a 3 ML Fe layer thickness in Fe/Cr. Both intermixing and some structural change may have occurred in the Fe/V samples.

4.3 Saturation magnetic fields and magnetic interlayer coupling

Numerous magnetic interactions are known in magnetic multilayers. [4] They are

(i) Demagnetizing energy (Shape anisotropy)

(ii) Anisotropy energy

Crystalline anisotropy, Stress anisotropy, Growth anisotropy etc.

(iii) Magnetic field energy with local magnetic field

(iv) Exchange energy between magnetic layers

Recently magnetic interlayer interactions has been reported in some rare earth superlattices[5] and Fe/Cr systems.[6] [7][8][9]

Magnetization curves for parallel and perpendicular fields provide some measure of magnetic anisotropy. Consider a single magnetic thin film. In a thin film there is no interlayer coupling and only various anisotropies could be involved. If the film is very broad compared to the thickness, there is an extra energy per unit volume, $E_D = 2\pi M_S^2$, when the magnetization is oriented normal to the film plane. This is the shape anisotropy and if a magnetic field H is applied perpendicular to the film, $H = 4\pi M_S$ is needed to overcome the demagnetization energy and align the magnetization perpendicular to the film.

In fig.4.1 we have the magnetization curves of a (9ML Fe/9ML V)40 sample in parallel and perpendicular magnetic fields. In parallel fields the magnetization rises quickly at low field and saturates at about 4 KOe. In perpendicular fields, on the other hand, the magnetization shows a slower and linear increase, saturates at about 18 KOe and joins the parallel magnetization curve at higher fields. Extrapolation to zero field gives the saturation magnetization $M_S = 1600 emu/cm^3$ Fe. From now on we designate the parallel saturation field as H_S and the perpendicular saturation field as H_A. If there is only shape anisotropy H_A and M_S should be related by

$$H_A = 4\pi M_S \qquad (4.3)$$

For (9ML Fe/9ML V)40 the observed values of H_A and M_S satisfy eq.4.3 within experimental error suggesting any other anisotropies are very small compared to the shape anisotropy. Indeed the crystalline anisotropy of an Fe single crystal has a very small effect on the saturation field H_S giving only for 0.4KOe difference in H_S between the easy axis (100) and the hard axis (111).[10] All Fe/V and Fe/Mo samples

tested in this thesis give results consistent with eq.4.3. Currently available data for perpendicular measurements of the Fe/V and Fe/Mo systems are summarized in table 4.1 and table 4.2, respectively.

Fe/Cr systems show magnetization curves much different from those of Fe/V or Fe/Mo systems. The magnetization curves for fields parallel and perpendicular to the sample planes of 2 Fe/Cr superlattices are shown in fig.4.7 (a) for 5ML Fe/5ML Cr and (b) for 5ML Fe/20ML Cr. The magnetization of sample 5ML Fe/5ML Cr increases very slowly in both directions saturating at 26KOe in a parallel field and at 38KOe in a perpendicular field; from parallel field data $M_S = 1800 emu/cm^3 Fe$. The saturation fields in both directions are much higher than that of Fe/V and Fe/Mo samples for which $H_S \sim 3KOe$ and $H_A \sim 4\pi M_S$. Sample 5ML Fe/20ML Cr has another interesting feature in its magnetization curve: $H_S = 3KOe$ which is typical in the case of Fe/V or Fe/Mo systems but $H_A = 14KOe$ which is smaller than the demagnetizing field $4\pi M_S = 22.6KOe$ by 8.6KOe ! The saturation field H_S changes systematically with the change of Cr interlayer thickness as shown in fig. 4.8 for 7ML Fe thickness samples. The magnetization of the sample with 3ML Cr layers saturates at $H_S = 19KOe$ and H_S systematically decreases as the Cr layer thickness increases. Near and above 10ML Cr thicknesses, H_S is approximately constant at 6KOe.

Fig.4.9 summarizes the systematic dependence of H_S on the Cr layer thickness in our Fe/Cr superlattices. One immediately notices that the strength of change in H_S also depends on the Fe layer thickness; 3ML Fe samples have a strong change in H_S while samples with thicker Fe layer have a very weak dependence of H_S upon Cr layer thickness.

Ultrathin Fe layers are known to have antiferromagnetic coupling across Cr layers. Recently Grunberg et al. studied evaporated Fe/Cr/Fe sandwich samples using light scattering from spin waves, and claimed antiferromagnetic coupling of magnetic Fe layers across the Cr interlayer.[9] They also found that in a small external field the double Fe layers order antiparallel with their magnetizations perpendicular to the external field in analogy to the spin- flop phase of antiferromagnets.

ID No.	ML Fe/ML V	$H_S(KOe)$	M_S	$4\pi M_S(KOe)$	$H_A(KOe)$
#134-9	17/17	3	1710	21.5	22
#134-3	15/15	3	1700	21.4	22
#134-2	9/9	4	1500	18.8	18
#69-13	3/3	4	900	11.3	12
#151-13	3/9	4	1530	19.2	20

Table 4.1: The magnetic data of Fe/V samples. $H_A = 4\pi M_S$ is well satisfied.

ID No.	ML Fe/ML Mo	$H_S(KOe)$	M_S	$4\pi M_S(KOe)$	$H_A(KOe)$
#199-3	8/8	6	1800	22.6	22
#199-8	3/8	5	1800	22.6	22
#199-9	3/12	4	1700	21.4	18

Table 4.2: The magnetic data of Fe/Mo samples.
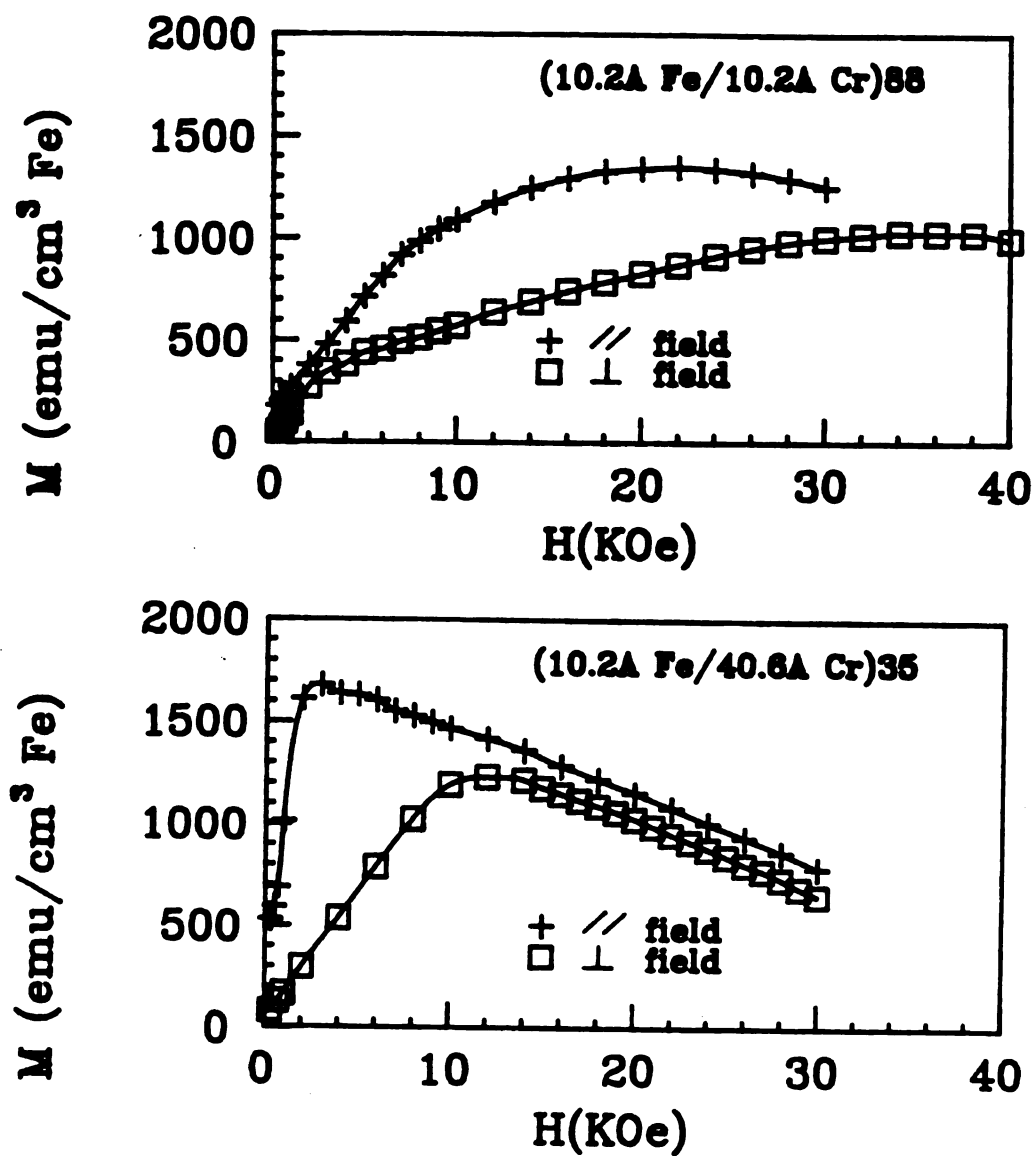
Figure 4.7: The magnetization curves in parallel and perpendicular fields for (a)5ML Fe/5ML Cr and (b) 5ML Fe/20ML Cr superlattices.
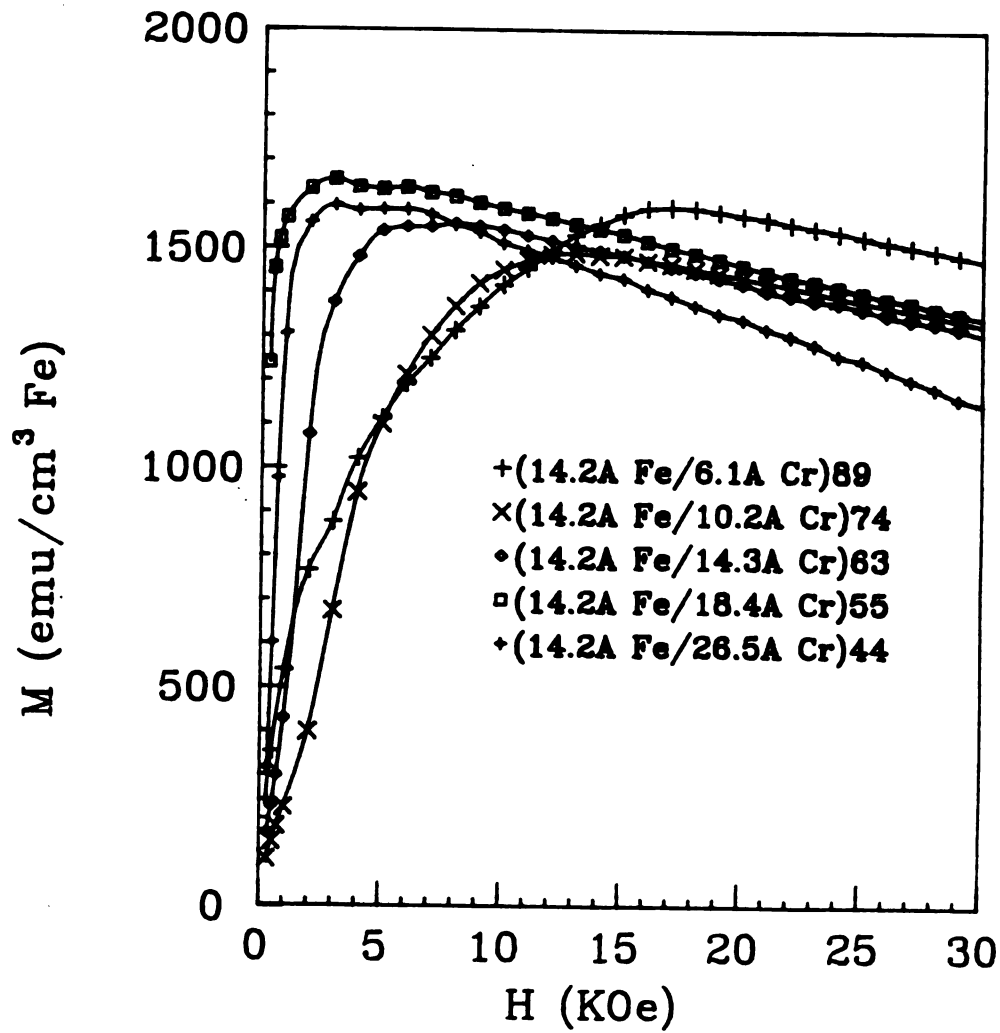
Figure 4.8: The magnetization curves of 7ML Fe/t ML Cr samples in parallel field. The saturation field H_S decreases systematically as the Cr thickness increases.
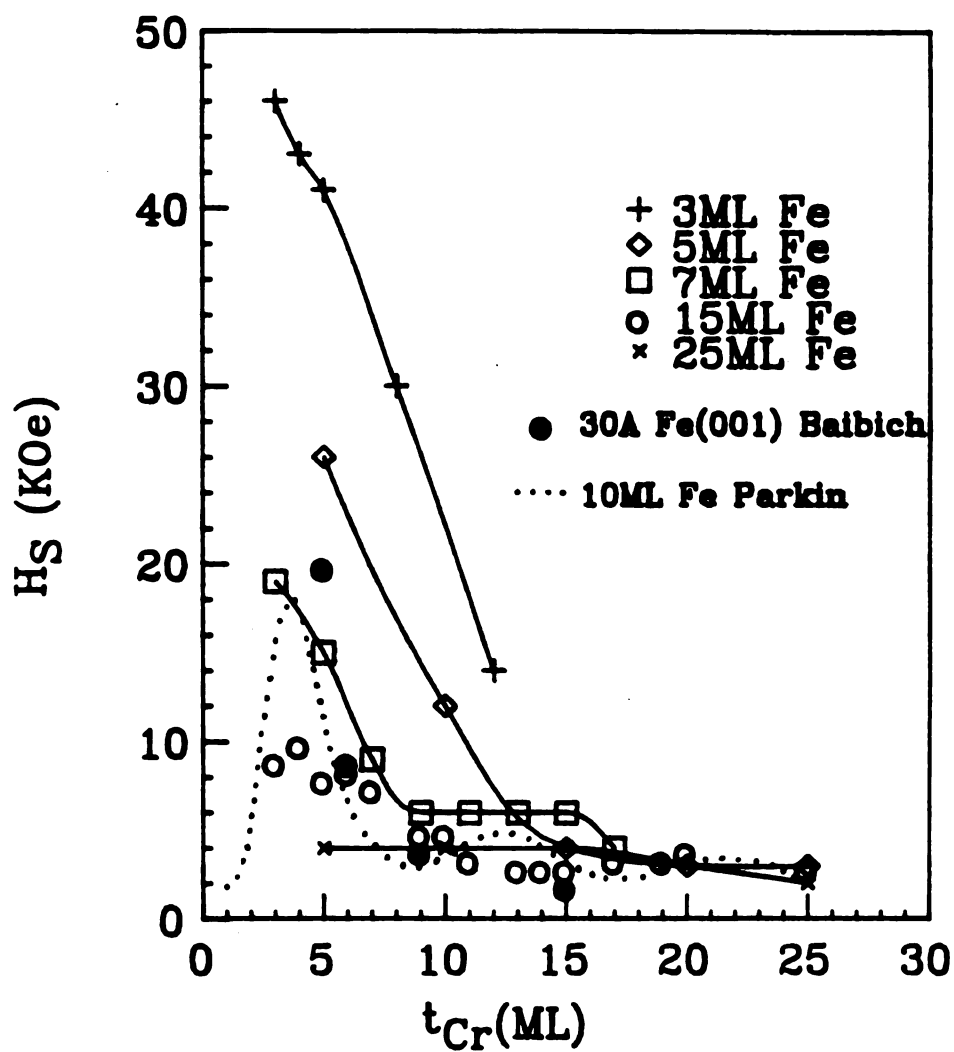
Figure 4.9: The systematic change of saturation field H_S as a function of the Cr thickness. Data for samples with different Fe thickness are plotted separately.

The antiferromagnetic coupling also has been observed in an evaporated $20\mathring{A}$ Fe/$20\mathring{A}$ Cr/$20\mathring{A}$ Fe double layer by Carbone and Alvarado via in-situ spin-polarized LEED.[7] [8] $30\mathring{A}$ (001)Fe/(001)Cr superlattices grown by the MBE method have been studied by Baibich et al.[11] Their saturation fields also have a strong dependence on the Cr layer thickness as depicted in fig.4.9 but the dependence upon the Fe thickness for their and our samples differs. They ascribed the high saturation field of thin Cr thickness sample as a signature of antiferromagnetic interlayer coupling when the Cr layer thickness is below $30\mathring{A}$. Very recently Parkin et al. investigated ($20\mathring{A}$ Fe/t_{Cr})M superlattice samples fabricated in a dc magnetron sputtering system.[6] They measured the saturation field and the magnetoresistance as functions of the Cr layer thickness and observed high saturation fields for thin Cr thicknesses and low saturation fields for thicker Cr layers. However, their saturation fields oscillate as the Cr thickness changes rather than dropping monotonically as shown in fig.4.9. They claimed this oscillatory behavior is evidence of oscillations in the exchange interaction coupling the Fe layers across the Cr layers.

In fig.4.9, the saturation fields of our Fe/Cr samples are plotted for each Fe thickness as functions of the Cr interlayer thickness. The data points of the two other groups are reproduced for comparison. The saturation fields of our Fe/Cr samples with Fe layer thicknesses below 15 ML are very high in the thin Cr thickness region and drop rapidly and monotonically as the Cr layer become thicker. Any oscillations like the data of Parkin's group were not observable in our samples. The behavior of thin Fe layer samples is qualitatively consistent with literature results and suggests antiferromagnetic interlayer coupling in our Fe/Cr superlattices. The strong dependence of H_S on the Cr interlayer thickness become weaker as the Fe layer become thicker and for 25 ML Fe layers H_S is almost constant at about 4 KOe. This value occurred for H_S in the Fe/Mo or Fe/V systems where no interlayer interaction occurred. The Fe layer thickness for the Baibich et al. was 15 ML but their samples were prepared on GaAs(001) substrates and have a BCC(001) Fe/Cr texture.Our sputtered samples have a BCC(110)Fe/Cr texture. Whether the different behaviors in H_S for these 15 ML Fe samples originates from the different texture or the quality

of the samples is not clear at this time. Although samples with 10 ML Fe layers were not available in our study, the fine oscillations observed by Parkin's group are not seen in our data for thicker and thinner layers. While both studies used the sputtering method there are two differences in the sample preparation conditions: First, the deposition rate was 2Å/sec in Parkin's study and 7Å/sec was used in our sample preparations. Second, they used Si(111) substrates while sapphire(0001) was used for our samples. How these conditions affect the sample quality is not clear.

As we pointed out, the difference between the perpendicular saturation magnetic field H_A and the demagnetizing field $4\pi M_S$ is a measure of extra magnetic anisotropy. The data for $\Delta H = H_A - 4\pi M_S$ are plotted in fig.4.10 as functions of the Cr thickness . The dependence of ΔH on the Cr layer thickness is quite similar to that of H_S except a number of negative values occur for ΔH. This similarity and difference raise the following two questions:

(i) Does the extra anisotropy in our Fe/Cr superlattices which is represented by ΔH, originate solely from the antiferromagnetic interlayer coupling?

(ii) If the answer for question (i) is "yes" what does the negative value of ΔH mean?

In an effort to answer question (i), a plot of ΔH vs H_S is provided in fig.4.11. Interestingly enough these two quantities are closely related over the positive range of ΔH indicating the two quantities are closely related by a common physical origin, the antiferromagnetic interlayer coupling. Another interesting fact to be noted is that the negative values of ΔH are always occurred at the lowest values of H_S where antiferromagnetic interlayer coupling is weak or zero. Ferromagnetic interlayer coupling may be associated with these negative values of ΔH.
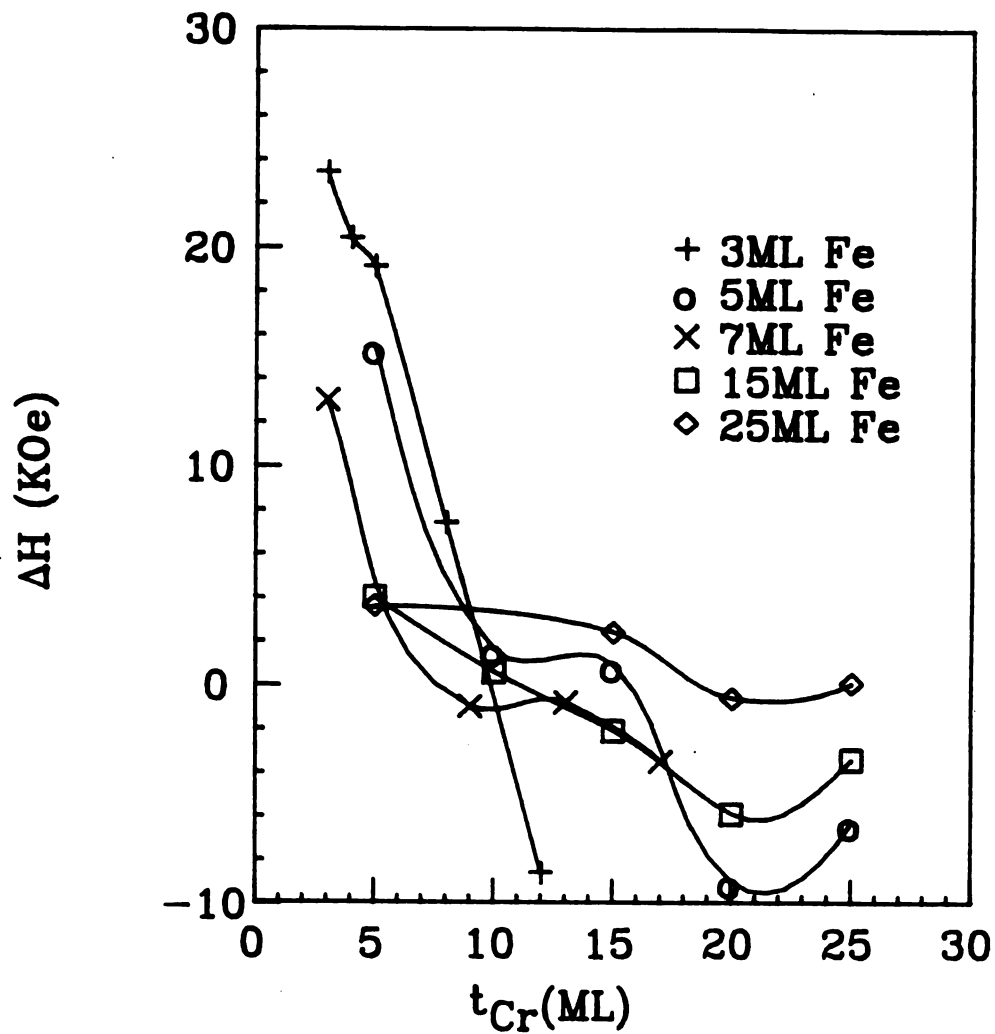
Figure 4.10: Plot of $\Delta H = H_A - 4\pi M_S$ versus the Cr layer thickness.
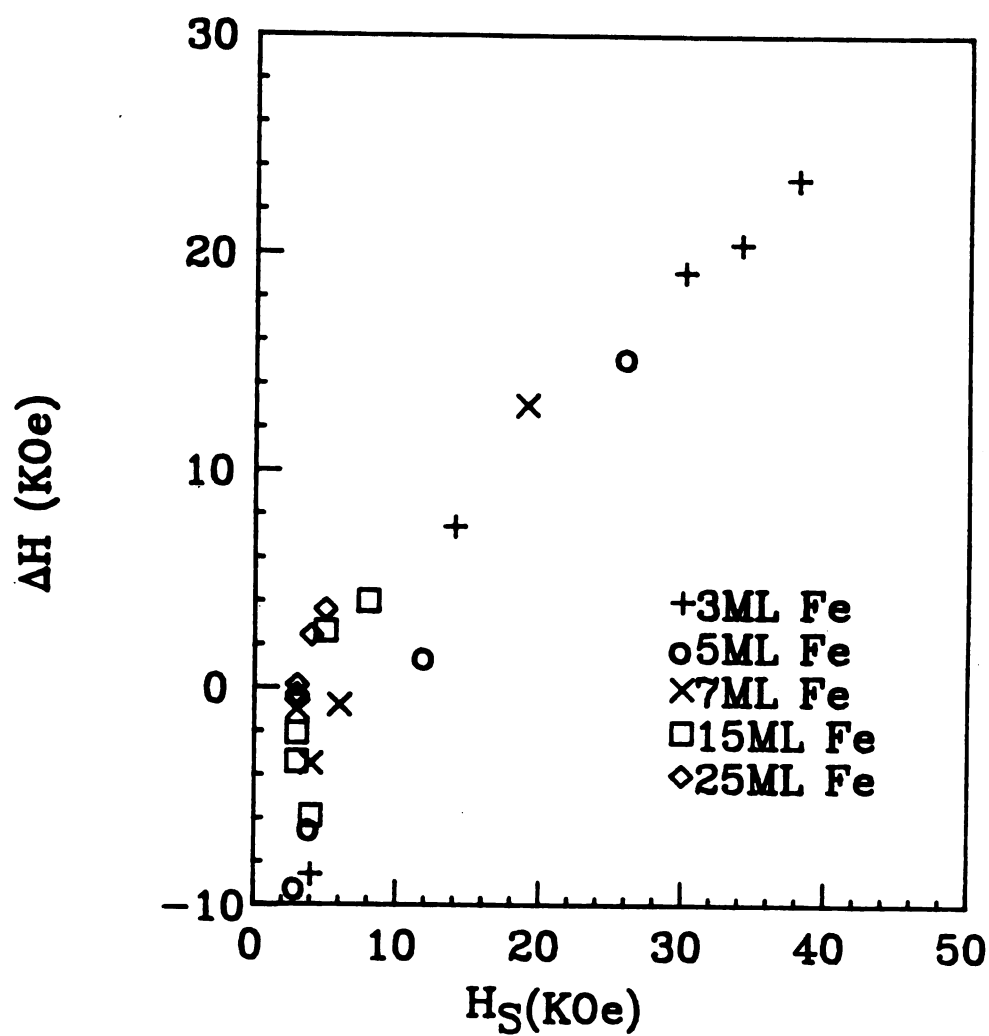
Figure 4.11: Plot of ΔH versus H_S. The high degree of linear correlation between the two parameters is clear for positive values. Note also that negative ΔH is always associated with very low H_S values.

Bibliography

[1] M. Hansen, Constitution of Binary Alloys, 2nd edition Metallurgy and Metal-lurgical Engineering Series (McGraw-Hill Book Company, 1958)

[2] R.M. Bozorth, Ferromagnetism, 2nd edition (D. Van Nostrand Company, 1953)

[3] T. Shinjo and T. Takada, Metallic superlattices (Elsevier Science Publishers B.V., 1987)

[4] A.H. Eschenfelder, Magnetic Bubble Technology (Springer-Verlag Berlin Hei-delberg New york, 1980)

[5] C.F. Majkrzak, J.W. Cable, J. Kwo, M. Hong, D.B. McWhan, Y. Yafet, J.V. Waszczak, and C. Vettier, Phys. Rev. Lett., 56, 2700 (1986)

[6] S.S.P. Parkin, N. More and K.P. Roche, Phys. Rev. Lett., 64, 2304 (1990)

[7] C. Carbone and S.F Alvarado, Phys. Rev. B., 36, 2433 (1987)

[8] S.F. Alvarado and C. Carbone, Physica B, 149 (1987) 43-48

[9] P. Grunberg, R. Schreiber and Y. Pang, Phys. Rev. Lett., 57, 2442 (1986)

[10] C. Kittel, Introduction to Solid State Physics, 6-th edition (John Wiley & Sons Inc. NY, 1986)

[11] M.N. Baibich, J.M. Broto, A. Fert, F. Nguyen Van Dau, F. Petroff, P. Eitenne, A. Friederich, and J. Chazelas, Phys. Rev. Lett., 61, 2472 (1988)

Chapter 5

EXAFS studies

5.1 Introduction

The term extended X-ray absorption fine structure(EXAFS) refers to the oscillations of the X-ray absorption coefficient on the high-energy side of an absorption edge. Such oscillations can extend up to 1000 eV above the edge and may have a magnitude of 10 % or more. As an example, the EXAFS spectrum near the K edge in a polycrystalline Fe foil sputtered onto a ultra high pure Al foil is shown in fig.5.1 This EXAFS signal was taken by detecting the total electron yield which is proportional to the X-ray absorption coefficient. The total electron yield method will be discussed in the next section. Core levels of atoms differ and thus the energy of the absorption edge uniquely identifies the atomic constituent being studied; the technique is element specific. The abrupt jump in the absorption coefficient is the Fe K edge absorption (the binding energy of Fe K-shell is 7112 eV) and the height of this jump is proportional to the amount of Fe in the sample. The oscillations at energies greater than about 30 eV above the edge are EXAFS data and they can be used to determine the local structure surrounding the absorbing atoms.

The oscillatory part of the absorption coefficient $\Delta\mu$, normalized to the structureless(atomlike) background μ_0, is given by[1]

$$\chi(k) = \frac{\Delta\mu}{\mu_0} \quad = \quad -\sum_j \frac{N_j}{kr_j^2} |f_j(k,\pi)|$$
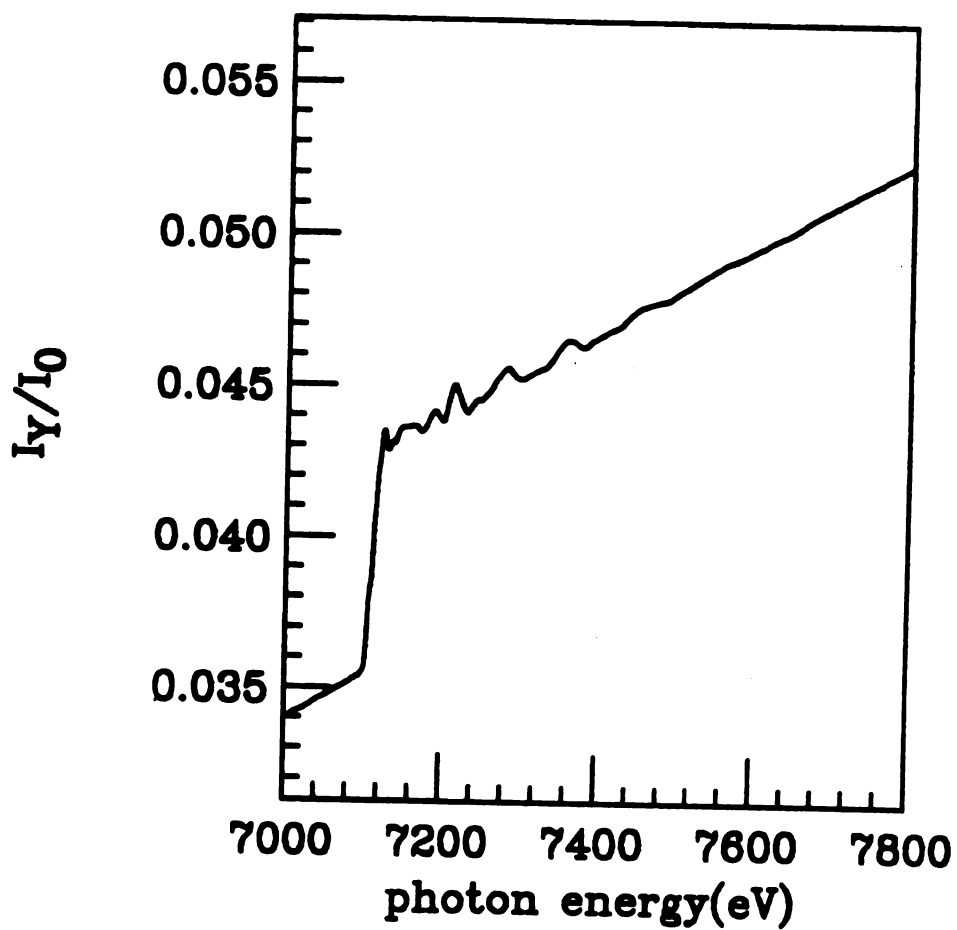
Figure 5.1: Total electron yield spectrum of a polycrystalline Fe foil. The sharp rise in yield near 7112 eV is the Fe K edge and the modulation above the edge is the EXAFS.

$$\times \quad \sin[2kr_j + \psi(k)]e^{-2\sigma j^2 k^2}e^{-2r_j/\lambda_j(k)} \qquad (5.1)$$

Eq.5.1 describes the modification of the photoelectron wave function at the origin due to scattering by N_j neighbors located at a radial distance r_j away. This is illustrated in fig.5.2 where (a) an X-ray photon is absorbed by an atom through the excitation of an electron from a core state j to an unoccupied continuum state f (i.e., $E_f = E_j + \hbar\omega \geq E_{Fermi}$), (b) the photoexcited electron waves propagate outward from the excited atom(nodes denoted by solid lines) and (c) a scattered wave from a neighboring atom interferes with the outgoing wave at the excited atom(nodes denoted by dashed lines), modulating the wave function at the core level and thus the absorption cross section. The backscattering amplitude is given by

$$
\begin{aligned}
f(k,\pi) &= |f(k,\pi)|e^{i\phi(k)} \qquad (5.2)\\
&= \frac{1}{2ik}\sum_l (2l+1)(e^{2i\delta_l} - 1)(-1)^l
\end{aligned}
$$

where $\delta^l(k)$ are the scattering phase shifts. The photoelectron wavevector k is defined as

$$k = [2m_e(\hbar\omega - E_0)]^{1/2}/\hbar \qquad (5.3)$$

where ω is the X-ray frequency and E_0 is the threshold energy. It is clear that the electron wave will be phase shifted by $2kr_j$ by the time it makes the round trip to the neighbor. To this we must add the total phase function $\psi_j(k)$ given by

$$\psi_j(k) = \phi_j(k) + 2\delta_1(k) \qquad (5.4)$$

The first term $\phi_j(k)$ is the phase shift due to the backscattering from the j-th neighboring atom as defined in eq.5.2, while the second term is twice the absorbing atom phase shift $\delta_1(k)$ to account for the potential of the absorbing atom through which the $l = 1$ photoelectron wave(excited from $l = 0$ state) has traversed.

The Debye-Waller-type term $exp(-2\sigma_j^2 k^2)$ accounts for the thermal vibrations of the atoms. Finally, electrons that have suffered inelastic losses will not have the proper wave vector to contribute to the interference process. This is accounted for by a mean free path, $\lambda_j(k)$, in an exponential damping term $exp[-2r_j/\lambda_j(k)]$. This
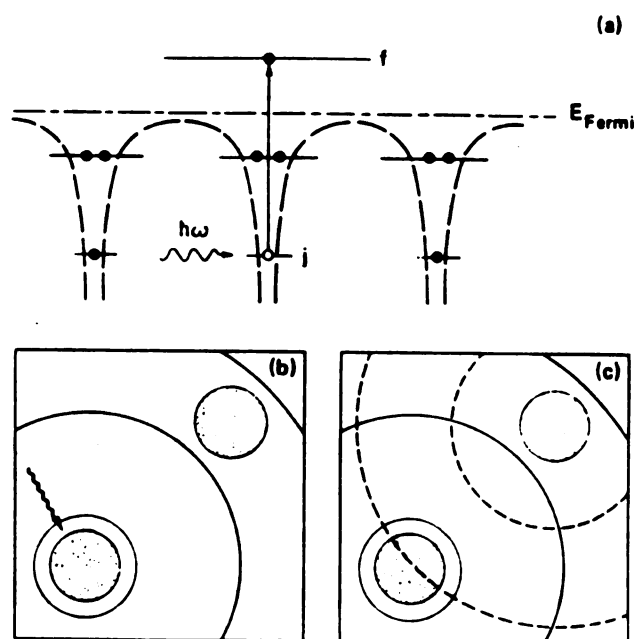
Figure 5.2: The origin of the EXAFS. The outgoing photoelectron wave(solid lines) and backscattered photoelectron wave(dashed lines) interfere at the center of the absorbing atom and thereby modulates the absorption cross-section. After T.M. Hayes and J.B. Boyce[2].

term has critical importance. The limited range for the photoelectrons in the energy region of interest(30-1000eV) imposed by this damping term permits a short range order description of EXAFS even in crystalline materials.

There are many parameters in eq.5.1 and this fact is often used in criticizing EXAFS studies. B.N. Teo[3] reviews the progress made in EXAFS studies and gives a more concise statement on the number of parameters: "Each EXAFS spectrum contains two sets of highly correlated variables; $[f(k, \pi), N, \sigma, \lambda]$ and $[\psi(k), E_0, r]$." Indeed by dividing eq.5.1 into the oscillatory part $\sin[2kr_j + \psi_j(k)]$ containing only distances r_j and phase shifts $\psi_j(k)$ and the amplitude function

$$A(k) = -\sum_j \frac{N_j}{kr_j^2} |f_j(k, \pi)| e^{-2\sigma_j^2 k^2} e^{-2r_j/\lambda_j(k)} \tag{5.5}$$

we can handle the two groups of parameters separately. The use of theoretical calculations for $f(k, \pi)$ and $\psi(k)$, the use of model compounds of known structure and the use of Fourier Transform (FT) techniques reduce the number of free parameters to a manageable number. The resultant structural information is for the local environment(generally about $6\text{\AA}$) around specific atoms.

5.2 Experimental techniques

Strictly speaking an EXAFS spectrum can be derived only from a measurement of the photoabsorption cross section over an appropriate range of X-ray photon energies. The more direct approaches to this involve measuring the normal incidence transmittance or grazing angle reflectance of the sample. In the transmission mode the optimum signal-to-noise ratio is obtained when the sample is about two absorption lengths thick.[2] Since this typically requires several microns of sample with subsequent tests at slightly different thicknesses to verify the absence of thickness effects, the transmission mode is not suitable for ultrathin multilayers with their attendant substrates.

The absorption cross section can also be inferred indirectly through measurement of some particular response of the sample to the absorption events. Such indirect schemes may involve detection of photoemitted electrons, of the fluorescent

X-rays or of Auger electrons emitted when the hole in the core of the excited atom is ultimately filled.

Fluorescence or total electron yield spectroscopy were used in this thesis. The core hole created by the photoabsorption process can decay by either a radiative or a nonradiative transition. In radiative decay, a higher lying electron fills the core hole with the emission of a photon of energy equal to the difference the two energy levels. The intensity of the fluorescence is proportional to the probability that the incident photon has created a core hole, that is, it is proportional to the absorption coefficient. Thus the fluorescence exhibits EXAFS.

Total electron yield detection monitors all the photoemitted electrons including Auger electrons and inelastically scattered secondary electrons as well as the electrons that are elastically emitted from the sample.

The standard experimental geometry is shown in fig.5.3 A tunable X- ray source is needed for EXAFS experiment and this is accomplished with a double single crystal monochromator which is controlled by a computer. A focused monochromatic X-ray beam is passed through a partially transparent ionization chamber to provide incident beam normalization and then allowed to strike the sample mounted inside the electron yield detector or fluorescence detector. EXAFS data in this thesis were taken on beam lines X9A, X11A and X23B in the National Synchrotron Light Source on the Brookhaven National Laboratories using experimental setups established by the PRT groups.

5.3   EXAFS analysis

In this section we deal with the analysis of EXAFS data. Given a set of data and the basic EXAFS equation eq.5.1, there are clearly a large number of approaches for extracting distances and information about the phase shifts and the amplitudes. In this thesis FT(Fourier Transform) and curve fitting with theoretically calculated scattering amplitudes and phase shifts were used in an existing EXAFS analysis software package.[4] It is clear that a knowledge of the phase $\psi(k) = 2\delta_1(k) + \phi(k)$

is essential for obtaining distances from EXAFS data. The theoretical values of backscattering amplitude $|f(k,\pi)|$, phase of the backscattering amplitude $\phi(k)$ and the central atom phase shift $2\delta_1(k)$ calculated by Teo and Lee[5] were used for curve fitting.

The EXAFS data shown in fig.5.1 for a pure Fe foil will be used to demonstrate the EXAFS data analysis procedures.

5.3.1 Background removal

The structure of bulk Fe is well known and serves here only as a good test of our analysis procedure. The modulation above the K edge near 7112 eV is due to the EXAFS $\chi(k)$ from several shells of neighboring atoms adding together. The first step in the analysis is to isolate $\chi(k)$ from the total absorption coefficient data. The pre-edge background was removed by a linear spline fitting and the smooth background above the edge was removed with polynomial splines using a least-square procedure.

Fig.5.4 shows the extracted pure EXAFS signal after removing the backgrounds and converting from $\hbar\omega$ to k. The curve has been multiplied by k^3 and this has the effect of weighting the EXAFS oscillations more uniformly. This step is important in preventing the larger amplitude oscillations from dominating the smaller ones in determining the interatomic distances, which depend upon only the frequency and not the amplitude of the $\sin[2kr_j + \psi_j(k)]$ function in eq.5.1.

5.3.2 Fourier transform filtering

The next step in the analysis is a FT. This isolates the contributions of the different shells of neighbors and allows the use of filtering techniques both to remove much of the noise and to study each shell separately.

Fig.5.5 shows the magnitude of the FT of the $k^3\chi(k)$ data in fig.5.4. The large peak at $\sim 2.2\text{Å}$ is the contribution from the first shell of 8 atoms at the distance 2.4823Å and the second shell of 6 atoms at the distance 2.8663Å.[6] The resolution into two peaks for the first two shells was not possible and the first peak in the FT magnitude contains the contributions of both shells. The four arrows in fig.5.5

A. Transmitted flux
   monitor

Sample (foil)

B. Fluorescence
   detector
   Z-1 filter/slits

sample

fluorescence
x-rays

synchrotron
source

double crystal
monochromator

Incident flux
monitor

A or B

polychromatic
x-rays

monochromatic
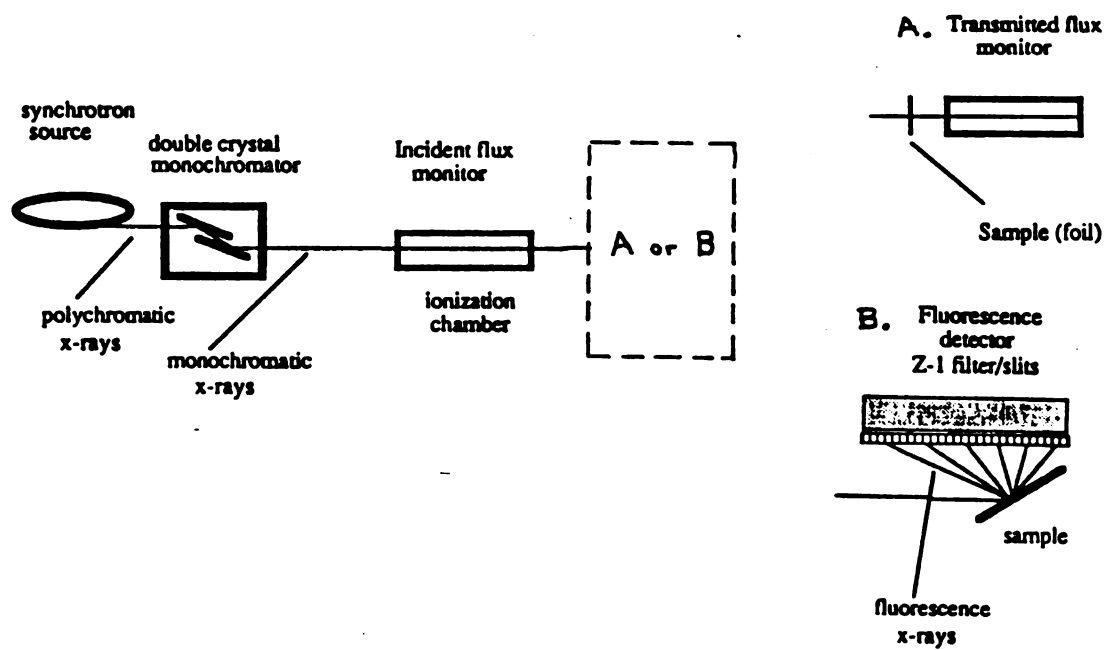x-rays

ionization
chamber

Figure 5.3: Standard experimental geometry for EXAFS experiment.

indicate the distances of the first four shells in BCC Fe. The FT peaks are located at apparently lower distances due to the effect of the phase shift $\psi_j(k)$.

The dashed line in fig.5.5 is a smooth filter window function for isolating the first 2 shells EXAFS. After filtering, the inverse FT is performed to give the solid curve in fig.5.6. Note that the absence of all higher frequency variations and noise.

5.3.3 Curve fitting

A curve fitting has to be used to separate two or more radial distribution function peaks which are not resolved by the FT technique.

Once the EXAFS data for particular shells has been extracted by the inverse FT as shown by the solid line in fig.5.6, the data analysis turns to fitting the observed EXAFS data with simulated data which is calculated assuming some hypothetical structure and the EXAFS expression given by eq. 5.1. The curve fitting procedure consists of a non-linear least square optimization process. The measure of goodness of fit used by XFPAK is called the minimization function F, which is defined as follows:

$$F = \sqrt{\sum_n [k^3(\chi_{obs}(k) - \chi_{cal}(k))]^2} \tag{5.6}$$

where $\chi_{obs}(k)$ is the observed EXAFS data and $\chi_{cal}(k)$ is the calculated data with a model. The sum is over the entire data range. Thus F^2 is the sum of square of errors between the observed and simulated data, weighted by k^3.

Since the first peak in the FT magnitude in fig.5.5 contains the contributions from the first 2 shells, we assumed 2 shells in our curve fitting. The known distances and the number of atoms in the first 2 nearest shells (8 atoms at $2.4823\overset{\circ}{A}$ and 6 atoms at $2.8663\overset{\circ}{A}$) were given as the initial parameters. These parameters and the threshold energy E_0 were allowed to vary during the optimization process. We note that E_0 is often shifted from its original value due to the change of chemical environment[1] or systematic errors in data aquisition.

The best fitting was obtained with 8.8 atoms at $2.47 \pm 0.06\overset{\circ}{A}$ and 4.0 atoms at $2.84 \pm 0.04\overset{\circ}{A}$ and the value of the minimization function was $F = 0.346$. The dotted
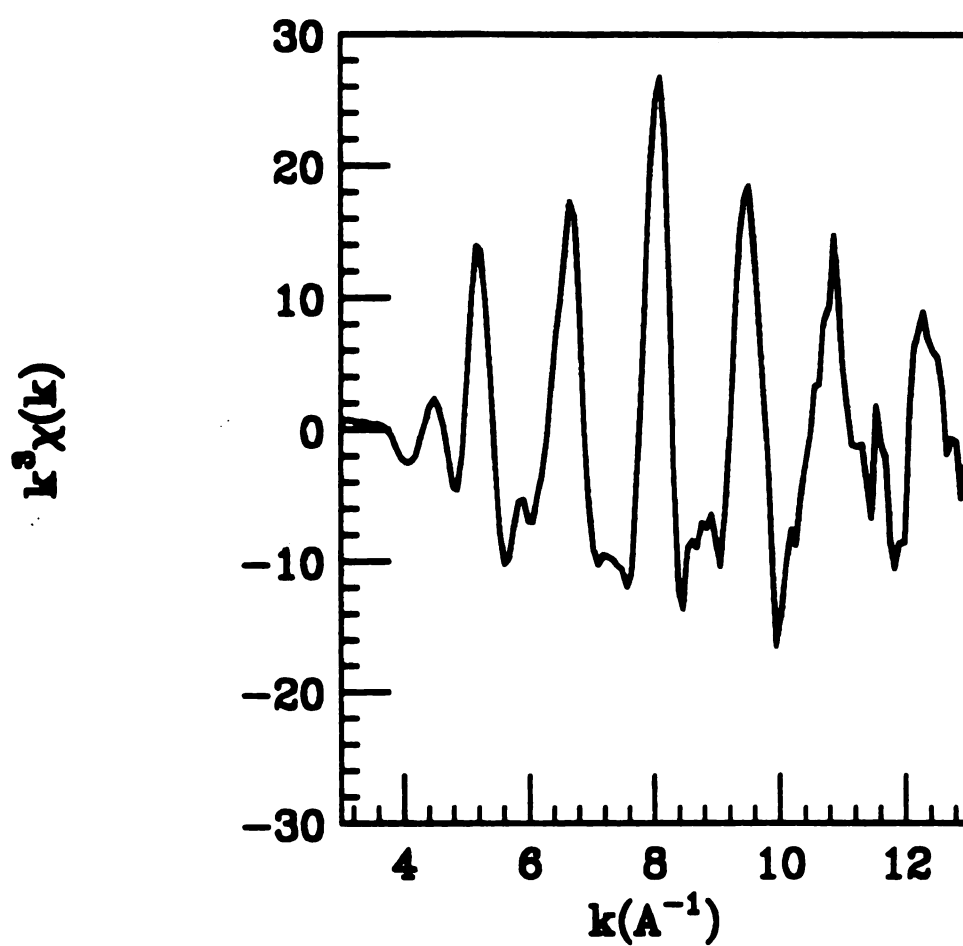
Figure 5.4: $k^3\chi(k)$ derived from fig. 5.1 by removing smooth backgrounds using a polynomial spline fit. The photon energy $\hbar\omega$ has been converted to the photoelectron momentum k.
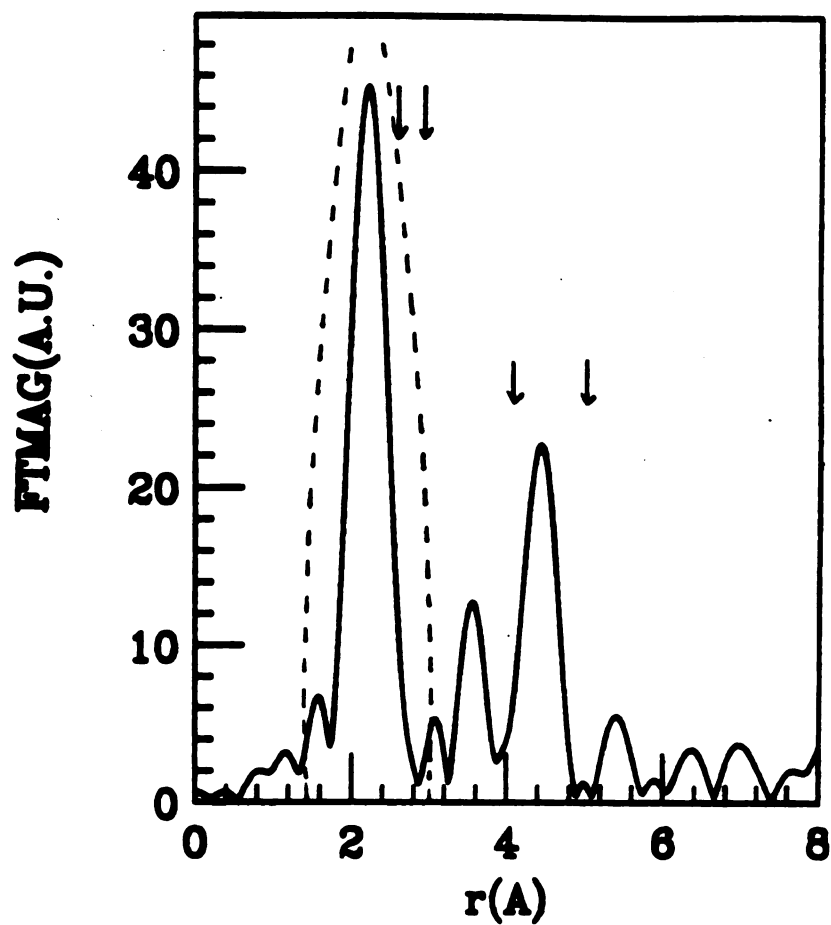
Figure 5.5: The magnitude of the Fourier transform of the curve in fig. 5.4. The dashed line denotes a window function used to isolate the EXAFS signal of the first peak. The 4 arrows indicate the actual positions of the first 4 nearest neighbors.
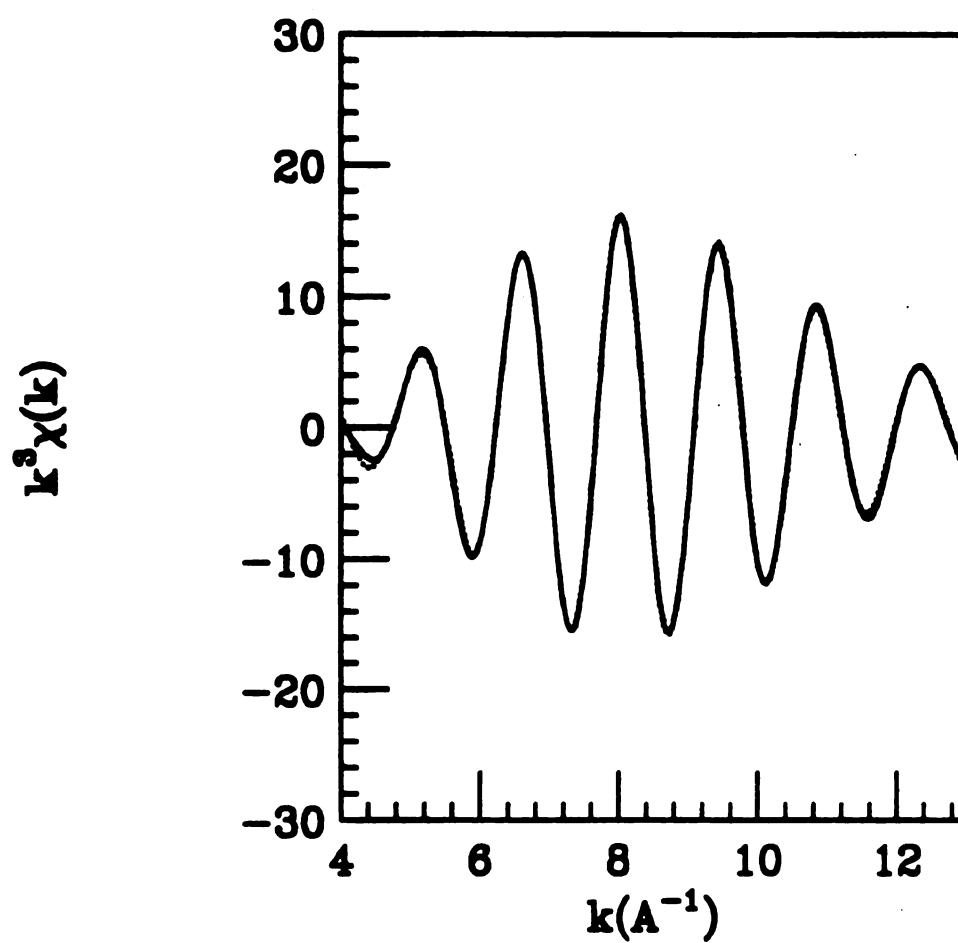
Figure 5.6: Inverse transform of Fourier transformed data in fig. 5.4 after multiplication by the window function shown in fig. 5.5. The dotted curve is the simulated EXAFS using only the first 2 Fe neighboring shells.

line in fig.5.6 shows the simulated curve with this 2 shell model; the experimental data and the simulated curve are nearly indistinguishable.

5.4 Structural changes observed by EXAFS in metallic multilayers

In chapter 4, we discussed the loss of magnetism in metallic multilayers, especially in the Fe/Si and Fe/Mo systems.(see fig.4.2 and fig. 4.5) In this section EXAFS data of these Fe multilayers will be described. To set a context for these EXAFS data we give a brief review of findings for the Fe/Si and Fe/Mo systems.

The Fe layers in the Fe/Si system lost their magnetism when the Fe layer thickness was less than about $10\mathring{A}$. In chapter 4 the pattern of saturation magnetization versus Fe layer thickness for Fe/Si multilayers was explained excellently with a model assuming magnetically dead Fe layers of $10\mathring{A}$ thickness in each Fe layer. The Fe(110) X-ray Bragg line became weaker and broader as the Fe layer thickness decreased and TED data also showed the systematic loss of the long range order in Fe layers as we discussed in chapter 3. The magnetically dead layers are believed to be amorphous.

The Fe/Mo samples with a constant 3ML Fe layer thickness and varying Mo layer thicknesses showed a drastic change in the saturation magnetization. While 3ML Fe/3ML Mo samples are essentially non-magnetic, the saturation magnetization reaches that of bulk value as the Mo thickness increases. It is strongly suspected that structural changes in the Fe layers are responsible for this magnetic behavior. In contrast to systematic changes in XRD data for Fe/Si samples, all 3ML Fe /t ML Mo samples have rather sharp X-ray reflection lines as shown in fig. 3.20 and fig.3.21. These sharp lines indicate well layered structure and no structural change in the Fe layers, even in 3ML Fe/3ML Mo sample, was observable by XRD.

In the remaining part of this chapter, the structural changes in the Fe layers in Fe/Si and 3ML Fe/t ML Mo samples determined from EXAFS analysis will be discussed.

5.4.1   EXAFS data of Fe/Si multilayers

EXAFS spectra of 2 Fe/Si multilayers were taken using the fluorescence detection method. The nominal sample parameters were $30\mathring{A}$ Fe/$50\mathring{A}$ Si and $18\mathring{A}$ Fe/$30\mathring{A}$ Si, respectively. Fig.5.7 shows the spectra. One can notice the similarity between the EXAFS spectrum of the $30\mathring{A}$ Fe/Si multilayer and the spectrum of a pure Fe foil in fig.5.1 while the spectrum of the $18\mathring{A}$ Fe multilayer is qualitatively different.

The difference in the spectra is more clearly seen in the extracted pure EXAFS spectra after removing the background and converting to k-space(Fig.5.8). The EXAFS spectrum of the $30\mathring{A}$ Fe layer sample is quite similar to that of the Fe foil in fig.5.5, showing multifrequency character , while the EXAFS spectrum of the $18\mathring{A}$ Fe sample resembles a single frequency with weaker amplitude and shifted peak positions. A single frequency in an EXAFS signal is a typical feature of an amorphous structure implying the dominance of a single near-neighbor distance in the EXAFS.[2]

The Fourier transform of an EXAFS spectra in k-space produces an approximate radial distribution function in real space which is shown in fig.5.9. For the $30\mathring{A}$ Fe layer sample, the FT magnitude of the EXAFS signal is essentially identical to that of pure Fe with up to the third peak. But the FT magnitude of the $18\mathring{A}$ Fe sample shows only the first peak; no evidence of higher peaks is seen confirming that the structure of the Fe layers in this sample is predominantly amorphous. The peak in FT magnitude also suggests that the nearest neighbor distance in the $18\mathring{A}$ Fe layers is substantially reduced. However the positions of each peak are not the actual distances of each shell since the phase shifts of absorbing atoms and backscattering atoms cause non- physical translations in the FT.

To calculate the nearest neighbor distances from the observed EXAFS data, inverse FT and curve fitting were used. A smooth Gaussian window function with the half width of $0.1\mathring{A}$ was used to isolate the first peak in each FT magnitude. Fig.5.11(a) and (b) shows the observed EXAFS data of the first peaks (denoted by solid lines) and the best curve fittings of them (denoted by dotted line). For the $30\mathring{A}$ Fe sample, the best fitting was obtained using a 2 shell model and for the $18\mathring{A}$
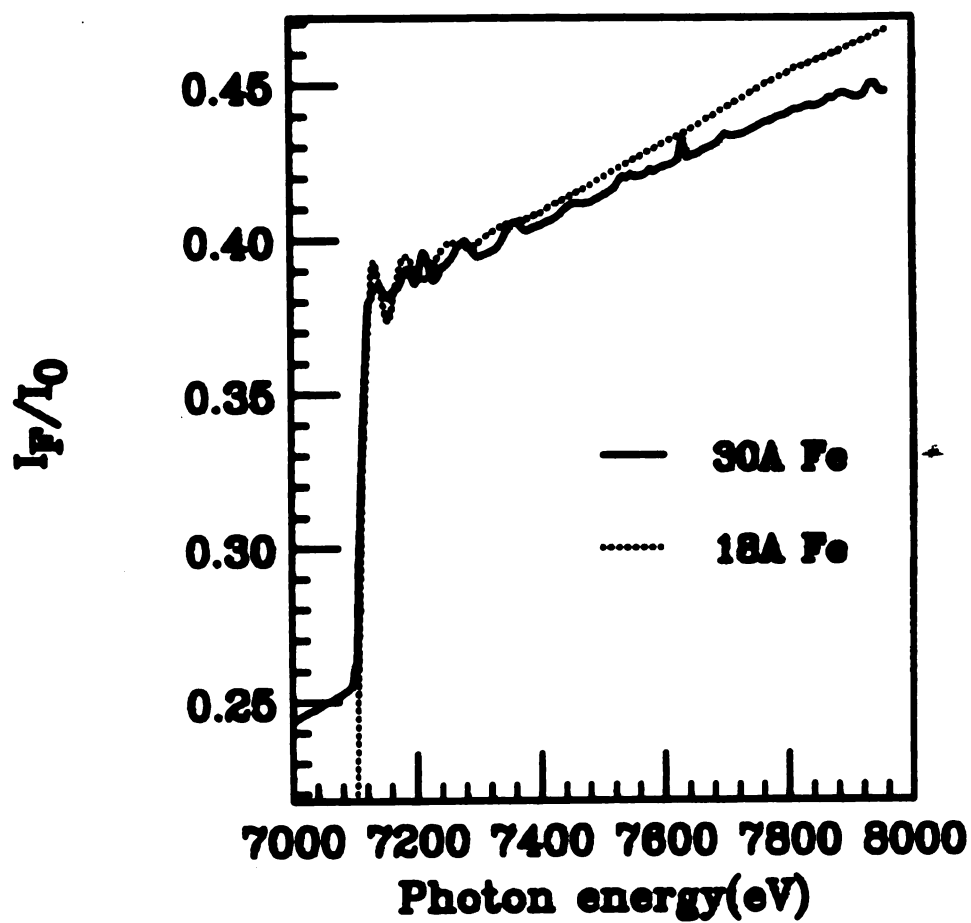
Figure 5.7: X-ray absorption spectra of two Fe/Si multilayers measured by the fluorescence detection method.
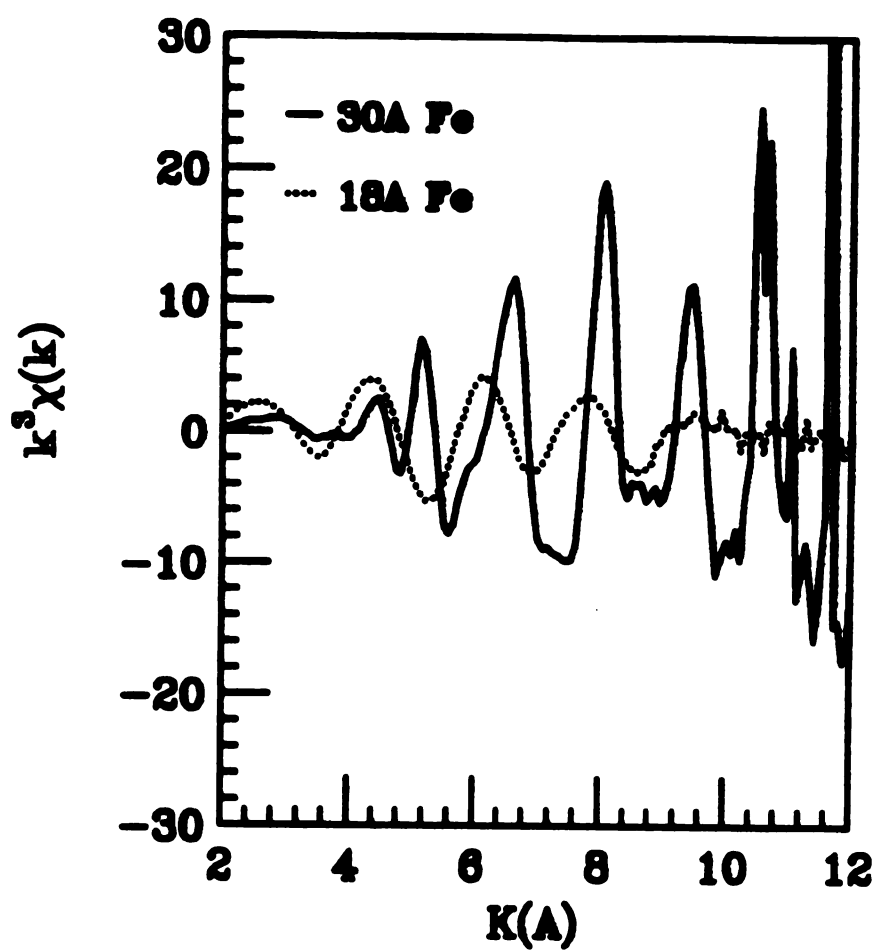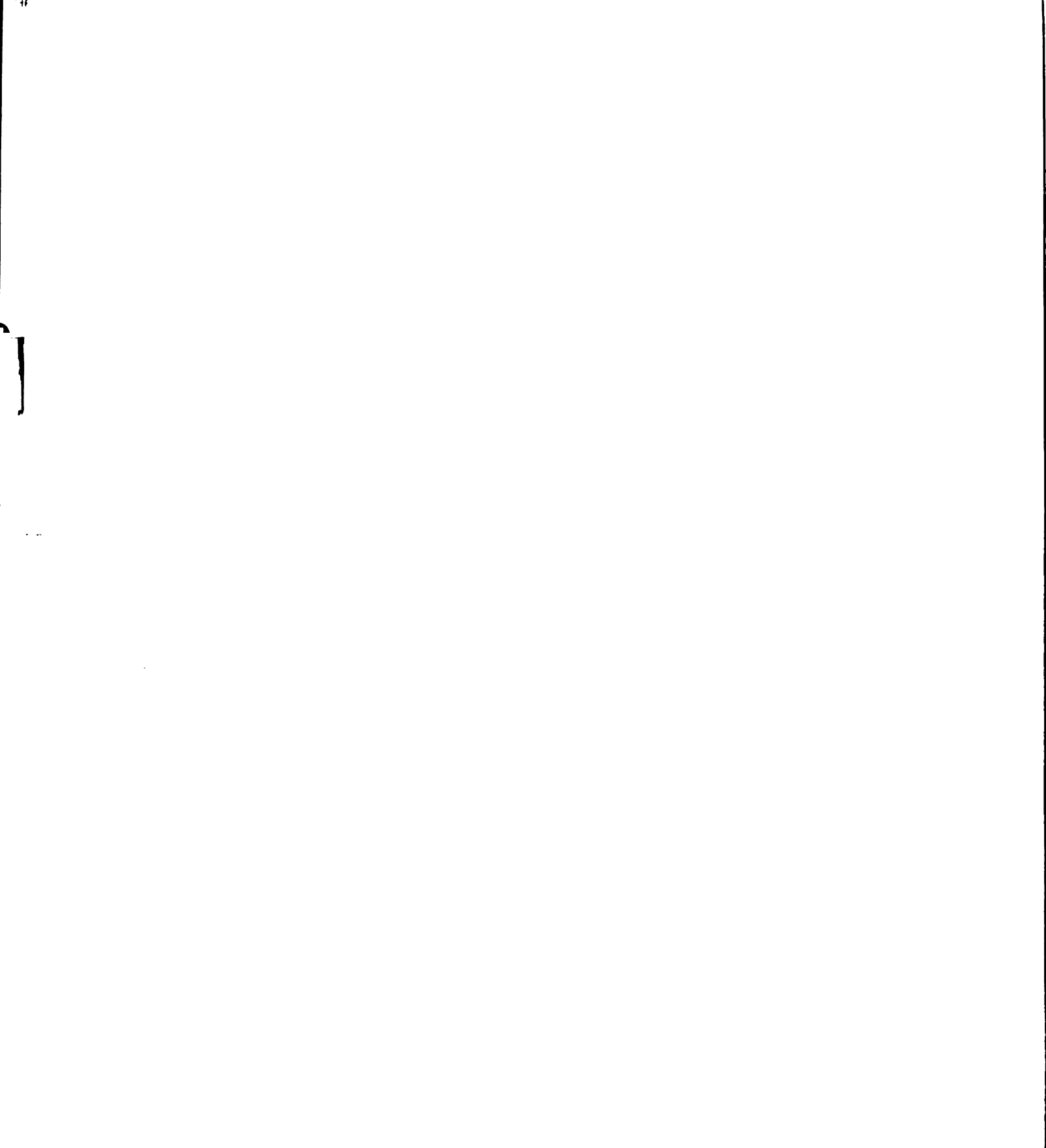
Figure 5.8: Extracted EXAFS spectra $k^3\chi(k)$ for two Fe/Si multilayers after removing backgrounds.

Fe sample a single shell model gave the best curve fitting. These results suggest crystalline Fe is dominant in the 30Å layers while amorphous Fe is predominant in the 18Å Fe layers. The structural parameters for the best fit curves are as follows:

(i) 30Å Fe/50Å Si

2 Fe atomic shells: 4.7 atoms at 2.36±0.05Å and 4.9 atoms at 2.80±0.02Å

(ii) 18Å Fe/30Å Si

1 Fe atomic shell: 10 atoms at 2.39±0.14Å

5.4.2 EXAFS data of 3ML Fe/t ML Mo systems

The Fe layers in 3ML Fe/t ML Mo multilayer samples(from now on we will denote such a multilayer just as 3/t) show a drastic change in magnetism, being non-magnetic with $t = 3$ and bulk Fe like ferromagnet with $t \geq 4$. All 3/t samples have quite sharp average Bragg line(perpendicular structural coherence $\xi_\perp \sim 200$Å). There are satellites in the high angle XRD data and at least 2 harmonics in the low angle XRD data indicating highly ordered samples composed of crystalline individual layers with good chemical modulation. Any evidence of structural change in the non-magnetic 3/3 sample was not observable with XRD measurements.

Extracted EXAFS spectra $k^3\chi(k)$ of 3/t samples(t =3,4,8 and 12) are depicted in fig.5.11. One immediately notices the uniqueness of the EXAFS data of 3/3 compared to the other spectra. The period of oscillation for 3/3 is clearly longer than the periods of others and a longer period in k-space indicates a short distance to the near neighbors. The envelope function expressed by eq.5.5 is a function of the number of neighbors, the scattering amplitudes of neighbors, thermal vibrations and the mean free path for photoelectrons. The envelope functions of the samples with t =4, 8 and 12 appear to be very similar. These facts suggest that a structural change occurred in the non-magnetic Fe layers of the 3/3 sample.

The FT magnitudes of the EXAFS spectra in fig.5.11 are shown in fig. 5.12. As expected the position of first peak in the FT magnitude for 3/3 is shifted to a shorter distance compared to other first peaks. The higher order peaks in the FT
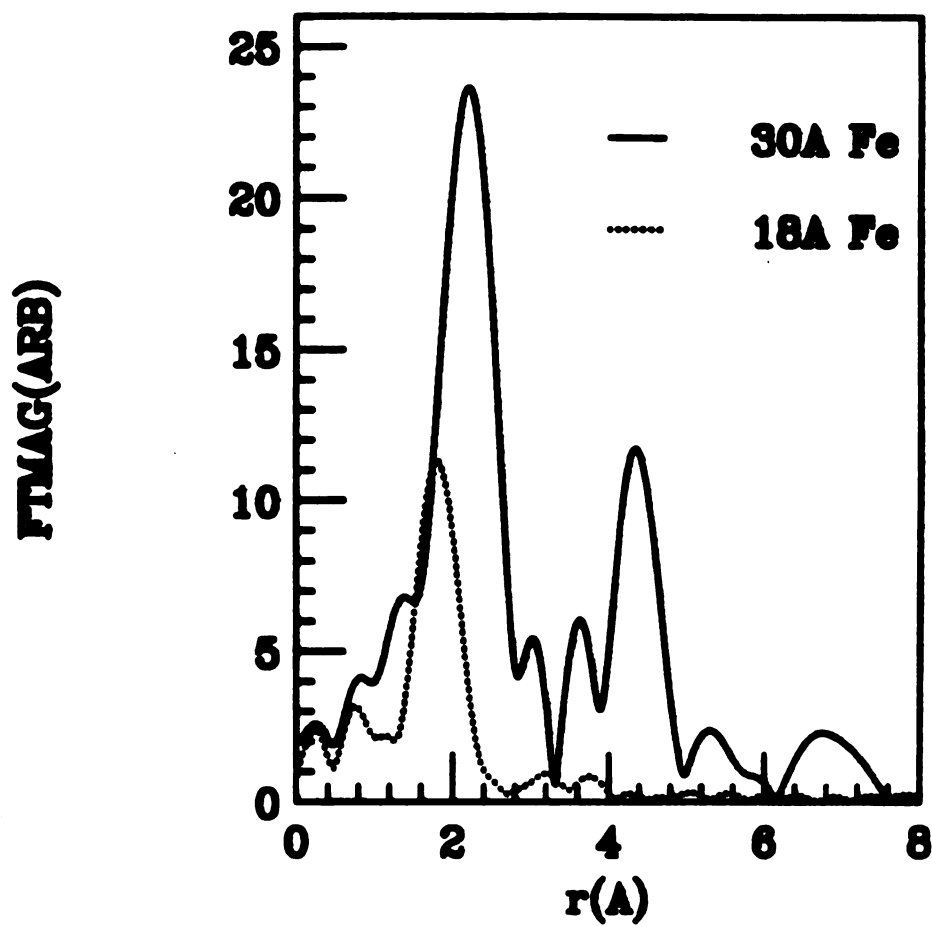
Figure 5.9: Fourier transform magnitudes of $k^3\chi(k)$ in fig.5.9. The FT magnitude of $30\mathring{A}$ Fe layers clearly shows higher order peaks indicating BCC crystalline structure.
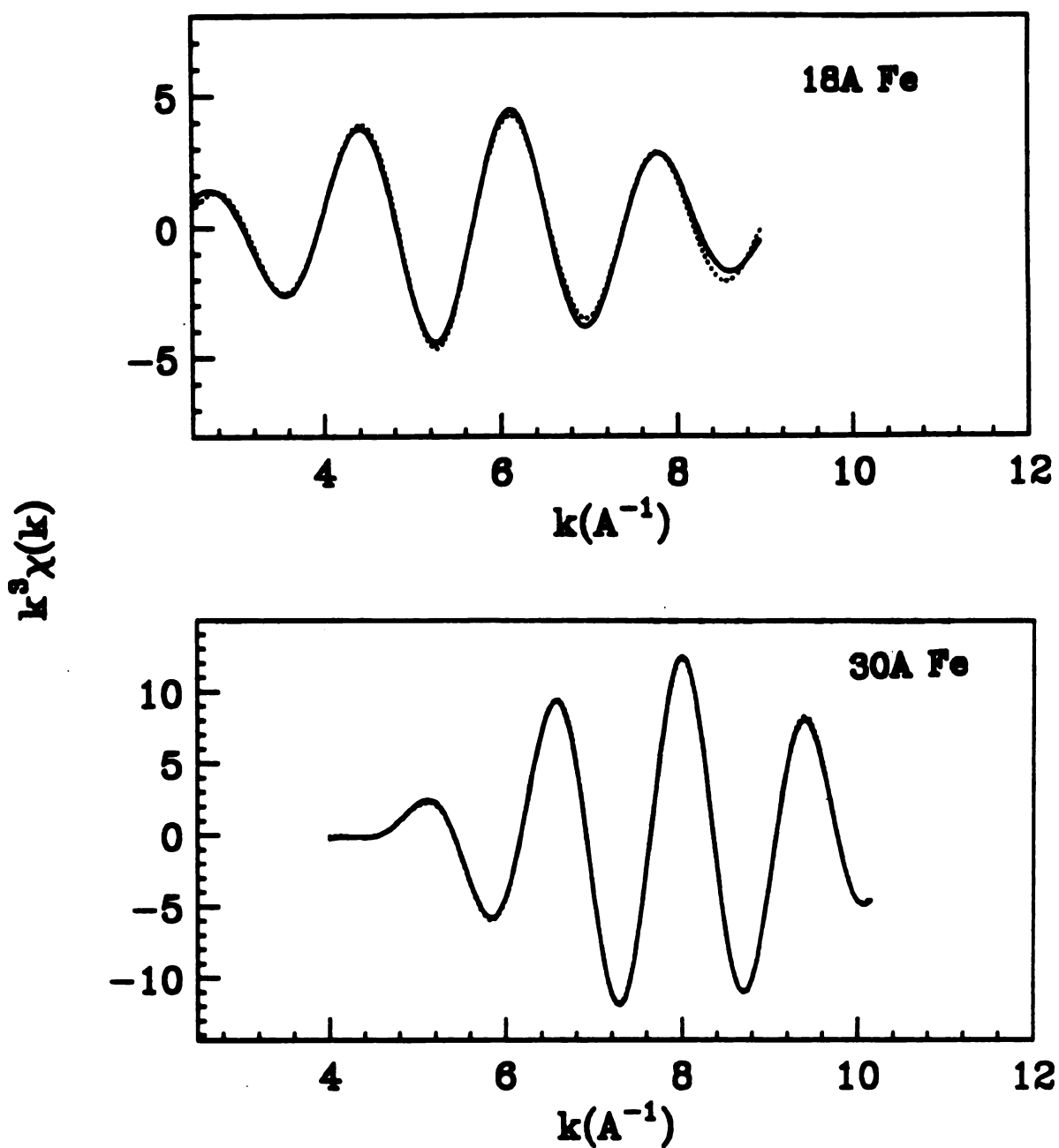
Figure 5.10: Observed(solid lines) and calculated(dotted lines) EXAFS data. The fitting parameters for the simulated curves are given in the text.
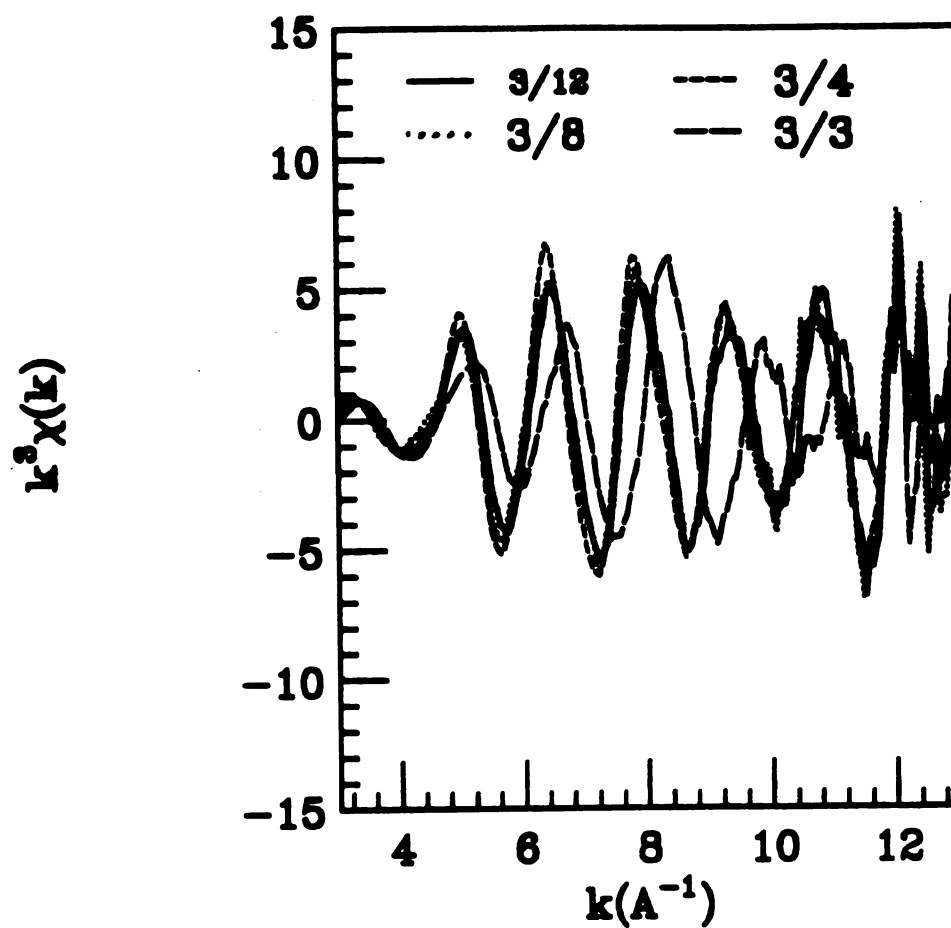
Figure 5.11: Pure EXAFS spectra of 3/t Fe/Mo samples. Note the difference in the period and envelope function of the EXAFS of the 3/3 system compared to the other spectra.
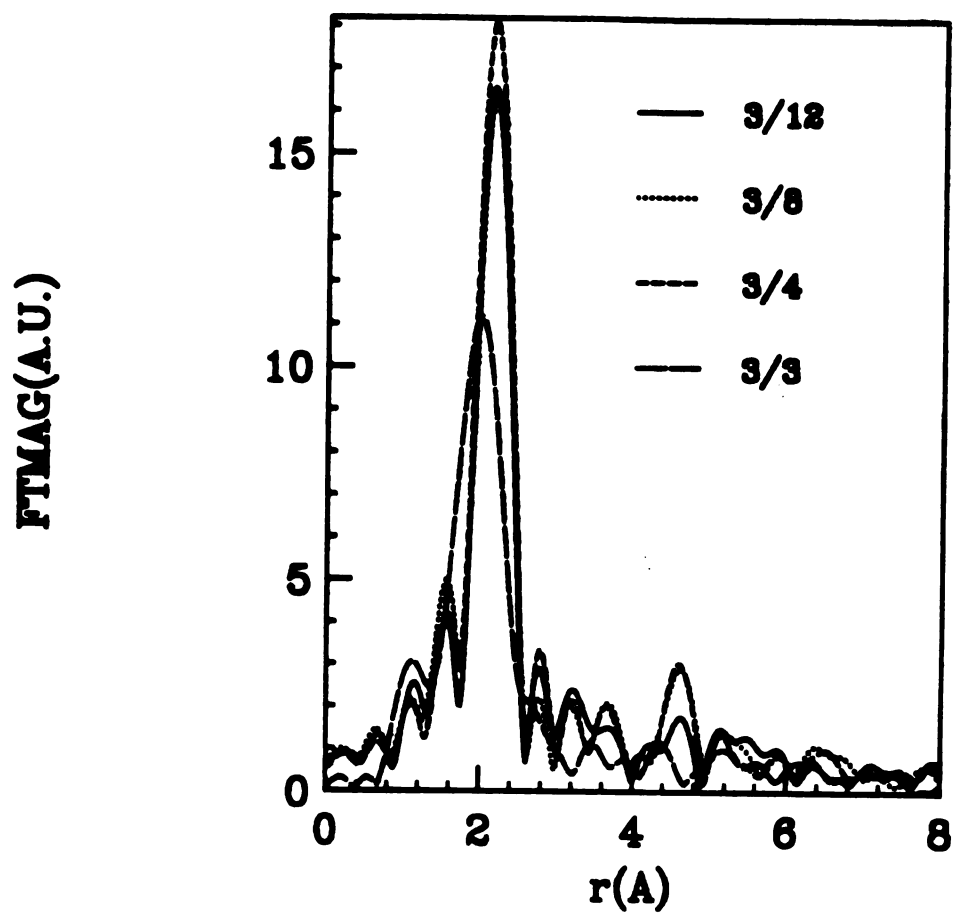
Figure 5.12: FT magnitudes of the EXAFS data of 3/t Fe/Mo samples in fig.5.11. The first peak in the FT magnitude of the 3/3 samples is shifted toward shorter distances relative to the others.

magnitudes are rather weak; each sample with $t \geq 4$ has a faint hint of a higher peak at about $4.4\mathring{A}$. Any trace of this higher peak in the 3/3 sample is lost in the noisy background. In last section, it was noted that the absence of the high order peaks in FT magnitudes is generally attributed to the highly disordered structure. At the first sight the weakness of the higher order peaks in 3/t Fe/Mo multilayers is puzzling because the XRD data indicate good crystalline layer in these samples.

But our samples are layered with the Fe layer thickness being fixed at only 3ML and the higher order peaks (i.e. more distant atomic shells) would have both Fe and Mo atoms. In table 5.1, the number of Fe atoms and Mo atoms in the first 4 atomic shells of an Fe atom are counted for the case of 3 ML Fe layers having Mo layers on each side with the (110) texture out of plane and atomically sharp interfaces. In reality the number of Mo near neighbors would be even larger than these values when we allow for the rough interfaces and possible interdiffusion. The fact that the calculated back scattering amplitudes $|f(k,\pi)|$ and phase shifts $\phi(k)$ of Fe atoms and Mo atoms are much different from each other [5] and that the structural information in EXAFS data has been spherically averaged could appear as increased disorder around a central Fe atom. Increased disorder would damp the higher order peaks in the FT magnitudes of our 3/t Fe/Mo multilayers even in the case of crystalline individual layers. No attempt to calculate the EXAFS spectrum with many number of shells with varying numbers of Fe atoms and Mo atoms was done.

As noted earlier the first peak in the FT magnitude of BCC Fe contains the contributions from the first 2 atomic shells. Furthermore noting in table 5.1 that the average number of Mo atoms in the first 2 shells of an Fe atom in an ideal 3 ML Fe layer is relatively small, curve fittings for the first peaks in the FT magnitudes were done. Each fitting assumed only Fe atoms and trends rather than values are the goal. Appropriate Gaussian filtering window functions were used each FT magnitude.

Fig.5.13 depicts the observed and simulated EXAFS spectra of each 3 /t sample. The curve fitting of 3/3 is very poor; the value of the minimization function $F = 0.923$ and a negative number of atoms is required. The simulated EXAFS data
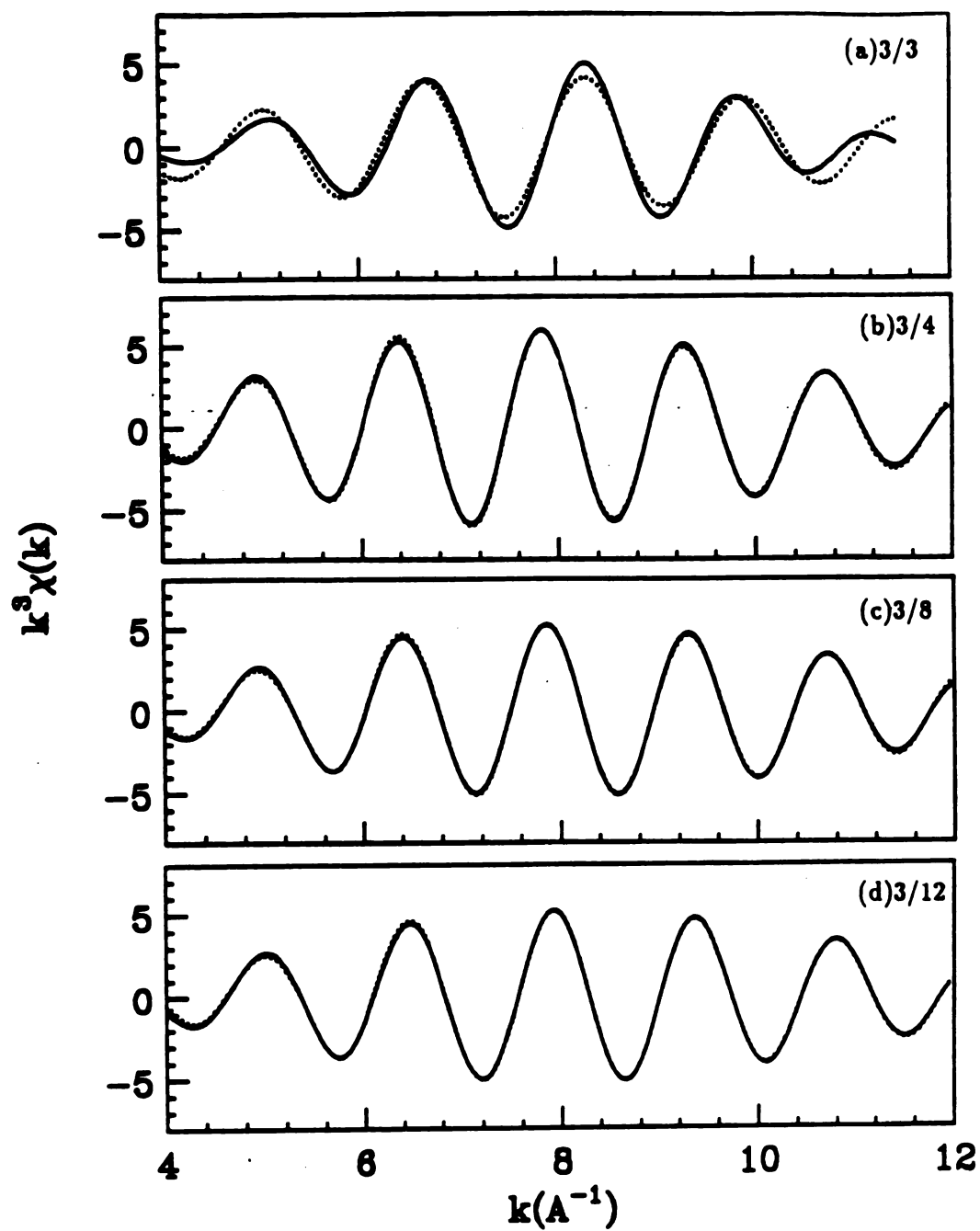
Figure 5.13: Observed(solid line) and calculated EXAFS spectra for 3/t Fe/Mo systems. (a)3/3 (b)3/4 (c)3/8 (d)3/12. The 3/3 system is not fitted very well by the 2 Fe shell model.

of samples with $t = 4,8$ and 12 shows much better curve fittings with smaller values of F. The variables in these curve fittings were the near neighbor distance r and the half width of its fluctuation σ, the number of neighbors n and the threshold energy ΔE_0. The structural parameters obtained from the best curve fittings in fig. 5.13 are given in table5.2. In general the number of Fe atoms in the first 2 shells obtained by simulation is rather far from the values of the ideal model system for 3/t samples. This is in contrast to the 12/12 sample for which the obtained structural parameters are quite close to the bulk crystalline values. The crudity of the 2 shell model involving Fe atoms only forces poor results. Never-the-less, the relative constant value of n in the first shell and the lack of unrealistic n values in the second shell for 3/4, 3/8 and 3/12 are encouraging. Such features may indicate better BCC like crystalline Fe layers in these samples than in the 3/3 samples.

j	Total No. of N.N	Atom at center layer Fe	Mo	Atom at interface Fe	Mo	Average Fe	Mo
1	8	8	0	6	2	6.67	1.33
2	6	6	0	4	2	4.67	1.33
3	12	10	2	7	5	8	4
4	8	4	4	6	2	5.33	2.67

Table 5.1: The number of Fe atoms and Mo atoms in the first 4 nearest neighbor shells of the Fe atoms in an ideal 3 ML Fe(110) layer with thick Mo layers on both sides.

	First shell $r(\overset{\circ}{A})$	n	σ	ΔE_0	Second shell $r(\overset{\circ}{A})$	n	σ	ΔE_0	F
3/3	2.61	7.3	0.1	29.3	2.94	-14.3	0.17	45	0.923
3/4	2.50	5.5	0.08	-5.2	2.90	0.32	0	-13.2	0.152
3/8	2.50	5.5	0.08	-6.5	2.78	2.0	0.08	-5.2	0.111
3/12	2.48	5.82	0.07	-6.8	2.90	0.7	0.06	-23.6	0.118
12/12	2.43	7.5	0.06	-4.13	2.79	5.3	0.04	6.0	0.129

Table 5.2: The optimum fitting parameters of the EXAFS data for the Fe/Mo systems considering only the first 2 Fe atomic shells.

Bibliography

[1] P.A. Lee, P.H. Citrin, P. Eisenberger, and B.M. Kincaid Rev. of Mod. Phys., 53, 769, (1981)

[2] T.M. Hayes and J.B. Boyce Solid State Physics 37, 173, (1982)

[3] Boon K. Teo EXAFS: Basic Principles and Data Analysis (Springer-Verlag, 1986)

[4] EXAFS Analysis Software Package School of Chemical Science, University of Illinois Urbana

[5] B.K. Teo and P.A. Lee Jour. of Am. Chem. Soc. 101, 2815 (1979)

[6] CRC Hand book of Chemistry and Physics, 66th edition 1985

Chapter 6

Summary and recommendations

6.1   Structure and magnetism

Metallic multilayers, Fe/Si, Fe/Mo, Fe/V and Fe/Cr, were prepared using a sputtering system. The individual layer thicknesses were between 3 ML and 40 ML.

In the XRD(X-ray diffraction) data of the Fe/Si multilayers, at least 3 harmonics were observed at small angles indicating a compositionally modulated structure. No high angle satellite was seen; only a broad Fe(110) bragg line was observed. Si layers were amorphous and the ultrathin Fe layers were structurally isolated in our Fe /Si multilayers. The saturation magnetization decreased with decreasing Fe layer thickness and vanished near 5 ML. A simple magnetic model assuming magnetically dead Fe layer of 5ML explained the reduction of magnetism in Fe/Si as the Fe layer thickness decreased. Both XRD data and TED(Transmission Electron Diffraction) data were consistent with a crystalline to amorphous transition as the Fe layer thickness decreased. EXAFS data confirmed this transition. We conclude that about $10\text{\AA}$ of amorphous Fe were grown on the amorphous Si layers before crystalline Fe layers were resumed and the amorphous Fe layers were non-magnetic.

For Fe/X(X=Mo, V and Cr) systems, successful crystalline layered structures were confirmed by XRD data and calculation. In most of our samples, values of the modulation period determined from XRD data agreed to the nominal values within 5% or less. All the transition metal layers had BCC(110) texture in the film normal.

The typical value of the perpendicular structural coherence length(PSCL) from the FWHM of the average lines was $\sim 200\text{Å}$ without device broadening correction.

Fe/V was crystalline at all layer thickness but strains in the layers were observed when the layers were thinner than 16 ML. Both XRD data and TED data are consistent with the onset of a SLS(strained layered superlattice) in Fe/V. Comparison between XRD data and model calculations suggested that strains reside in Fe/V up to individual layer thickness 16 ML and that the strain is uniaxial. TED data provided the direct evidence of a SLS. Fe/V samples with layer thicknesses greater than 16 ML have a double BCC lattice in the sample plane while samples with thinner layers have a single BCC lattice.

XRD data and TED data for Fe/Mo systems also exhibited a double BCC to single BCC transition. However this transition differed significantly from that of Fe /V. First, the transition occurred abruptly without the gradual modification of individual layer structures that occurred in Fe/V. Second, the transition occurred at a smaller layer thickness, between 6 ML and 10 ML rather than 16 ML.

A reduction of magnetism started at layer thicknesses around these structural transitions in both the Fe/V and Fe/Mo systems. Fe/Mo lost its magnetism abruptly at thicknesses below 6 ML and was non-magnetic at 3 ML. The reduction of magnetism in Fe/V was gradual and 3 ML Fe layers still retained about 50% of the magnetization of bulk Fe. Fe layers in Fe/Cr had bulk Fe magnetizations at all layer thicknesses.

3 ML Fe/X systems showed an interesting interplay between structure and magnetism. The 3 ML Fe layers in 3ML Fe/Mo samples had a transition from non-magnetic to ferromagnetic(like bulk Fe) as the Mo layer thickness increased from 3 ML to 5 ML. While XRD data indicated crystalline structure in all Fe/Mo systems, at least in the film normal, preliminary EXAFS data analysis suggested better BCC like Fe layers in the samples with more than 4 ML Mo layers. The 3ML Fe/V samples had considerably reduced magnetization(below 70% of bulk value) at all V layer thicknesses but no drastic change in magnetism was seen. Fe and V are mutually soluble and the intermixing at interfaces could cause the reduction of magnetism

with relatively small structural change. The 3ML Fe/Cr sample retained the bulk magnetism at all layer thicknesses , neither structural change nor intermixing is indicated in this system.

6.2 Magnetic interlayer interaction in Fe/Cr

In parallel field magnetic measurements, saturation fields(H_S) of 4KOe are typical for all Fe/Mo and Fe/V samples independent of the layer thicknesses. In Fe/Cr, however, anomalously large saturation fields up to 46KOe have been observed when both the Fe layers and the Cr layers are thinner than 10ML. These saturation fields decrease rapidly and monotonically to $\sim$4KOe as the Cr interlayer thickness is increased to about 20ML. These anomalously large H_S's are believed to be from the antiferromagnetic coupling between the magnetic Fe layers across the Cr interlayers. H_S is also strongly dependent on the Fe layer thickness. In the samples with an Fe layer thickness of 25ML, H_S is $\sim$4KOe, the typical value for Fe/Mo and Fe/V, and no dependence on the Cr thickness is observed. This behavior suggests the disappearance of antiferromagnetic coupling for these thicker Fe layers.

Perpendicular field magnetic measurements provide a measure of magnetic anisotropies. The perpendicular saturation fields(H_A) of Fe/Mo and Fe/V satisfy $H_A = 4\pi M_S$ within the experimental error indicating no anisotropy other than the shape anisotropy. Again, however, H_A's for Fe/Cr showed large deviations from this relation. The value of the deviation, $\Delta H = H_A - 4\pi M_S$, ranged from -9KOe to 24KOe depending on the Fe layer thickness and the Cr layer thickness. The positive values of ΔH are closely related to the values of H_S giving essentially a linear function. It is believed that the large anisotropy is due to the magnetic interlayer coupling . The idea that the positive ΔH's are from antiferromagnetic coupling and the negative ΔH's are from ferromagnetic coupling is suggested.

6.3 Recommendations

(1) While XRD data indicate a crystalline structure for 3ML Fe/3ML Mo samples, at least in the film normal, EXAFS data suggest some kind of structural change in the non-magnetic 3ML Fe layers. Since TED data are not available in this thesis, TED measurements on this sample should be done to determine the in-plane structure.

(2) From the results of magnetic measurements it is believed that the Fe/Cr system has strong magnetic interlayer interactions while no, or very weak, magnetic interactions are present in the Fe/Mo or Fe/V systems. The conduction electrons in Cr layers are believed to be responsible for this interlayer coupling between Fe layers. The quality of the interfaces is generally believed to be important for this coupling. The nearest of Fe and Cr in the periodic table and the small lattice mismatch between them make structural studies by XRD or TED very difficult. A systematic perpendicular transport study of Fe/X(X=Mo, V, and Cr) is suggested as means of studying Fe/Cr interfaces relative to Fe/Mo and Fe/V interfaces.